ALMA MATER STUDIORUM
UNIVERSITÀ DI BOLOGNA

DOTTORATO DI RICERCA IN

INGEGNERIA ELETTRONICA, TELECOMUNICAZIONI E TECNOLOGIE DELL'INFORMAZIONE

Ciclo 36

Settore Concorsuale: 09/F2 - TELECOMUNICAZIONI

Settore Scientifico Disciplinare: ING-INF/03 - TELECOMUNICAZIONI

SIGNAL PROCESSING ALGORITHMS FOR JOINT SENSING AND COMMUNICATION

Presentata da: ***Lorenzo Pucci***

Coordinatore Dottorato

Aldo Romani

Supervisore

Enrico Paolini

Co-supervisore

Andrea Giorgetti

Esame finale anno 2024

Alma Mater Studiorum - Università di Bologna

DOTTORATO DI RICERCA IN
Ingegneria Elettronica, Telecomunicazioni e Tecnologie
dell'Informazione

Ciclo 36

Settore Concorsuale: 09/F2 - Telecomunicazioni

Settore Scientifico Disciplinare: ING-INF/03 - Telecomunicazioni

SIGNAL PROCESSING ALGORITHMS FOR JOINT SENSING AND COMMUNICATION

Presentata da:
LORENZO PUCCI

Supervisore:
Prof. Ing.
ENRICO PAOLINI

Coordinatore Dottorato:
Prof. Ing.
ALDO ROMANI

Co-supervisore:
Prof. Ing.
ANDREA GIORGETTI

Esame finale anno 2024

Keywords

Signal Processing

Joint Sensing and Communication

Orthogonal Frequency-Division Multiplexing

Orthogonal Time Frequency Space

5G & Beyond Systems

Multiple-Input Multiple-Output

Abstract

Joint sensing and communication (JSC) systems, i.e., systems that combine radar and communication functionalities within the same architecture by sharing hardware and physical layer resources, are gaining increasing interest for future mobile systems. By enabling precise user localization and non-collaborative objects detection, they can usher in a new era of mobile networks with ubiquitous and pervasive sensing capabilities. In this dissertation, several signal-processing techniques for JSC systems are investigated and a comprehensive analysis of the sensing performance of these systems is presented by focusing on two main contributions.

First, an analysis of orthogonal frequency division multiplexing (OFDM)-based JSC systems is performed by investigating the dominant factors that affect performance in the context of different radar settings (i.e., monostatic, bistatic, and multistatic) when considering line-of-sight propagation conditions. Several physical layer signal processing techniques are examined for estimating target positions and velocities, with particular emphasis on multiple-input multiple-output (MIMO) JSC systems. After analyzing the sensing performance in the presence of single and multiple point-like targets when considering a monostatic fully digital MIMO OFDM-based JSC system with multibeam capabilities, the analysis progresses to a bistatic configuration where the transmitter (Tx) and receiver (Rx) are not co-located, thus avoiding self-interference. Lastly, the analysis is extended to a MIMO multistatic configuration with a single Tx and two Rxs with hybrid digital-analog (HDA) architectures to exploit spatial diversity for improved target detection. This analysis considers extended targets (ET) and explores both near-field and far-field propagation conditions at millimeter wave (mmWave). The need for an ET model is recognized because real objects such as cars are more likely to appear as a collection of scattered points rather than a single reflection. Numerical results show the benefits of considering a multistatic setting to improve detection performance, and also of considering near-field propagation conditions when using large antenna arrays (e.g., at mmWave frequencies) to improve estimation performance when the target is close to Tx or Rx.

In the second part of this thesis, a JSC system using orthogonal time frequency space (OTFS) modulation is investigated. OTFS is a novel multicarrier modulation scheme that has shown promise for future mobile systems, particularly in JSC applications. However, it is associated with high computational complexity. For this reason, a novel low-complexity estimation and detection approach based on Dirichlet kernel analysis is presented by considering a monostatic JSC system. Through numerical simulations, it is proved that the proposed approximation technique effectively preserves the sensing performance while concurrently reducing the computational effort enormously.

The main goal of this dissertation is to contribute to a deeper understanding of OFDM- and OTFS-based JSC systems, along with their performance in various radar environments, and to provide innovative solutions to address key challenges.

Contents

Acronyms

AWGN additive white Gaussian noise

BER bit error rate

BF beamformer

BND binomial distribution

BS base station

CP cyclic prefix

CRLB Cramér-Rao lower bound

DFT discrete Fourier transform

DoA direction of arrival

DoD direction of departure

EIRP effective isotropic radiated power

ELP equivalent low-pass

ET extended target

ESPRIT estimation of signal parameters via rotational invariance techniques

FAR false-alarm rate

FFT fast Fourier transform

FMCW frequency modulated continuous wave

HDA hybrid digital-analog

ICI inter-carrier interference

IFFT inverse fast Fourier transform

i.i.d. independent, identically distributed

ISFFT inverse symplectic finite Fourier transform

ISI inter-symbol interference

JSC joint sensing and communication

LLR log-likelihood ratio

LoS line-of-sight

MC Monte Carlo

MCL maximum coupling loss

MDL minimum description length

MIL maximum isotropic loss

MIMO multiple-input multiple-output

ML maximum likelihood

mmWave millimeter wave

MPL maximum path loss

MUSIC multiple signal classification

NR new radio

OFDM orthogonal frequency-division multiplexing

OS-CFAR ordered statistic constant false alarm rate

OSPA optimal sub-pattern assignment

OTFS orthogonal time frequency space

PSD power spectral density

QPSK quadrature phase shift keying

RCS radar cross-section

RF radio frequency

RMSE root mean square error

Rx receiver

RoI region of interest

RRH remote radio head

r.v. random variable

SCM sample covariance matrix

SE spectral efficiency

SFFT symplectic finite Fourier transform

SI self interference

SISO single-input single-output

SNR signal-to-noise ratio

SSIR signal-to-self interference ratio

TDD time-division duplexing

Tx transmitter

UE user equipment

ULA uniform linear array

Chapter 1

Introduction

A key aspect of mobile radio networks, which received a significant boost in recent years, is the possibility to perform and exploit accurate user localization thanks to specific signaling capabilities offered by the standards. Such types of localization leverage user collaboration, who actively participate in the localization process. However, the need to equip mobile networks with sensing capabilities has recently emerged. Such ability consists in the detection and localization of non-collaborative objects, a feature typical of radar systems [1–5]. Joint sensing and communication (JSC) is a novel paradigm to fulfill the requirement of systems capable of performing both sensing and communication operations through the sharing of the physical layer and the hardware.

Despite the unquestionable benefits of JSC, the design of such a system is non-trivial because the two functionalities are at odds with one another and compete for spectral resources. On this issue, in the literature, we can find three main approaches [6, 7]:

1. the usage of communication signals for target detection, i.e., what is also called a communication-centric approach;

2. the usage of radar waveforms for communication purposes, i.e., what is also called a radar-centric approach;

3. the design from scratch of a totally new waveform for the upcoming 6G systems [8].

In this thesis, the first approach is considered, which consists of using for sensing applications signals originally designed for communication purposes. In particular, two different types of communication signals are taken into account, which are orthogonal frequency-division multiplexing (OFDM) and orthogonal time frequency space (OTFS). OFDM-based signals are widely employed in radio communications such as Wi-Fi, 4G, and 5G systems, and are considered a promising option for JSC systems, as highlighted in previous research by Braun [9].

Differently, OTFS is a novel bi-dimensional modulation technique that has recently gained a lot of interest for future mobile systems. The increasing interest in this new modulation is motivated by better communication performance than OFDM in high-mobility scenarios, which is one of the typical operating conditions required for future cellular networks [10]. Furthermore, OTFS modulation appears to have comparable performance to OFDM, regarding sensing tasks in JSC application, as shown in [11].

Moreover, in this dissertation, three different JSC system configurations, i.e., monostatic, bistatic, and multistatic, are considered. As it will be explained later, different from a monostatic system where transmitter (Tx) and receiver (Rx) are co-located, in a bi- or more generically multistatic system the Tx and the Rx(s) are separated in the space. This allows to avoid the problem of self-interference that usually afflicts monostatic systems [12].

1.1 Basic Radar System

Let us consider a generic single-input single-output (SISO) radar system that transmits a signal $s(t)$. The received equivalent low-pass (ELP) echo signal $r(t)$ consists of a superposition of reflections of the original signal by objects positioned in the way of $s(t)$'s wavefront, as well as of receiver noise. It can be written as

$$r(t) = \sum_{l=0}^{L-1} b_l s(t - \tau_l) e^{j 2\pi f_{\mathrm{D},l} t} + z(t) \tag{1.1}$$

where L is the number of reflections, also referred to as scatterers, b_l, τ_l and $f_{\mathrm{D},l}$ are the complex gain factor, the propagation delay and the Doppler shift associated to the l-th scatterer, respectively, while $z(t)$ is the Gaussian noise. When a monostatic setting is considered, i.e., Tx and Rx are co-located (as depicted in Fig. 1.1), the propagation delay $\tau_l = 2r_l/c$ is referred to as the round trip delay, with r_l the distance between the radar system and the scatterer l and c the speed of light. In particular, τ_l is the time required for the transmitted signal $s(t)$ to reach the object and return to the radar system where it is collected and processed to estimate the distance and velocity of the object/scatterer by estimating τ_l and $f_{\mathrm{D},l}$. The relationship between the Doppler shift and the radial velocity v_l of scatterer l, is given by $f_{\mathrm{D,l}} = (2v_l f_{\mathrm{c}})/c$, where f_{c} is the carrier frequency.

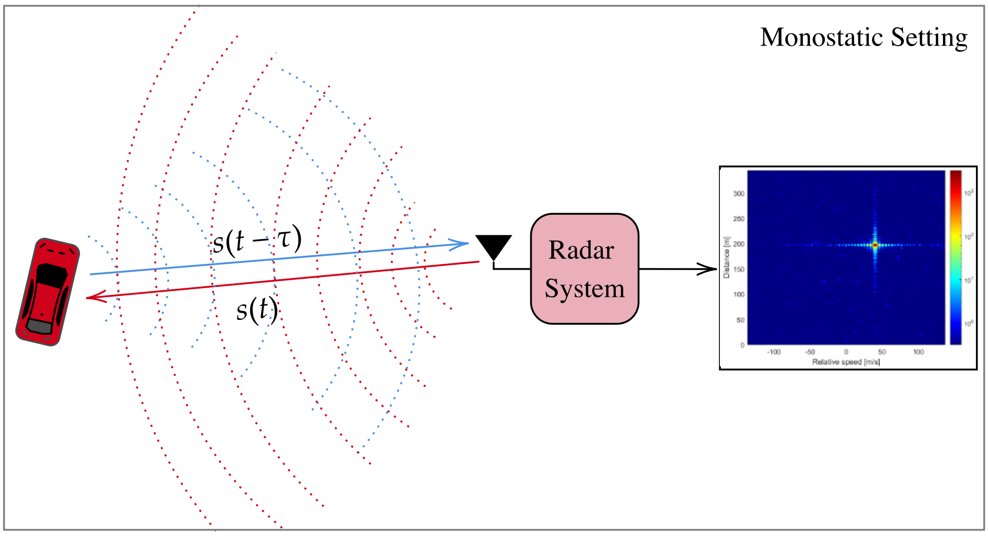

Figure 1.1: Schematic diagram of a monostatic radar system. The system acquires signals backscattered by objects in the environment and produces a radar map as an output by performing an estimation of target parameters (i.e., distance and velocity).

Differently, in a bistatic (multistatic) configuration, since the Tx and Rx are not colocated, the propagation time τ_l of the signal scattered by a target l is related to the distance between the Tx and the target, $R_{\mathrm{T},l}$, and that between the target and the Rx, $R_{l,\mathrm{R}}$, via the bistatic range $R_{\mathrm{bis},l} = R_{\mathrm{T},l} + R_{l,\mathrm{R}} = \tau_l \cdot c$ [13]. Moreover, for bi- and multistatic configurations, an additional phase term $e^{j\varphi_0}$ should be added for each path l in (1.1), where $\varphi_0 \in \mathcal{U}_{[0,2\pi)}$ is the phase offset between Tx and Rx that accounts for non-ideal synchronization (i.e., clock offset).

Starting from the received signal in (1.1), sensing parameter estimation can be approached through different methods. In this dissertation, we adopt a Maximum Likelihood (ML) approach as proposed in [14]. Details of the estimation procedure are given in the following chapters.

1.2 OFDM-based JSC systems

As previously stated, OFDM-based signals, widely employed in radio communications such as Wi-Fi, 4G, and 5G new radio (NR) systems, are considered a promising choice for JSC systems [9, 12, 15]. Notably, 5G NR waveforms have garnered significant attention due to their extensive channel bandwidths and adaptable subcarrier spacing, making them highly suitable for sensing applications [12]. In addition, the flexibility in resource allocation, i.e., time and frequency (see Fig. 1.2) of 5G NR systems could be exploited to easily integrate sensing as a service.

In the context of 5G NR networks, new operating bands have been established, encompassing millimeter wave (mmWave) frequencies, which offer the advantage of accommodating exceptionally wide channel bandwidths of up to 400 MHz. Literature on mmWave JSC demonstrates its feasibility and potentials in indoor and vehicle networks [17–23]. In particular, in-depth signal processing aspects of mmWave-based JSC with an emphasis on waveform design are provided by [17]. As it will be clarified later in this dissertation, having a wide bandwidth allows for improved resolution of the sensing systems in terms of distance or range estimation. In addition, the shorter wavelengths associated with mmWave bands allow the use of large antenna arrays, further increasing the resolution of radar systems. In particular, multiple-input multiple-output (MIMO) technology in JSC system can not only facilitate high-capacity communication links through techniques such as spatial multiplexing but also empower the sensing receiver to perform direction of arrival (DoA) estimation, which is the more accurate the higher the number of antennas in the array [24].

Another noteworthy characteristic of MIMO systems, which has garnered considerable attention in recent investigations concerning JSC with OFDM

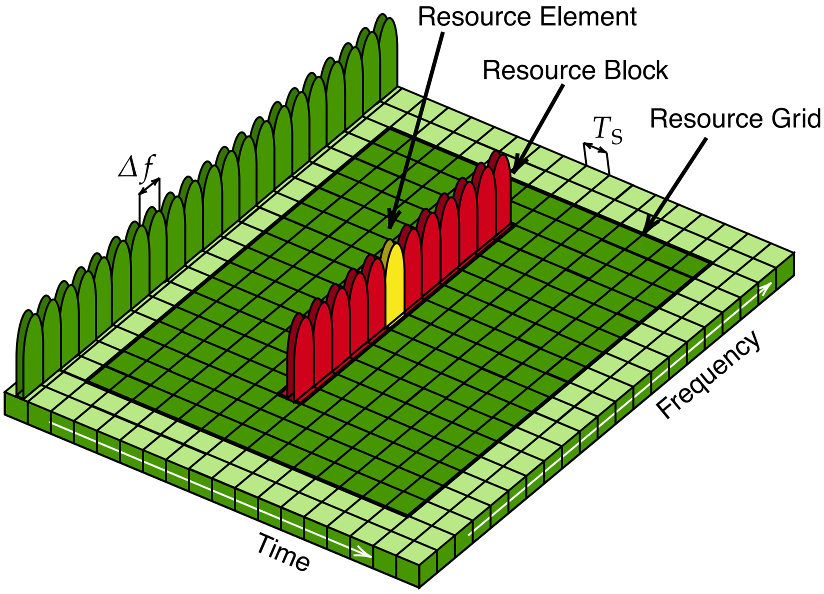

Figure 1.2: Example of representation of the time-frequency resources in a 5G NR system. The notation used refers to the 5G NR standard [16]. Δf is the subcarrier spacing, while T_s is the total OFDM symbol duration considering cyclic prefix. A resource block is composed of 12 subcarriers.

waveforms, is the capability to employ distinct, coexisting beams for communication and sensing purposes, driven by the disparate requirements of these two functionalities. For instance, in works such as those presented in Zhang et al. [18] and Barneto et al. [25], multibeam frameworks, similar to the one shown in Fig. 1.3, have been proposed. These frameworks involve the design and optimization of beamforming techniques to concurrently support a stable communication beam directed toward the user equipment (UE) and a sensing beam for environmental scanning. In particular, Zhang et al. [18] examine an OFDM-based mmWave system, wherein two nodes engage in two-way point-to-point communication using time-division duplexing (TDD) mode while simultaneously sensing the surroundings to ascertain the positions and velocities of nearby objects. Similarly, in the study by Barneto et al. [25], a system is proposed wherein a 5G base station (BS) operates as a dual-functional node, serving as both a radar and communication device at mmWave frequencies, employing multiple beams.

The main idea is to split the power of the transmitted OFDM signal

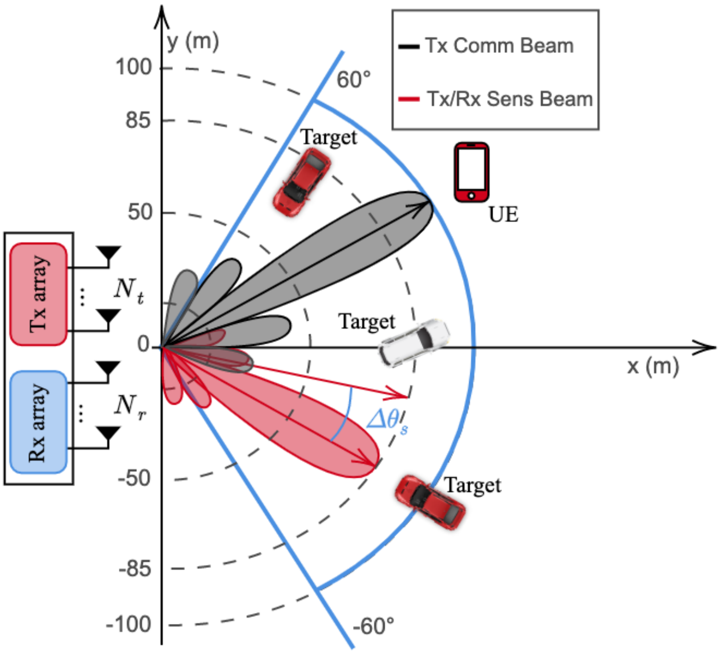

Figure 1.3: 5G NR-based sensor with multibeam capability for joint communication and sensing

between communication and sensing, namely, the total available power is in part exploited to sense the environment and in part directed to the UE. Therefore, the transmitting beamformer (BF), $\mathbf{w}_\mathrm{T}$ can be defined as

$$\mathbf{w}_\mathrm{T} = \sqrt{\rho}\,\mathbf{w}_\mathrm{T,s} + \sqrt{1-\rho}\,\mathbf{w}_\mathrm{T,c} \tag{1.2}$$

where $\rho \in [0, 1]$ is the parameter used to control the fraction of power apportioned to the two directions, while $\mathbf{w}_\mathrm{T,s}$ and $\mathbf{w}_\mathrm{T,c}$ are the communication and the sensing BFs, respectively. The choice of the BFs depends on the desired array response [26, 27].

This approach, characterized by the simultaneous presence of communication and sensing beams (i.e., multibeam system), is considered in part of the analysis conducted within this dissertation, specifically in Chapters 2, 3, and 4. Moreover, the possibility of performing a scan of the environment (in a predefined area) by sequentially moving the beam reserved for sensing in different spatial directions through $\mathbf{w}_\mathrm{T,s}$ is considered and explained in detail in Chapter 2.

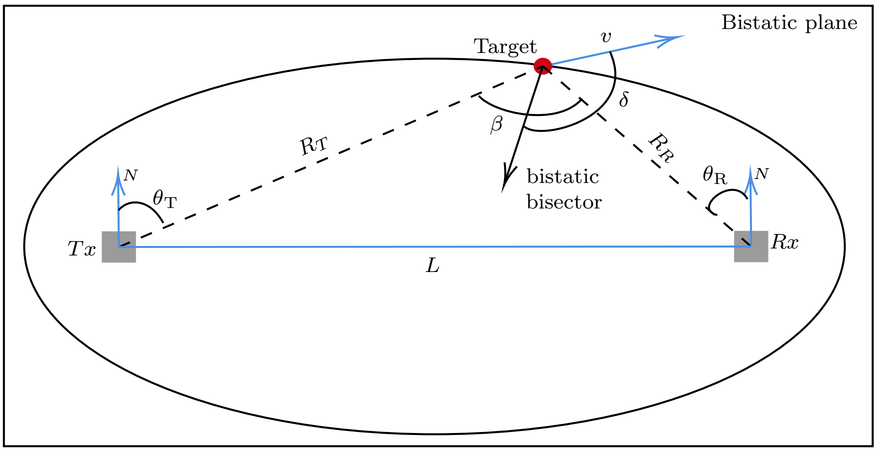

Figure 1.4: Illustration of a bistatic radar configuration. As it is explained in more detail in Chapter 4, in a bistatic configuration it is possible to localize the target on an ellipse starting from the estimation of the bistatic range, R_{bis}. To resolve the uncertainty and estimate the position of the target, it is necessary to estimate the angle θ_{R} using MIMO systems. Alternatively, it is possible to estimate the position by moving from a bistatic to a multistatic configuration, e.g. with one Tx and several Rxs, and fusing the information from different bistatic pairs.

1.2.1 Bi and multistatic JSC systems

It is important to notice that most of the recent research has shown the feasibility of using OFDM-based waveforms for JSC systems, especially focusing on the monostatic configuration, i.e., with Tx and Rx co-located [12, 14, 28]. For this type of configuration, a critical aspect is the self interference (SI) (as it will be shown in Chapter 3), which requires the full-duplex capability for which technology is not yet at a mature stage [12, 29]. SI is essentially a strong signal received directly from the transmitting antenna that has the potential to interfere with the weak signals reflected from objects.

In this regard, a possible solution to avoid this problem is to resort to a bistatic or multistatic configuration, where the Tx and Rx(s) are not co-located. Bi/multistatic radar setups are also interesting as they can extend the sensing area with a Rx that can be simple and mobile [30]. For this reason, in this thesis, the analysis initially explores a monostatic system based on OFDM for JSC. Subsequently, the investigation moves to a bistatic configuration and then to a multistatic one. A significant advantage of transitioning from bistatic to multistatic is the ability to leverage spatial diversity.

For example, improved detection performance can be achieved in a system with one Tx and two Rxs by observing the same target from different angles, especially when dealing with extended targets [31].

1.3 Joint Sensing and Communication in the Near Field

As mentioned in Section 1.2, mmWave bands allow the use of large antenna arrays and this can enable high-resolution radar functionality. Moreover, another interesting aspect related to the use of very large arrays is that for some users and radar targets very close to the Tx/Rx, the usual far-field propagation assumption (i.e., plane wavefront) common in most array processing literature when modeling the wireless channel (and used for the majority of the analysis performed throughout this dissertation) is no longer satisfied and a near-field channel model should be considered [32].

In contrast to the far-field channel model where the signal wavefront is approximated to be a plane, the near-field channel is modeled to account for a spherical wavefront. This creates a significant distinction between the two scenarios.

In far-field processing, target DoA and distance estimation relies on the array response and signal propagation delay, operating independently. Time delay estimation resolution, in this case, is constrained by the system bandwidth [9]. On the other hand, in the near-field regime, direct target localization is achievable without the need to estimate time delay. Instead, the phase of the signals scattered by the target and received by the antenna array elements is analyzed using the properties of spherical waves [33]. Consequently, the design of algorithms for communication and sensing in the near-field demands a specific approach. In the stat-of-the-art literature, some work can be found related to user localization in near-field scenarios especially considering reconfigurable intelligent surfaces, e.g., [34, 35]. Moreover, some recent works have considered JSC systems operating in the near-field [36]. However, it is now important to note that when considering a multistatic JSC system operating at mmWave in a given urban scenario, a given UE or target may be in the far-field for one of Txs or Rxs and in the far-field for the others at any given time. For this reason, it may be desirable to design a system that can easily switch from one scenario to another, i.e., which considers both near- and far-field. Moreover, as far as the near-field is concerned, it should be noted that the traditional beamforming approaches, where it is possible to illuminate a circular sector by steering the energy in a specific direction, are no longer optimal and the need arises to switch to a beamfocusing approach. This approach consists of focusing the energy on a specific range-angle region in the space. This occurs because a spherical wavefront allows for simultaneous control of both distance and angle, enabling illumination of a specific region [32]. Conversely, using traditional beamforming in the near-field results in a mismatch in the array response, as shown in Fig. 1.5.

In the following, the relationship (i.e., the boundary) between the near-field and far-field regions is explained.

1.3.1 Near/far-field region relationship

The boundary between near-field and far-field can be determined by the *Fraunhofer* distance (also called Rayleigh distance). For an antenna with maximum aperture D at wavelength λ, the Fraunhofer distance given by $D_{\mathrm{ff}} = \frac{2D^2}{\lambda}$ represents the minimum distance for guaranteeing the phase difference of received signals across the array elements of at most $\lambda/4$ [32]. For a ULA with N_{a} elements and $\lambda/2$ inter-element spacing, this equates to $N_{\mathrm{a}}^2\lambda/2$. This is widely considered the limit under which wave propagation under the planar assumption holds. The Fresnel distance D_{fr} given by $\sqrt[3]{\frac{D^4}{8\lambda}}$ is the distance beyond which the reactive field components of the antenna itself become negligible. The distance between D_{ff} and D_{fr} is known as the radiative near-field Fresnel region, or the near-field region for brevity.

It is important to note that when dealing with multicarrier modulation (e.g., OFDM or OTFS), the *Fraunhofer* distance is impacted by the wavelength of each component. The overall far-field regime of the system with a fixed array aperture can then be considered as the *Fraunhofer* distance of the highest frequency sub-carrier, i.e. $D_{\mathrm{ff}} = 2D^2/\min(\lambda_m)$. Figure 1.6 depicts

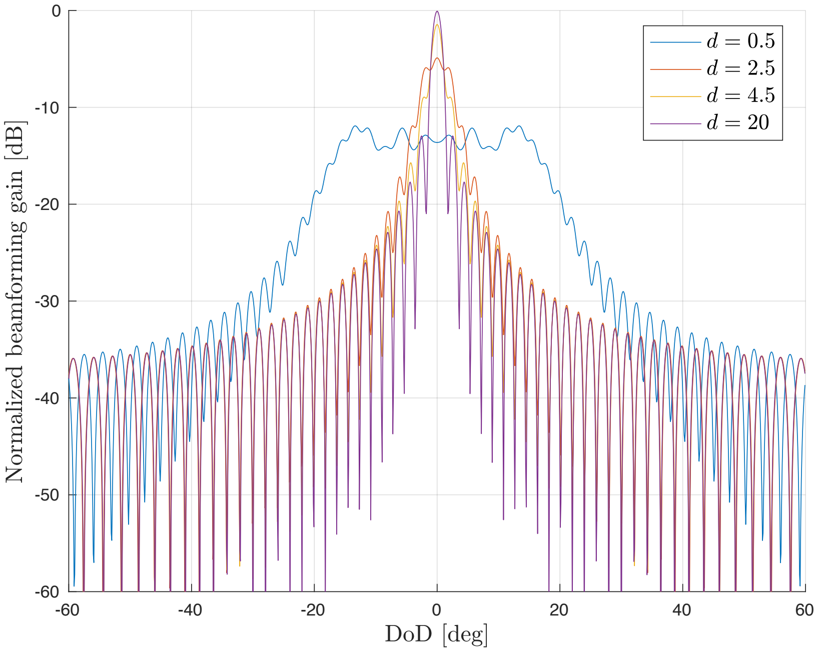

Figure 1.5: Mismatch in the array response for a system operating with a carrier frequency $f_c = 28\,\text{GHz}$. The direction of departure (DoD) of the user's signal computed with respect to the center of the array is 0°, while d, which represents the distance between a user and a uniform linear array (ULA) comprising 64 elements, is varied between 0.5 m, and 20 m. The Tx employs a traditional beamforming technique that steers the power toward the user's direction. It can be seen that when the user is very close to the antenna, using a traditional beam steering approach results in a mismatch in the array response. This mismatch becomes increasingly irrelevant as the user moves away from the array.

D_{ff} for a few mmWave carrier frequencies and bandwidths considering 100 OFDM subcarriers.

1.4 Joint Sensing and Communication with OTFS

Despite the fact that, as already stated, OFDM is an established reality in the field of mobile communications and seems to guarantee effective performance in JSC applications, the search for an even more performing and reliable modulation that can totally or partially replace OFDM in future cellular

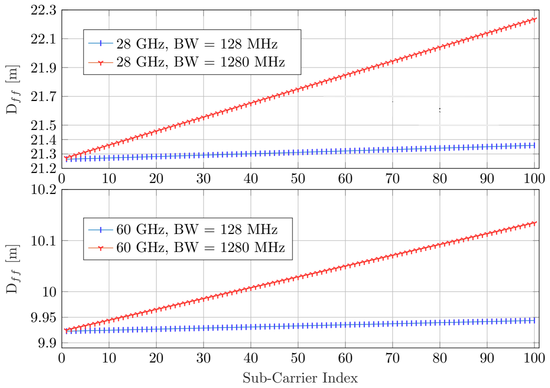

Figure 1.6: Far-field distance as a function of OFDM subcarrier index.

systems is still ongoing [37].

One of the possible candidates is OTFS, a novel bi-dimensional modulation technique that has recently gained a lot of interest for future mobile systems [38–41]. The increasing interest in OTFS is motivated by the higher spectral efficiency due to the absence of the cyclic prefix (CP) and by its robustness in high-mobility scenarios [38, 42]. Indeed, in channels with a wide range of Doppler frequencies, such modulation displays exhibit very high performance in terms of bit error rate (BER) [43–45]. Furthermore, OTFS modulation has also been seen to be particularly suitable in JSC scenarios [40, 42, 46, 47], showing comparable performance to OFDM, regarding sensing range and velocity estimation, as shown in [48] and [11], but with the possibility to detect targets at a larger distance (thus avoiding the limitation imposed by the CP) and to estimate their radial velocity on a broader interval [40, 47, 49, 50].

Unfortunately, OTFS modulation is particularly complex, making it challenging to implement efficiently [51–53]. As it will be explained in Chapter 6, this problem is even more exacerbated in JSC systems where sensing parameters must be estimated quickly to support real-time tracking. At the forefront, various approaches in the literature aim to reduce and manage the complexity of OTFS-based JSC systems.

In particular, in [11], authors propose an approximated maximum likelihood (ML) algorithm to estimate the range and velocity of the target through successive refinements by tightening the search step around the value estimated at the previous iteration. In [54], a mixed technique that couples the frequency modulated continuous wave (FMCW) signal, suffering from low data rate, with OTFS waveform, which suffers from high sensing complexity, is proposed. The paper demonstrates that the joint OTFS-FMCW waveform, obtained by exploiting the locality property of the FMCW in both time-frequency and delay-Doppler domains, achieves high data rates for communication while ensuring a low-complexity radar receiver. In [55], a low-complexity Bayesian learning algorithm for target parameter estimation is proposed for OTFS-based automotive radars, which leverages the structural sparsity of the radar channel in the delay-Doppler domain. Furthermore, the efficiency is further improved by dimension pruning of the measurement matrix in the OTFS radar signal model by incorporating prior knowledge of the motion parameter limit of the targets. Finally, in [56], authors present an efficient OTFS implementation based on the discrete Zak transform. In particular, the proposed formulation simplifies the derivation and analysis of the input-output relation of the time-frequency dispersive channel in the delay-Doppler domain.

1.5 Main Contributions

Most of the research efforts on JSC have so far been devoted to the design of signal processing techniques aimed at extracting features from the environment, such as the position and velocity of a target (for example, a car or a human being) or at inferring the environment itself, such as the mapping or imaging of a room. However, only a few works have investigated the performance of a JSC system, especially from the sensing perspective, and provided results in terms of target parameters estimation accuracy with current technology. For this reason, the first part of this dissertation, i.e., from Chapter 2 to Chapter 5, aims at addressing the analysis of JSC systems to understand the key aspects and their role in governing performance, considering OFDM-based signals with different radar settings (i.e., monostatic, bistatic, and multistatic). Several signal processing techniques applied directly to the downlink physical layer are considered to estimate the position (through DoA and distance estimation) and velocity of the targets. In particular, first, in Chapter 2 and Chapter 3, a fully digital MIMO monostatic JSC system based on 5G NR with multibeam capabilities is considered, both in the presence of single and multiple point-like targets. The analysis is then extended to a bistatic MIMO JSC system in Chapter 4. As already mentioned, this configuration, with Tx and Rx that are not co-located allows to avoid the problem of SI. An analysis of the coverage of the sensing system is performed in addition to an analysis of the root mean square error (RMSE) on target position and speed estimation. Subsequently, in Chapter 5, a MIMO multistatic configuration with one Tx and two Rxs with hybrid digital-analog (HDA) architectures is considered to exploit the spatial diversity for improved detection.

Unlike the previous analysis, in Chapter 5, we consider extended targets (ETs) and both near-field and far-field propagation conditions. The need to introduce a model for ET is related to the awareness that an extended real object (e.g., a car) is unlikely to produce a single reflection such that it can be seen as a point by the radar system. On the contrary, it is likely to be seen by the radar system as a series of scattered points. For this reason, a possible solution for modeling an ET is given.

Another important aspect is related to the considered propagation conditions. In fact, as explained in Section 1.3, the use of a very large antenna array enabled by mmWave bands leads to the need to consider the possibility that a target may be in the near-field of the antenna array, making far-field assumptions invalid and thus also an approach based on steering power to a specific angular sector no longer valid. For this reason, in Chapter 5, the analysis of the performance of the considered multistatic JSC system is performed by taking into account a general near/far-field channel model valid for JSC applications. It is shown that when the target is detected to be in the near-field of the Tx, a beamfocusing approach should be considered instead of a beamforming one to properly illuminate the target, namely to increase the signal-to-noise ratio (SNR) at the intended target location. This is also very important when the target is a UE. In this case, the use of a beamfocusing approach can lead to an increase in communication performance. Moreover, if the target is detected to be in the near-field of one of the Rx, performing ML estimation of the target parameters by considering a more accurate near/far-field channel model instead of a far-field-only one results in significantly improved estimation performance.

For what concerns the second part of this thesis, a JSC system based on OTFS modulation is considered. As mentioned in Section 1.4, OTFS is a novel and promising multicarrier modulation scheme that is currently one of the possible candidates for future mobile systems and it has shown good performance for JSC systems. However, this modulation is particularly expensive in terms of computational complexity, especially when used in JSC systems. Despite some attempts to reduce complexity, current solutions still seem ineffective, especially when fast estimation of target parameters is a stringent requirement for real-time tracking in complex environments. For this reason, this dissertation proposes a low-complexity implementation of the ML algorithm for estimating the target's distance and velocity parameters using OTFS signals. In particular, first, a monostatic SISO JSC system is considered and its computational complexity in performing sensing operations is analyzed. The system model and the ML estimation of the target parameters (i.e., distance and radial velocity) are first introduced in Chapter 6 (based on [11, 48]). Then, a novel low-complexity estimation and detection approach is presented and described in detail in Chapter 7. This approach is based on the approximation of the channel matrix, which contains information about target parameters, by a *Dirichlet* kernel analysis. The approximation criterion is designed for the channel matrix expression given in [11].

1.6 Thesis Organization and Notation

The rest of the thesis is organized as follows.

Chapter 2: a monostatic MIMO JSC system based on 5G NR with multibeam capabilities is considered. In particular, the system model and the signal processing techniques that we consider in our analysis are introduced, by detailing the considered transmitted and received signals, specifically focusing on the multibeam design at the transmitter side. Then, the signal processing techniques used to estimate distance, radial velocity, and DoA of targets are introduced. Finally, an algorithm is presented to remove phantom targets that appear due to the considered sensing method, which is based on beam scanning.

Chapter 3: an analysis of the sensing performance of the monostatic JSC system introduced in Chapter 2 is performed through numerical simulations. The analysis focuses first on the estimation performance in terms of RMSE of distance, radial velocity, and DoA estimates in single point-like target scenarios when the system operates at both sub-6 GHz and mmWave frequencies. Then, we evaluate the system performance when multiple targets are present, using the optimal sub-pattern assignment (OSPA) metric. Finally, we provide an in-depth investigation of the dominant factors that affect performance, including the fraction of power reserved for sensing.

Chapter 4: the RMSE analysis performed in Chapter 3 is extended by considering a bistatic JSC system, i.e., where Tx and Rx are not co-located, in a single point-like target scenario. In particular, the RMSE of DoA and bistatic range estimation is first studied by comparing two setups operating at sub-6 GHz, and mmWave frequencies. Then, the RMSE of the position estimation is studied through heatmaps computed in the monitored area. Finally, since a multibeam system is considered, as in Chapter 2, the sensing coverage limits of the bistatic system are studied, by varying the fraction of power devoted to sensing.

Chapter 5: the analysis presented in Chapter 3 and Chapter 4, in which monostatic and bistatic settings and point-like targets are considered, is extended by studying the performance of a MIMO OFDM-based JSC multistatic system in the presence of ETs and considering both near-field and far-field propagation conditions. In particular, an ET model and a general near/far field channel model are introduced. The considered multistatic system is made of one Tx and two Rxs in order to exploit spatial diversity to improve target detection. A beamfocusing approach is considered to improve sensing performance when the target is in the near-field of the Tx. Some numerical results in terms of RMSE and probability of detection are shown.

Chapter 6: the focus is shifted from OFDM modulation to OTFS, specifically introducing the system model and methods for estimating target parameters in a monostatic OTFS-based JSC system. The discussion draws from the research presented in [38,39], and [11].

Chapter 7: we propose a low-complexity detector for a JSC OTFS-based systems, based on efficient computation of the channel matrix introduced in Chapter 6. First, a priori localization of the elements of the channel matrix containing most of the information helpful in estimating the sensing parameters is performed. Then, an approximation criterion of the channel matrix based on the *Dirichlet kernel* is given. The proposed solution is validated through numerical simulations.

The following notation is adopted: capital boldface letters for matrices, lowercase bold letters for vectors, $(\cdot)^*$, $(\cdot)^\dagger$ and $(\cdot)^\mathrm{T}$ for conjugate, conjugate transpose and transpose of a vector/matrix respectively, $\lceil\cdot\rceil$, $\lfloor\cdot\rfloor$ for ceiling and floor functions, respectively. $|x|$ denotes the absolute value of x if $x \in \mathbb{R}$, while $|\mathcal{X}|$ denotes the cardinality of a set $|\mathcal{X}|$. Also, $\mathbb{E}\{\cdot\}$, $\mathrm{var}[\cdot]$ for mean value and variance operator respectively. Additionally, $\mathrm{frac}(x) = x - \lfloor x \rfloor$ represents the fractional (or decimal) part of a non-negative real number x, and $\left\|\cdot\right\|_p$ is the p-norm operator; $[n] = \{1, \ldots, n\}$ and $[0 : n] = \{0, 1, \ldots, n\}$ for a positive integer n; $\otimes$ denotes Kronecker product.

The dissertation is based on the research works in [57], [58], [59], [60], [61].

Chapter 2

Monostatic Joint Sensing and Communication with 5G NR

This Chapter focuses on the description of the system and channel models and the signal processing techniques that we consider for our analysis of a monostatic MIMO JSC system based on 5G NR with multibeam capabilities. In particular, first, in Section 2.1, the considered transmitted and received signals are detailed, specifically focusing on the multibeam design at the transmitter side. In fact, the considered system is a multibeam system with a beam pointing to the UE while the other one periodically scans the environment by sequentially pointing towards predetermined directions. The scan procedure is also introduced. Then, in Section 2.2, the signal processing techniques used to estimate the distance, radial velocity, and DoA of targets are introduced. Moreover, we propose an algorithm to remove phantom targets that appear because of the sensing method, which relies on beam-scanning impaired by beam sidelobes.

2.1 System Model

As depicted in Fig. 2.1, a multiple antennas OFDM system is considered. The JSC system consists of a Tx antenna array with N_{T} elements and of an Rx antenna array with N_{R} elements, used for communication and sensing, respectively. For both Tx and Rx we assume a ULA with half-wavelength

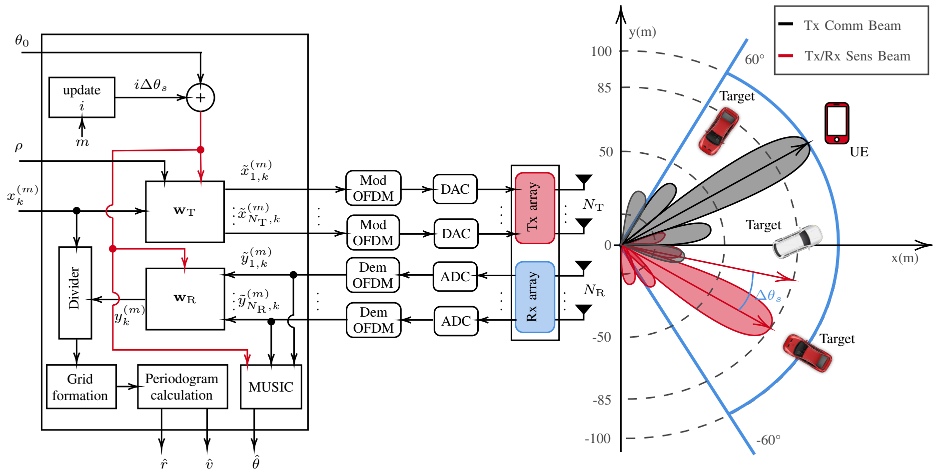

Figure 2.1: Block diagram of the 5G NR-based sensor with multibeam capability for joint communication and sensing.

separation, i.e., $d = \lambda_\mathrm{c}/2$ with $\lambda_\mathrm{c} = c/f_\mathrm{c}$, c the speed of light, and f_c the carrier frequency. The communication system transmits a 5G NR waveform with M OFDM symbols and K active subcarriers to a UE in the cell [62].[1] The ELP representation of the signal transmitted by the nth antenna can be written as

$$s_n(t) = \sum_{m=0}^{M-1} \left(\sum_{k=0}^{K-1} \tilde{x}_{n,k}^{(m)} e^{j2\pi \frac{k}{T} t} \right) g(t - mT_\mathrm{s}) \tag{2.1}$$

where $\tilde{x}_{n,k}^{(m)}$ is the modulation symbol, taken from a complex modulation alphabet, to be transmitted to the UE at the mth OFDM symbol and kth subcarrier, mapped through digital precoding at the nth transmitting antenna, $g(t)$ is the employed pulse, $\Delta f = 1/T$ is the subcarrier spacing, and T_s is the OFDM symbol duration including the CP.

2.1.1 Joint waveform

The vector $\tilde{\mathbf{x}}_k^{(m)} \in \mathbb{C}^{N_\mathrm{T}\times 1}$ is defined as $\tilde{\mathbf{x}}_k^{(m)} = \mathbf{w}_\mathrm{T} x_k^{(m)}$, where $\mathbf{w}_\mathrm{T} \in \mathbb{C}^{N_\mathrm{T}\times 1}$ is the precoder vector used to map each modulation symbol, $x_k^{(m)}$, to the transmitting antennas. In particular, we consider a multibeam system where

---

[1] Without loss of generality, we consider one user; however, during the scan period described in Section 2.1.3, the UE may change according to the multiple access rule established for communication.

the power of the OFDM signal to be transmitted is split between communication and sensing, namely, the total available power is in part exploited to sense the environment and in part directed to the UE [25,28]. Therefore, the transmitting BF vector $\mathbf{w}_\mathrm{T}$ can be written as [28]

$$\mathbf{w}_\mathrm{T} = \sqrt{\rho}\,\mathbf{w}_\mathrm{T,s} + \sqrt{1-\rho}\,\mathbf{w}_\mathrm{T,c} \tag{2.2}$$

where $\rho \in [0,1]$ is the parameter used to control the fraction of the total power apportioned to the two directions, while $\mathbf{w}_\mathrm{T,c}$ and $\mathbf{w}_\mathrm{T,s}$ are the communication and the sensing BF vectors, respectively. The latter are defined as[2] [62]

$$\mathbf{w}_\mathrm{T,c} = \frac{\sqrt{P_\mathrm{T} G^\mathrm{a}_\mathrm{T}}}{N_\mathrm{T}}\,\mathbf{a}^c_\mathrm{T}(\theta_\mathrm{T,c}) \tag{2.3}$$

$$\mathbf{w}_\mathrm{T,s} = \frac{\sqrt{P_\mathrm{T} G^\mathrm{a}_\mathrm{T}}}{N_\mathrm{T}}\,\mathbf{a}^c_\mathrm{T}(\theta_\mathrm{T,s}) \tag{2.4}$$

where G^a_T is the transmit array gain along the beam steering direction (where such a gain is maximum), $P_\mathrm{T} G^\mathrm{a}_\mathrm{T}$ is the effective isotropic radiated power (EIRP). Moreover, $\mathbf{a}_\mathrm{T}(\theta_\mathrm{T,c}) \in \mathbb{C}^{N_\mathrm{T}\times 1}$ and $\mathbf{a}_\mathrm{T}(\theta_\mathrm{T,s}) \in \mathbb{C}^{N_\mathrm{T}\times 1}$ are the steering vectors for communication and sensing, respectively, with $\theta_\mathrm{T,c}$ and $\theta_\mathrm{T,s}$ the DoDs for communication and sensing, respectively. The spatial steering vector for a ULA at a given DoA/DoD θ_l is [64, Chapter 9], [62, Chapter 5]

$$\mathbf{a}(\theta_l) = \left[1, e^{j2\pi d \sin(\theta_l)/\lambda_\mathrm{c}}, \dots, e^{j2\pi (N_\mathrm{a}-1) d \sin(\theta_l)/\lambda_\mathrm{c}}\right]^T \tag{2.5}$$

where N_a is the number of array antenna elements. Since a half-wavelength separation is considered, the expression (2.5) reduces to

$$\mathbf{a}(\theta_l) = [1, e^{j\pi \sin(\theta_l)}, \dots, e^{j\pi (N_\mathrm{a}-1) \sin(\theta_l)}]^T. \tag{2.6}$$

Looking at (2.2), it is evident the trade-off between the performance of the communication and sensing functions. To guarantee certain sensing ca-

---

[2] Without loss of generality, we perform a beam steering operation adopting a multi-beam approach for both sensing and communication. Other methods exist in the literature for beamforming, e.g., based on optimization techniques, further improving performance [20,63].

pabilities, it is necessary to reserve a fraction of the total power available for it, with a consequent reduction in communication coverage. To study how the communication system coverage changes by varying the EIRP, some metrics can be used according to the 3GPP Technical Report in [65]. In particular, maximum coupling loss (MCL), maximum path loss (MPL) and maximum isotropic loss (MIL) are the metrics used in 5G NR systems to express the coverage of the communication system [65, 66]. These metrics differ for some terms, but they share the main idea of maximum loss that the communication system can tolerate and still be operational. In particular, differently from MCL, MIL and MPL include also the antenna gains. Moreover, the MIL metric takes into account parameters such as shadow fading and penetration margins. A detailed analysis of this metric is out of the scope of this dissertation, but it is important to highlight that the fraction of power ρ reserved for sensing results in a reduction of MPL and MIL by a factor $10\log_{10}(\rho)$ dB.

2.1.2 Sensing received signal

The vector $\tilde{\mathbf{y}}_k^{(m)} \in \mathbb{C}^{N_\mathrm{R}\times 1}$ of the received modulation symbols at each antenna after the fast Fourier transform (FFT) block in the OFDM receiver, is given by

$$\tilde{\mathbf{y}}_k^{(m)} = \mathbf{H}_k^{(m)}\tilde{\mathbf{x}}_k^{(m)} + \tilde{\boldsymbol{\nu}}_k^{(m)} + \tilde{\mathbf{n}}_k \tag{2.7}$$

where $\mathbf{H}_k^{(m)} \in \mathbb{C}^{N_\mathrm{R}\times N_\mathrm{T}}$ is the channel matrix for the mth OFDM symbol and the kth subcarrier, $\tilde{\boldsymbol{\nu}}_k^{(m)} \in \mathbb{C}^{N_\mathrm{R}\times 1}$ is the vector whose elements represent the SI due to imperfect Tx–Rx isolation at each receiving antenna, and $\tilde{\mathbf{n}}_k \in \mathbb{C}^{N_\mathrm{R}\times 1}$ is the additive white Gaussian noise (AWGN) vector whose entries are independent, identically distributed (i.i.d.) random variables (r.v.s), having circularly symmetric zero mean Gaussian distribution with variance σ_N^2.

Considering L point target reflections, the channel matrix can be written as

$$\mathbf{H}_k^{(m)} = \sum_{l=1}^{L} \underbrace{\alpha_l e^{j2\pi m T_\mathrm{s} f_{\mathrm{D},l}} e^{-j2\pi k \Delta f \tau_l}}_{\triangleq \beta_l} \mathbf{a}_\mathrm{R}(\theta_l)\mathbf{a}_\mathrm{T}^T(\theta_l) \tag{2.8}$$

where τ_l, $f_{\mathrm{D},l}$, and θ_l are the round-trip delay, the Doppler shift, and the

DoA of the lth target, respectively. The term $\alpha_l = |\alpha_l| e^{j\phi_l}$ is the complex amplitude which includes phase shift and attenuation along the lth propagation path. The array response vector at the receiver for sensing is denoted in (2.8) by $\mathbf{a}_{\mathrm{R}}(\theta_l)$. To simplify the presentation of the DoA estimation method, (2.8) can be recast in the more compact form

$$\mathbf{H}_k^{(m)} = \mathbf{A}_{\mathrm{R}}(\boldsymbol{\theta})\boldsymbol{\Sigma}\mathbf{A}_{\mathrm{T}}^T(\boldsymbol{\theta}) \tag{2.9}$$

where $\mathbf{A}_{\mathrm{R}}(\boldsymbol{\theta}) = [\mathbf{a}_{\mathrm{R}}(\theta_1), \dots, \mathbf{a}_{\mathrm{R}}(\theta_L)] \in \mathbb{C}^{N_{\mathrm{R}} \times L}$ and $\mathbf{A}_{\mathrm{T}}(\boldsymbol{\theta}) = [\mathbf{a}_{\mathrm{T}}(\theta_1), \dots, \mathbf{a}_{\mathrm{T}}(\theta_L)] \in \mathbb{C}^{N_{\mathrm{T}} \times L}$ are the steering matrices for the targets' directions $\boldsymbol{\theta} = [\theta_1, \theta_2, \dots, \theta_L]$, and $\boldsymbol{\Sigma} = \mathrm{diag}(\beta_1, \beta_2, \dots, \beta_L) \in \mathbb{C}^{L \times L}$ is the diagonal matrix of the channel coefficients.

For what concerns the SI term, $\tilde{\boldsymbol{\nu}}_k^{(m)}$, in (2.7), each element n of this vector can be considered as the signal scattered by a static target with an almost null distance from the receiver, i.e., with $f_{\mathrm{D,SI}} = 0$ and $\tau_{\mathrm{SI}} = 0$, thus it can be written as $\tilde{\nu}_{n,k}^{(m)} = \alpha_{\mathrm{SI},n} x_k^{(m)}$, where $\alpha_{\mathrm{SI},n} = |\alpha_{\mathrm{SI},n}| e^{j\phi_{\mathrm{SI},n}}$ is the complex amplitude, which includes phase shift and attenuation of the SI contribution at the nth receiving antenna element [12, 67]. As for the targets, all the attenuation factors $\alpha_{\mathrm{SI},n}$ are assumed to be the same for all the receiving antennas. Therefore, the signal-to-self interference ratio (SSIR) for the eco generated by the target l at each receiving antenna is given by

$$\mathrm{SSIR} = \frac{|\alpha_l|^2}{|\alpha_{\mathrm{SI}}|^2}. \tag{2.10}$$

Starting from (2.7), by performing spatial combining through the receiving BF vector, $\mathbf{w}_{\mathrm{R}} = \mathbf{a}_{\mathrm{R}}^c(\theta_{\mathrm{R,s}})$, we have the received symbol $y_k^{(m)} = \mathbf{w}_{\mathrm{R}}^T \tilde{\mathbf{y}}_k^{(m)}$, which, using (2.9), can be expressed as

$$y_k^{(m)} = \mathbf{w}_{\mathrm{R}}^T \mathbf{A}_{\mathrm{R}}(\boldsymbol{\theta})\boldsymbol{\Sigma}\mathbf{A}_{\mathrm{T}}^T(\boldsymbol{\theta})\tilde{\mathbf{x}}_k^{(m)} + \mathbf{w}_{\mathrm{R}}^T \tilde{\boldsymbol{\nu}}_k^{(m)} + \mathbf{w}_{\mathrm{R}}^T \tilde{\mathbf{n}}_k. \tag{2.11}$$

2.1.3 Beam-scanning

As mentioned above, the considered system is a multibeam JSC scheme, with a beam pointing to the UE and a beam pointing sequentially to different directions to sense the environment.

Referring to Fig. 2.1, during a scan the DoD and the DoA for sensing are the same. Specifically, we have

$$\theta_{\mathrm{T,s}} = \theta_{\mathrm{R,s}} = \theta_0 + i\,\Delta\theta_{\mathrm{s}} \qquad i = 0, \dots, N_{\mathrm{dir}} - 1 \tag{2.12}$$

where θ_0 is the starting scan direction, $\Delta\theta_{\mathrm{s}}$ is the scan angle step, i is the index used to update the direction, and N_{dir} is the number of directions explored to perform a complete scan from $-\theta_0$ to θ_0. For each sensing direction, a number of OFDM symbols $M_{\mathrm{s}} < M$ is acquired from the receiver system. Therefore, since a 5G NR frame with M symbols lasts $T_{\mathrm{f}} = 10$ ms, by fixing N_{dir} it is possible to determine the number of frames and the time required to complete a scan as:

$$N_{\mathrm{f}} = \left\lceil \frac{M_{\mathrm{s}} N_{\mathrm{dir}}}{M} \right\rceil, \qquad T_{\mathrm{scan}} = T_{\mathrm{f}} N_{\mathrm{f}}. \tag{2.13}$$

The OFDM symbols collected in each direction are used to estimate range, Doppler and DoA of the target.

2.1.4 Sensor-target-sensor path

In line-of-sight (LoS) propagation conditions the power received at a given array element from the lth path, illuminated by the sensing beam, is proportional to $|\alpha_l|^2$ and given by [64]

$$P_{\mathrm{R},l} = \rho \cdot \frac{P_{\mathrm{T}} G_{\mathrm{T}}^{\mathrm{a}} G_{\mathrm{R}} c^2 \sigma_{\mathrm{RCS},l}}{(4\pi)^3 f_{\mathrm{c}}^2 d_l^4} \cdot \gamma_l \tag{2.14}$$

where $\sigma_{\mathrm{RCS},l}$ is the radar cross-section (RCS) of the point target l, d_l is the distance between the lth target and the BS, G_{R} is the single element antenna gain at Rx, and $\gamma_l = |\mathrm{AF}(\theta_{\mathrm{T,s}} - \theta_l)|^2 \in [0, 1]$ where $\mathrm{AF}(\theta)$ is the normalized array factor at Tx that considers the non-perfect alignment between the target DoA and the sensing direction [68]; when $\theta_l = \theta_{\mathrm{T,s}}$ then $\gamma_l = 1$. The SNR at the single receiving antenna element related to the lth target is defined as

$$\mathrm{SNR}_l = \frac{P_{\mathrm{R},l}}{N_0 K \Delta f} \tag{2.15}$$

where $P_{\mathrm{R},l}$, the received power from the lth path, is given in (2.14), and N_0 is the one-sided noise power spectral density (PSD) at each antenna element. When convenient, by normalizing to unit-power the transmitted symbols, i.e., $\mathbb{E}\{|x_k^{(m)}|^2\} = 1$, and ignoring the path-loss (2.15) reduces to $\mathrm{SNR}_l = 1/\sigma_\mathrm{N}^2$.

2.2 Estimation of Target Parameters and Detection

This section introduces multiple signal classification (MUSIC) for DoA estimation and periodogram-based frequency estimation for range and velocity evaluation. The estimation methods are performed for each sensing beam step in which M_s OFDM symbols are collected. To simplify the notation we drop the scan index i.

2.2.1 Estimation of the number of targets and DoAs

DoA estimation is performed by MUSIC that requires knowledge of the noise subspace, which in turn needs the number of targets to be known. Noise subspace can be identified via the covariance matrix of the received vector (2.7) $\mathbf{R} = \mathbb{E}\{\tilde{\mathbf{y}}_k^{(m)} \tilde{\mathbf{y}}_k^{(m)\dagger}\} \in \mathbb{C}^{N_\mathrm{R} \times N_\mathrm{R}}$. In fact, since the noise is zero mean and independent of the target echoes, it follows that the $N_\mathrm{R} - L$ smallest eigenvalues of $\mathbf{R}$ are all equal to the noise power σ_N^2 and the corresponding eigenvectors identify the noise subspace.[3] Since the covariance matrix is not known a priori, the sample covariance matrix (SCM) can be used instead [29]. It is given by

$$\widehat{\mathbf{R}} = \frac{1}{K M_\mathrm{s}} \sum_{m=0}^{M_\mathrm{s}-1} \sum_{k=0}^{K-1} \tilde{\mathbf{y}}_k^{(m)} \tilde{\mathbf{y}}_k^{(m)\dagger}. \tag{2.16}$$

The number of sources (target echoes in our scenario) can be estimated by model order selection based on information theoretic criteria [69,70]. The approach starts by performing eigenvalue decomposition of the SCM of the observed vectors, $\widehat{\mathbf{R}} = \mathbf{U}\boldsymbol{\Lambda}\mathbf{U}^\dagger$, where the columns of $\mathbf{U} \in \mathbb{C}^{N_\mathrm{R} \times N_\mathrm{R}}$ are the

---

[3] As required by MUSIC we consider $L < N_\mathrm{R}$, i.e, the number of targets is less than the number of sensing array elements.

eigenvectors and $\mathbf{\Lambda} = \mathrm{diag}(\lambda_1, \dots, \lambda_{N_\mathrm{R}})$ is a diagonal matrix with eigenvalues sorted in descending order, i.e., $\lambda_1 \geq \lambda_2 \geq \cdots \geq \lambda_{N_\mathrm{R}}$. Using the minimum description length (MDL) criterion, the estimated number of targets (considering that we are illuminating only targets within the sensing beam in the ith direction) is

$$L_\mathrm{m} = \underset{s \in \{0,\dots,N_\mathrm{R}-1\}}{\arg\min} \{\mathrm{MDL}(s)\} \tag{2.17}$$

with

$$\begin{aligned}\mathrm{MDL}(s) = &-\ln\left(\frac{\prod_{i=s+1}^{N_\mathrm{R}} \lambda_i^{1/(N_\mathrm{R}-s)}}{\frac{1}{N_\mathrm{R}-s}\sum_{i=s+1}^{N_\mathrm{R}} \lambda_i}\right)^{(N_\mathrm{R}-s)KM_\mathrm{s}} \\ &+ \frac{1}{2}s(2N_\mathrm{R}-s)\ln(KM_\mathrm{s}).\end{aligned} \tag{2.18}$$

The MUSIC algorithm then starts from $\widetilde{\mathbf{U}} \in \mathbb{C}^{N_\mathrm{R} \times (N_\mathrm{R}-L_\mathrm{m})}$, the submatrix containing the $N_\mathrm{R} - L_\mathrm{m}$ eigenvectors corresponding to the smallest eigenvalues, $\lambda_{L_\mathrm{m}+1}, \dots, \lambda_{N_\mathrm{R}}$, where such eigenvectors represent a good approximation of the noise subspace. Next, the pseudo-spectrum function, whose peaks reveal the presence of incoming signals, can be obtained as [71]

$$f_\mathrm{m}(\theta) = \frac{1}{\left\|\widetilde{\mathbf{U}}^\dagger \mathbf{a}(\theta)\right\|_2^2}. \tag{2.19}$$

The peak locations in $f_\mathrm{m}(\theta)$ are the DoA estimates $\widehat{\theta}$. However, as it will be better explained in Section 3.2, in each sensing direction we search for a local maximum of (2.19) in a limited angle range $[\theta_\mathrm{min}, \theta_\mathrm{max}]$, which depends on the beamwidth of the array response. The DoA estimate in each direction is thus given by

$$\widehat{\theta} = \underset{\theta \in [\theta_\mathrm{min}, \theta_\mathrm{max}]}{\arg\max} \{f_\mathrm{m}(\theta)\}. \tag{2.20}$$

2.2.2 Detection and range-Doppler estimation

For the range-Doppler profile evaluation, we start from the received symbols (2.11) from which, by expanding the matrix multiplications, we obtain

$$y_k^{(m)} = \left(\sum_{l=1}^{L} \beta_l \Upsilon(\theta_{\mathrm{T,s}}, \theta_{\mathrm{R,s}}, \theta_l) \right) x_k^{(m)} + n_k \tag{2.21}$$

where $n_k = \mathbf{w}_{\mathrm{R}}^T \tilde{\mathbf{n}}_k$ and $\Upsilon(\theta_{\mathrm{T,s}}, \theta_{\mathrm{R,s}}, \theta_l) \in \mathbb{C}$ is a factor which accounts for the gain due to the array response vector at Tx and Rx and the DoA of the target. Since the range and velocity of targets are embedded in β_l, first, a division is performed to remove the unwanted data symbols [9], i.e., $g_k^{(m)} = y_k^{(m)}/x_k^{(m)}$, which leads to

$$g_k^{(m)} = \sum_{l=1}^{L} \alpha_l e^{j2\pi m T_{\mathrm{s}} f_{\mathrm{D},l}} e^{-j2\pi k \Delta f \tau_l} \Upsilon(\theta_{\mathrm{T,s}}, \theta_{\mathrm{R,s}}, \theta_l) + \nu_k \tag{2.22}$$

where $\nu_k = n_k/x_k^{(m)}$. Note that (2.22) contains, for each target, two complex sinusoids whose frequencies are related to $f_{\mathrm{D},l}$ and τ_l, while α_l and $\Upsilon(\theta_{\mathrm{T,s}}, \theta_{\mathrm{R,s}}, \theta_l)$ are constant terms.

Starting from (2.22), a periodogram can be computed in order to estimate range and speed of the target as [9, 12, 14]

$$\mathcal{P}(q,p) = \left| \sum_{k=0}^{K_{\mathrm{p}}-1} \left(\sum_{m=0}^{M_{\mathrm{p}}-1} g_k^{(m)} e^{-j2\pi \frac{mp}{M_{\mathrm{p}}}} \right) e^{j2\pi \frac{kq}{K_{\mathrm{p}}}} \right|^2 \tag{2.23}$$

with $q = 0, \ldots, K_{\mathrm{p}} - 1$ and $p = 0, \ldots, M_{\mathrm{p}} - 1$, which consists of K FFTs of length M_{p} and M_{s} inverse fast Fourier transforms (IFFTs) of length K_{p}. In this analysis, $K_{\mathrm{p}} > K$ is calculated as the next power of two of K, whereas $M_{\mathrm{p}} > M_{\mathrm{s}}$ is the next power of two of $F_{\mathrm{p}} \cdot M_{\mathrm{s}}$, where F_{p} is the zero-padding factor to improve speed estimation resolution.

The periodogram (2.23) represents the range-Doppler map from which the first operation performed is target detection by a hypothesis test between H_0, where only the noise is present, and H_1, which refers to the presence of the target, i.e.,

$$\mathcal{P}(q,p) \underset{H_0}{\overset{H_1}{\gtrless}} \eta. \tag{2.24}$$

The threshold η is chosen to ensure a predefined false alarm probability P_{FA}. When the sensing beamwidth is relatively small, only one target is likely to be present in a given sensing direction, and if the test (2.24) rejects the null hypothesis, it is easy to find the location of the peak in the periodogram

$$(\widehat{q},\widehat{p}) = \underset{(q,p)}{\arg\max}\{\mathcal{P}(q,p)\} \tag{2.25}$$

and evaluate the distance and radial velocity of the target as

$$\widehat{r} = \frac{\widehat{q}\,c}{2\Delta f K_{\mathrm{p}}}, \qquad \widehat{v} = \frac{\widehat{p}\,c}{2f_{\mathrm{c}}T_{\mathrm{s}}M_{\mathrm{p}}}. \tag{2.26}$$

The distance and velocity resolutions are intrinsic characteristics of the periodogram and only depend on the 5G NR parameters, i.e., number of OFDM symbols, number of active subcarriers, subcarrier spacing, and OFDM symbol duration, and are given by [9, Chapter 3]

$$\Delta r = \frac{c}{2\Delta f K_{\mathrm{p}}}, \qquad \Delta v = \frac{c}{2f_{\mathrm{c}}T_{\mathrm{s}}M_{\mathrm{p}}}. \tag{2.27}$$

2.2.3 Pruning redundant target points

As explained above, the considered JSC system searches for a peak in the pseudo-spectrum (2.19) and in the periodogram (2.23) for each sensing direction for which the test (2.24) chooses the hypothesis H_1. When a target is detected in a particular direction, it might be detected also in some adjacent directions when the periodogram $\mathcal{P}$ is above threshold because of the beam sidelobes. These detected points are originated by the same target and are characterized by inaccurate DoA estimates. As it will be better quantified in Section 3.2, this effect is due to the choice of searching the maximum of MUSIC pseudo-spectrum in a limited range, as in (2.20), that reduces the computational cost of searching but may yield multiple detection points per target. To maintain the benefits of local search, we propose a method to thin

Algorithm 1 Pruning redundant target points

```
Require: $\mathbf{Z} \leftarrow \mathbf{z}_i = [\widehat{r}_i, \widehat{v}_i, \mathcal{P}(\widehat{r}_i, \widehat{v}_i), \widehat{\theta}_i, f_{\mathrm{m}}(\widehat{\theta}_i)]$
$\mathbf{Z}_{\mathrm{sort}} \leftarrow$ sort $\mathbf{Z}$ in decreasing order according to the 3rd column
$\mathbf{z}_{\mathrm{prun},1} \leftarrow \mathbf{z}_{\mathrm{sort},1}$        ▷ copy first row of $\mathbf{Z}_{\mathrm{sort}}$ in $\mathbf{Z}_{\mathrm{prun}}$
$k \leftarrow 1$        ▷ initialize row index of $\mathbf{Z}_{\mathrm{prun}}$
for $i = 2 : N_{\mathrm{max}}$ do
    count $\leftarrow 0$
    for $j = 1 : k$ do
        if $\widehat{r}_{\mathrm{prun},j} - \epsilon_{\mathrm{r}} \leq \widehat{r}_{\mathrm{sort},i} \leq \widehat{r}_{\mathrm{prun},j} + \epsilon_{\mathrm{r}}$ and
        $\widehat{v}_{\mathrm{prun},j} - \epsilon_{\mathrm{v}} \leq \widehat{v}_{\mathrm{sort},i} \leq \widehat{v}_{\mathrm{prun},j} + \epsilon_{\mathrm{v}}$ then
            count $\leftarrow$ count $+ 1$
            break
        end if
    end for
    if count $= 0$ then
        $k \leftarrow k + 1$        ▷ update row index of $\mathbf{Z}_{\mathrm{prun}}$
        $\mathbf{z}_{\mathrm{prun},k} \leftarrow \mathbf{z}_{\mathrm{sort},i}$
    end if
end for
$\widehat{L} \leftarrow k$
Output: $\mathbf{Z}_{\mathrm{prun}}$ and its number of rows, $\widehat{L}$
```

out redundant target points (hereafter also referred to as repeated targets) that has proven effective.

First, all the collected peaks and estimates are organized in a matrix $\mathbf{Z}$, whose rows are the vectors

$$\mathbf{z}_i = \left[\widehat{r}_i, \widehat{v}_i, \mathcal{P}(\widehat{r}_i, \widehat{v}_i), \widehat{\theta}_i, f_{\mathrm{m}}(\widehat{\theta}_i)\right] \quad i = 1, \ldots, N_{\mathrm{max}} \tag{2.28}$$

where $N_{\mathrm{max}} \leq N_{\mathrm{dir}}$ is the number of sensing directions in which the test (2.24) rejects the null hypothesis. Subsequently, these rows are sorted in descending order with respect to the values, $\mathcal{P}(\widehat{r}_i, \widehat{v}_i)$, to form a new matrix $\mathbf{Z}_{\mathrm{sort}}$. Finally, a check on the elements of $\mathbf{Z}_{\mathrm{sort}}$ is performed to remove redundant target points, i.e., those with very similar estimates of both distance and radial velocity (within a given range of uncertainty). This results in a new matrix

$\mathbf{Z}_{\text{prun}}$ with a number of rows $\widehat{L} \leq N_{\text{max}}$.[4] The sort operation ensures that only range and speed pairs associated with the largest values of the periodogram are kept between the repeated points. The whole procedure is detailed in Algorithm 1. As it can be seen, the definition of *redundant target point* is linked to the choice of two parameters, ϵ_{r}, and ϵ_{v}, that account for the measurement uncertainty. In particular, in the algorithm a target indexed with i is considered a repetition of an already detected target denoted with j if its estimated range, $\widehat{r}_i$, and velocity, $\widehat{v}_i$, meet the conditions, $\widehat{r}_j - \epsilon_{\text{r}} \leq \widehat{r}_i \leq \widehat{r}_j + \epsilon_{\text{r}}$, and $\widehat{v}_j - \epsilon_{\text{v}} \leq \widehat{v}_i \leq \widehat{v}_j + \epsilon_{\text{v}}$, respectively. The choice of the two parameters ϵ_{r} and ϵ_{v} will be discussed in Section 3.2.

---

[4] Note that $\widehat{L}$ is the estimated number of targets in our approach. This value may differ from L_{m} given by (2.17) because the number of targets detected by MUSIC is conditioned on the considered sensing direction. After all, Tx beamforming performs spatial filtering, illuminating predominantly targets within the beamwidth.

Chapter 3

System-Level Analysis of a Monostatic JSC System

In this chapter, an analysis of the sensing performance of the monostatic JSC system with multibeam capabilities introduced in Chapter 2 is performed through numerical simulations. The considered system is used to estimate the range, radial velocity, and DoA of multiple targets and can operate at both sub-6 GHz and mmWave frequencies.

In particular, we provide a detailed analysis of how the system performance is affected by the portion of the total radiated power used for sensing, by analyzing the RMSE of position estimate (obtained by target localization via range and DoA estimation) and the accuracy of radial velocity estimation for the single-target scenario. Furthermore, we propose an algorithm to remove phantom targets that appear because of the sensing method introduced in Chapter 2, which relies on beam-scanning impaired by beam sidelobes, and we use the OSPA metric to study the performance of the considered system for the multi-target scenario at mmWave frequencies.

3.1 Performance Evaluation in the Presence of Multiple Targets

This section introduces the performance metric employed to address the concept of miss-distance, or error, in a multi-target system. In particular, when considering a multi-object system, a consistent metric should capture the difference between two sets of vectors (the truth and the estimated), not only in terms of localization error but also in terms of cardinality error. For this reason, in this analysis, the OSPA metric [72], [73] is used to study the performance of the considered JSC system in a multi-target scenario.

The OSPA metric is a miss-distance indicator, which summarizes in a unique measure the estimation accuracy in both the number and location of the targets. More precisely, given the true positions of the L targets, $\mathbf{P} = [\mathbf{p}_1, \ldots, \mathbf{p}_L]$, with $\mathbf{p}_l = (x_l, y_l) = (r_l \cos\theta_l, r_l \sin\theta_l)$,[1] and the $\widehat{L}$ estimates, $\widehat{\mathbf{P}} = \left[\widehat{\mathbf{p}}_1, \ldots, \widehat{\mathbf{p}}_{\widehat{L}}\right]$, the distance between an arbitrary pair of the estimate and the true position, cut off at $\bar{c} > 0$, is defined as [72]

$$d^{(\bar{c})}\left(\mathbf{p}, \widehat{\mathbf{p}}\right) = \min\left\{\bar{c}, d\left(\mathbf{p}, \widehat{\mathbf{p}}\right)\right\} \tag{3.1}$$

where $d\left(\mathbf{p}, \widehat{\mathbf{p}}\right) = \left\|\mathbf{p} - \widehat{\mathbf{p}}\right\|_2$ is the Euclidean distance between the estimate and the true position, and $\bar{c}$ is the cutoff parameter that determines how the metric penalizes cardinality error with respect to the localization one. Denoting by Π_k the set of permutations on $\{1, 2, \ldots, k\}$ for any $k \in \mathbb{N}$, for $1 \leq q \leq \infty$ and $\bar{c} > 0$, the OSPA metric of order q and with cutoff $\bar{c}$ is defined as [72]

$$\begin{aligned} &\bar{d}_q^{(\bar{c})}\left(\mathbf{P}, \widehat{\mathbf{P}}\right) = \\ &\left(\frac{1}{\widehat{L}}\left(\min_{\pi \in \Pi_{\widehat{L}}} \sum_{l=1}^{L} \left(d^{(\bar{c})}\left(\mathbf{p}_l, \widehat{\mathbf{p}}_{\pi(l)}\right)\right)^q + \bar{c}^q(\widehat{L} - L)\right)\right)^{1/q} \end{aligned} \tag{3.2}$$

if $L \leq \widehat{L}$, and $\bar{d}_q^{(\bar{c})}\left(\mathbf{P}, \widehat{\mathbf{P}}\right) = \bar{d}_q^{(\bar{c})}\left(\widehat{\mathbf{P}}, \mathbf{P}\right)$ if $L > \widehat{L}$. Essentially, for $L \leq \widehat{L}$, the OSPA distance can be obtained by the following steps:

1. Find the L-elements subset of $\widehat{P}$ that has the shortest distance to P, corresponding to the optimal subset assignment;
2. If a point $\widehat{\mathbf{p}}_n \in \widehat{\mathbf{P}}$ is not paired with any point in $\mathbf{P}$, let $d_n = \bar{c}$; otherwise, d_n is the minimum value between $\bar{c}$ and the distance between

---

[1] From now on, and without loss of generality, the monostatic sensor is considered at the origin of a Cartesian coordinate system.

the two points in a pair;

3. The OSPA distance is given by $\bar{d}_q^{(\bar{c})}\left(\mathbf{P},\widehat{\mathbf{P}}\right) = \left(\left(\sum_{l=1}^{L} d_n^q\right)/\widehat{L}\right)^{1/q}$.

The OSPA distance can be interpreted as a qth order *per-target* error for a multi-object scenario. The metric can be divided into two components, one accounting for localization error and the other for cardinality error. In particular, for $q < \infty$ these components are given by [72]

$$\begin{aligned} \bar{e}_{q,\mathrm{loc}}^{(\bar{c})}(\mathbf{P},\widehat{\mathbf{P}}) &= \left(\frac{1}{\widehat{L}}\min_{\pi\in\Pi_{\widehat{L}}}\sum_{l=1}^{L}\left(d^{(\bar{c})}\left(\mathbf{p}_l,\widehat{\mathbf{p}}_{\pi(l)}\right)\right)^q\right)^{1/q}, \\ \bar{e}_{q,\mathrm{card}}^{(\bar{c})}(\mathbf{P},\widehat{\mathbf{P}}) &= \left(\frac{\bar{c}^q(\widehat{L}-L)}{\widehat{L}}\right)^{1/q} \end{aligned} \tag{3.3}$$

if $L \leq \widehat{L}$, and $\bar{e}_{q,\mathrm{loc}}^{(\bar{c})}(\mathbf{P},\widehat{\mathbf{P}}) = \bar{e}_{q,\mathrm{loc}}^{(\bar{c})}(\widehat{\mathbf{P}},\mathbf{P})$, $\bar{e}_{q,\mathrm{card}}^{(\bar{c})}(\mathbf{P},\widehat{\mathbf{P}}) = \bar{e}_{q,\mathrm{card}}^{(\bar{c})}(\widehat{\mathbf{P}},\mathbf{P})$ if $L > \widehat{L}$.

In the metric, the value of q determines the sensitivity of the $\bar{d}_q^{(\bar{c})}$ to outlier estimates, while $\bar{c}$ balances the cardinality error component with respect to the localization one, as a part of the total error. As $\bar{c}$ decreases, the localization error becomes dominant compared with the cardinality error, whereas larger values of $\bar{c}$ emphasize the latter. The best choice for $\bar{c}$ to maintain a balance between the two components is any value significantly larger than a typical localization error, but significantly smaller than the maximum distance between objects.

3.2 System-Level Analysis

System-level analysis is carried out through numerical simulations to evaluate the performance of the JSC scheme described in Chapter 2. For all the simulations, 5G NR signals compliant with 3GPP Technical Specification in [16] are considered. The main 5G NR parameters employed for the generation of the standardized signals are summarized in Table 3.1. In addition, a quadrature phase shift keying (QPSK) modulation alphabet is used for the generation of the OFDM signal. As shown in Fig. 2.1, the considered system scans the environment in the range $[-\theta_0, \theta_0]$, with $\theta_0 = -60°$, and a step

Table 3.1: JSC system parameters

5G specification →	NR 100	NR 400		
f_c [GHz]	3.5	28		
Δf [kHz]	30	120		
Active subcarriers K	3276	3168		
OFDM symbols per frame M	280	1120		
OFDM symbols per direction M_s	112	112		
Number of antennas $N_\mathrm{T} = N_\mathrm{R}$	10	10	50	100
Array beamwidth $\Delta\Theta$ [°]	27	27	5.3	2.6

$\Delta\theta_\mathrm{s}$. The choice of N_dir, and so of $\Delta\theta_\mathrm{s}$, mainly depends on the beamwidth $\Delta\Theta$ of the array response (here referred to $-10\,\mathrm{dB}$ gain with respect to the beam direction) reported in Table 3.1. As expected, when the number of antennas decreases, $\Delta\Theta$ becomes larger, and a lower N_dir is necessary to avoid blind zones. Once N_dir is chosen, the number of necessary 5G NR frames, and consequently, the total time needed to complete a scan cycle, are calculated from (2.13). For each selected direction, the periodogram is obtained from K active subcarriers, which differ between 5G numerologies, and a fixed number of OFDM symbols $M_\mathrm{s} = 112$, with $F_\mathrm{p} = 10$, required to perform speed estimation. Furthermore, for what concerns the DoA estimation algorithm, the MUSIC pseudo-spectrum (2.19) is computed only in the range $[\theta_\mathrm{R,s} - \Delta\Theta/2, \theta_\mathrm{R,s} + \Delta\Theta/2]$, to reduce the processing time and the position error.

The performance analysis is performed considering two different scenarios, single target and multi target. For the former, the primary purpose of the analysis is to derive the RMSE related to the estimation of the position and velocity of the target. When deriving the RMSE as a function of the SNR, the target is considered aligned with the sensing beam (i.e., $\gamma = 1$) and the noise variance is $\sigma_\mathrm{N}^2 = 1/\mathrm{SNR}$, as mentioned in Section 2.1.4. Whereas when the RMSE is evaluated varying the distance of the target, the SNR is computed using (2.15) and the following system parameters are considered: the target has an RCS equal to $\sigma_\mathrm{RCS} = 1\,\mathrm{m}^2$, the EIRP is set to $P_\mathrm{T}G_\mathrm{T}^\mathrm{a} = 43\,\mathrm{dBm}$, $G_\mathrm{R} = 1$, and the noise PSD is $N_0 = k_\mathrm{B}T_0F$ where $k_\mathrm{B} = 1.38 \cdot 10^{-23}\,\mathrm{JK}^{-1}$ is the Boltzmann constant, $T_0 = 290\,\mathrm{K}$ is the reference temperature, and $F = 10\,\mathrm{dB}$ is the receiver noise figure.

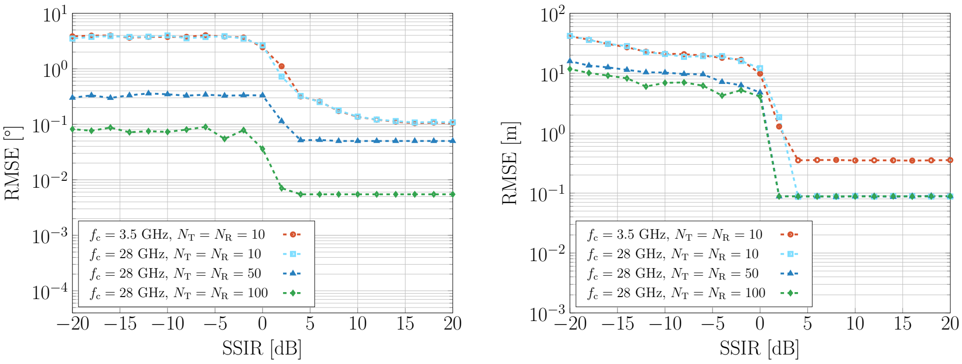

(a) *Angle estimation RMSE* (b) *Distance estimation RMSE*

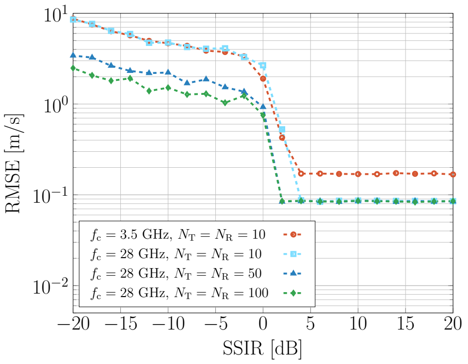

(c) *Speed estimation RMSE*

Figure 3.1: Sensing performance as a function of the SSIR for DoA, distance, and speed estimates, when SNR $= -20$ dB.

The RMSE is defined as

$$\mathrm{RMSE}(\hat{z}) = \sqrt{\frac{\sum_{i=0}^{N_{\mathrm{MC}}-1}(\hat{z}_i - z)^2}{N_{\mathrm{MC}}}} \tag{3.4}$$

where z is the true value assumed by a generic parameter to be estimated, and $\hat{z}$ is its estimate, while N_{MC} is the number of Monte Carlo (MC) iterations for each SNR value, here set equal to 2000.

For the multi-object scenario, we consider $L = 10$ point targets, one of which is the UE, and the same system parameters as the single-target scenario. Two different values of the fraction of power devoted to sensing, $\rho = 0.1$ and $\rho = 0.3$, a carrier frequency equal to $f_c = 28$ GHz, and $N_{\mathrm{T}} = N_{\mathrm{R}} = 50$ antennas, are considered. In this set of results, the OSPA metric, presented in Section 3.1, is the performance indicator to summarize the effectiveness of the

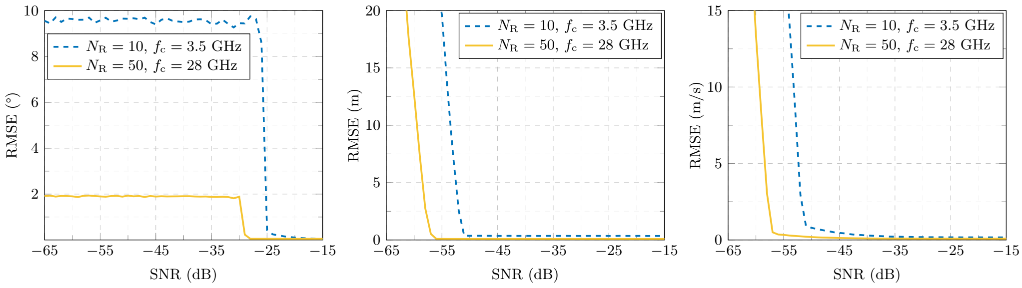

(a) *Angle estimation RMSE* (b) *Distance estimation RMSE* (c) *Speed estimation RMSE*

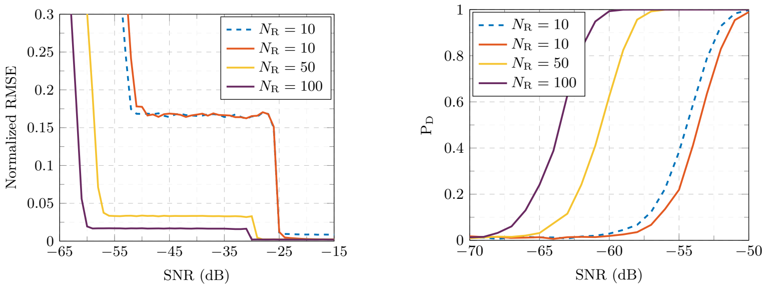

(d) *Normalized position RMSE* (e) *Detection probability*

Figure 3.2: Sensing performance as a function of the SNR for distance, DoA, speed, and position estimates, and detection probability. The dashed lines represent the results at $f_c = 3.5\,\text{GHz}$, whereas the continuous lines represent the results at $f_c = 28\,\text{GHz}$. In particular, (a), (b) and (c) show the RMSE results when the MIMO system consists of $N_T = N_R = 10$ antennas at $f_c = 3.5\,\text{GHz}$, and $N_T = N_R = 50$ antennas at $f_c = 28\,\text{GHz}$, whereas (d) and (e) depict the normalized localization error and the detection probability for different number of antennas.

designed system. The OSPA metric is computed for $q = 2$, as recommended by [72], and $\bar{c} = 10\,\text{m}$ to guarantee a good balance between localization and cardinality error. We will then provide the performance of the system in the presence of an extended target and multipath. Finally, the benefits of bayesian tracking in a vehicular scenario are demonstrated.

As it will be explained in the following, we will start investigating the impact of SI on estimation performance, focusing on the RMSE of DoA, distance, and speed estimates by varying the SSIR introduced in Section 2.1.2.

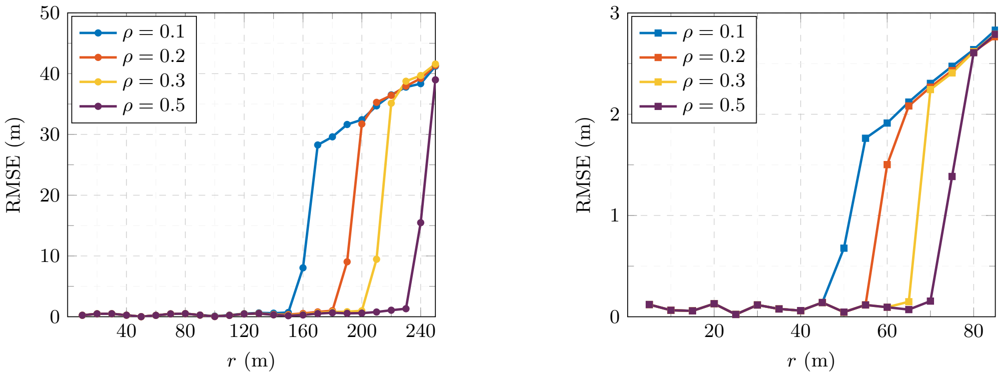

(a) *Position RMSE at* $f_c = 3.5\,\mathrm{GHz}$, $N_\mathrm{R} = 10$

(b) *Position RMSE at* $f_c = 28\,\mathrm{GHz}$, $N_\mathrm{R} = 50$

Figure 3.3: Target localization performance as a function of the sensor-target distance varying the fraction of power ρ reserved for sensing. Note that the maximum range of 250 m at 3.5 GHz and 85 m at 28 GHz is within the maximum unambiguous range for the respective numerology detailed in Table 3.1 [9].

3.2.1 RMSE and detection probability vs SNR and SSIR

Let us start analyzing the SI issue. Fig. 3.1 shows the RMSE of DoA, range, and radial velocity estimates obtained when only a single target is present and SNR $= -20\,\mathrm{dB}$, by varying the SSIR for different 5G NR parameters and number of antennas. As it can be noticed, the system performance quickly degrades for low SSIR values, but when SSIR $\geq 10\,\mathrm{dB}$, the RMSE of DoA, range, and radial velocity estimates, reaches a floor where thermal noise is the only limiting factor. Therefore, if proper SI suppression can be performed, either through beamforming optimization or through digital cancellation techniques [12, 29], the estimation error can be kept low.

From now on, an analysis of the RMSE by varying the SNR is now performed considering SI negligible. In particular, the SNR is varied from -65 to $-15\,\mathrm{dB}$, while distance, speed, and DoA of the target are varied randomly, from one iteration to another, with a uniform distribution from 20 to 85 m, -20 to $20\,\mathrm{m/s}$, and $-60°$ to $60°$, respectively. In Fig. 3.2, the results obtained for the RMSE of distance, angle, speed, and position estimations are shown. As the periodogram used to estimate speed and radial distance of the target is computed on the symbols obtained after spatial combining, the whole estimation process is subject to a double processing gain, one resulting from the periodogram calculation, equal to $10\log_{10}(K \cdot M_\mathrm{s})$ dB [15], and the other from the beamforming gain, equal to $10\log_{10}(N_\mathrm{R})$ dB. For this reason, the MIMO system can estimate range and speed with high accuracy for SNR significantly lower than those reached by the DoA estimation algorithm, as it can be seen in Fig. 3.2a, Fig. 3.2b, and Fig. 3.2c. In fact, MUSIC is not subject to any processing gain, and the RMSE of angle estimation starts to increase at much higher SNR values, depending on the number of receiving antennas, N_R. In particular, for increasingly negative values of SNR, the RMSE (in degree) vs SNR curves converge approximately to $\Delta\Theta/2.8$, because of the limited search interval, $\Delta\Theta$, over which the pseudo-spectrum is computed. As previously stated, $\Delta\Theta$, and consequently the upper bound value of the curves, strictly depends on the number of antennas, as it can be noticed comparing the blue dashed line and continuous yellow line curves in Fig. 3.2a, Fig. 3.2b and Fig. 3.2c.

From the estimated range, $\widehat{r}$, and DoA, $\widehat{\theta}$, the position estimate of the target is $\widehat{\mathbf{p}} = (\widehat{x}, \widehat{y}) = (\widehat{r}\cos\widehat{\theta}, \widehat{r}\sin\widehat{\theta})$. The normalized RMSE, shown in Fig. 3.2d, is derived from the Euclidean distance between the estimated position, $\widehat{\mathbf{p}}$, and the true location of the target, $\mathbf{p} = (x, y) = (r\cos\theta, r\sin\theta)$, divided by the true distance, r, as

$$\text{Normalized RMSE} = \sqrt{\frac{1}{N_\mathrm{MC}} \sum_{j=1}^{N_\mathrm{i}} \frac{\left\|\widehat{\mathbf{p}}_j - \mathbf{p}_j\right\|_2^2}{r_j^2}}. \tag{3.5}$$

The normalization in (3.5) eliminates the dependency of the position RMSE on the distance generalizing the results. In fact, since the length of the chord of a circumference is directly proportional to its radius, the DoA error causes the position error to increase with distance. In Fig. 3.2d the position estimate dependency on the DoA is emphasized for different numbers of antennas and 5G numerologies. As the SNR decreases, it is possible to notice the impact of DoA, which causes a first drop in the performance, and the effect of range estimation error, which leads to a second performance drop at lower SNR.

Another important parameter in sensing is the detection probability P_D as a function of the SNR as shown in Fig. 3.2e. In these plots, the threshold

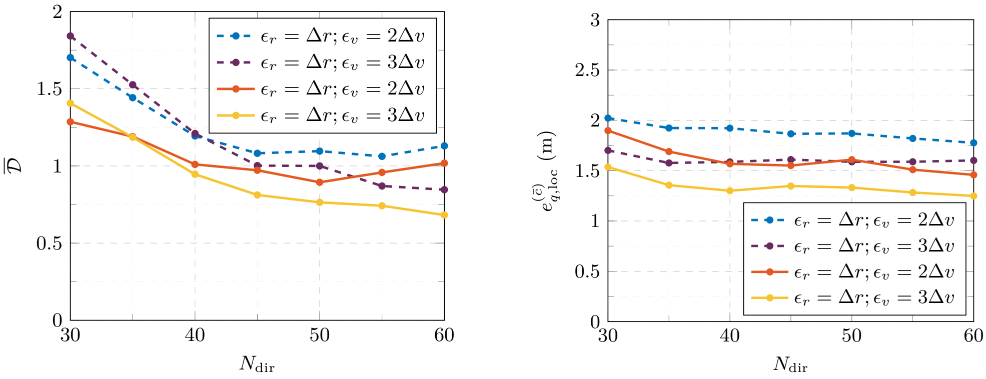

(a) (b)

Figure 3.4: Mean cardinality error (a) and mean OSPA localization error (b) varying the number of sensing directions, N_{dir}, for a JSC system with $f_{\mathrm{c}} = 28\mathrm{GHz}$, $N_{\mathrm{T}} = N_{\mathrm{R}} = 50$, obtained with $N_{\mathrm{MC}} = 500$ Monte Carlo iterations. Dashed lines represent the result for $\rho = 0.1$, whereas the continuous lines represent the results for $\rho = 0.3$.

η has been chosen to ensure a $P_{\mathrm{FA}} = 1\%$. As expected, since detection is performed on the range-Doppler map, the same map used for velocity and range estimation, it is easy to notice that the range and velocity estimation start degrading when detection probability degrades. Therefore, the main factor limiting the radar performance is DoA estimation.

3.2.2 RMSE vs distance

Let us now analyze the trade-off between communication and sensing varying ρ in (2.2). As it can be observed in Fig. 3.3a and 3.3b, the system works well also for moderately low values of ρ, e.g., $\rho = 0.1$. Notably, the position RMSE is below 0.33 m and 0.1 m, at 3.5 GHz and 28 GHz, respectively, even at tens of meters (in LoS condition). It is also important to highlight that the RMSE values reached at 3.5 GHz are much higher than that at 28 GHz. This mainly depends on the larger $\Delta\Theta$ resulting from $N_{\mathrm{T}} = N_{\mathrm{R}} = 10$, with respect to the beamwidth with $N_{\mathrm{T}} = N_{\mathrm{R}} = 50$ antennas. Moreover, at the considered ranges, the RMSE of the position mainly depends on DoA estimation error, and when this error reaches the upper bound, the position RMSE becomes proportional to the distance, r, as previously explained in Section 3.2.1.

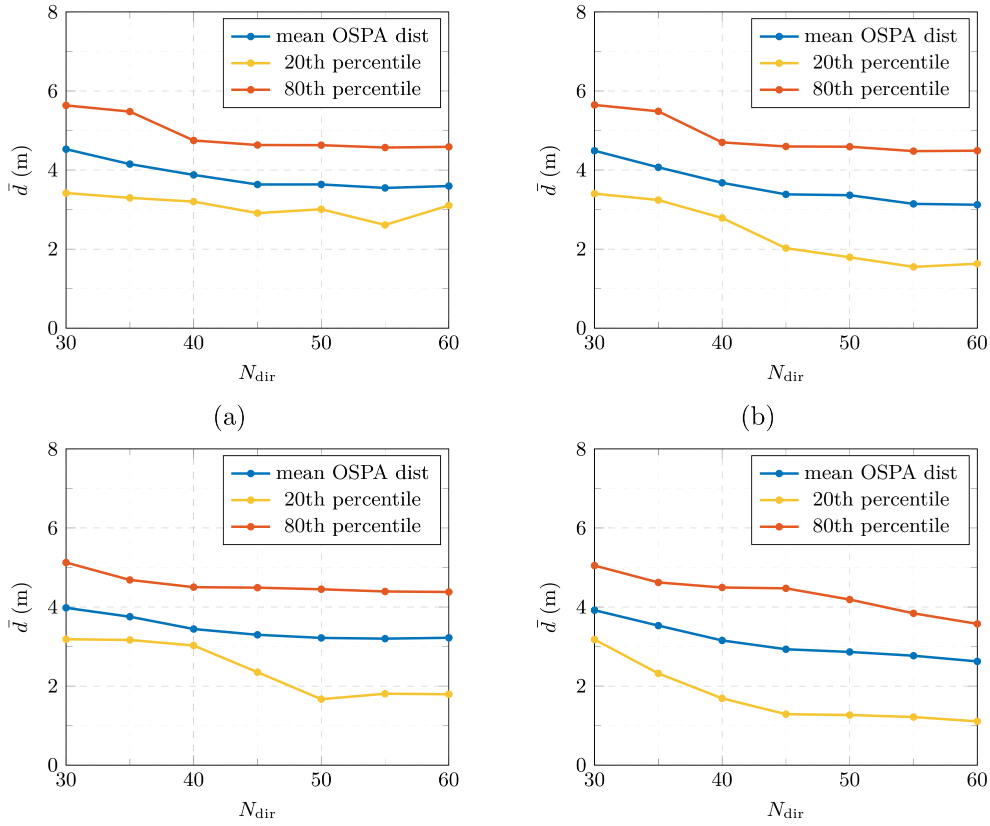

(a) (b) (c) (d)

Figure 3.5: Mean value, 20th and 80th percentile of the OSPA distance varying the number of sensing directions for different values of ϵ_r, ϵ_v and ρ, with $f_c = 28\,\mathrm{GHz}$ and $N_\mathrm{T} = N_\mathrm{R} = 50$. The OSPA metric is computed for $\bar{c} = 10\,\mathrm{m}$ and $q = 2$. The considered values are: $\epsilon_r = \Delta r$ and $\epsilon_v = 2\Delta v$ with $\rho = 0.1$ (a) and $\rho = 0.3$ (c), $\epsilon_r = \Delta r$ and $\epsilon_v = 3\Delta v$ with $\rho = 0.1$ (b) and $\rho = 0.3$ (d).

3.2.3 Performance analysis of multi-target scenario

For the multi-object scenario analysis let us consider $L = 10$ point targets ($9 + 1$ UE). Each target is associated with an SNR that depends on its radial distance from the monostatic sensor, on its RCS, and on the alignment between the target and the sensing direction, in accordance with (2.15). Without loss of generality let us assume all the targets with the same RCS, equal to $\sigma_{\mathrm{RCS}} = 1\,\mathrm{m}^2$, as in Section 3.2.2. The number of MC iterations for this group of results is set to $N_{\mathrm{MC}} = 500$. In each MC iteration targets positions are randomly generated according to a uniform distribution within a sector with radial distance between 20 to 85 m and angle from −60° to 60°.

The primary purpose of this analysis is to study the performance of the considered JSC system when multiple targets are present, computing the OSPA metric introduced in Section 3.1 for different choices of N_{dir}, ranging from 30 to 60 sensing directions. In particular, one of the main objectives is to study the influence of the uncertainty parameters, ϵ_r and ϵ_v, used in the repeated targets pruning algorithm presented in Section 2.2.3, and of the parameters ρ, on the detection and localization capabilities of the system.

For what concerns ϵ_r and ϵ_v, a good choice consists of using a multiple of distance and velocity resolutions, Δr and Δv, defined in (2.27). In fact, due to the presence of AWGN, radial distance and velocity estimates of a repeated target may fall in adjacent bins of the periodogram with respect to those of the original target. In this sense, between range and velocity, it is the latter that presents greater RMSE in the low SNR regime; this is due to zero padding, which increases velocity resolution at the expense of sensitivity to noise. The mean cardinality error is used to choose these parameters. This metric is given by

$$\overline{\mathcal{D}} = \frac{1}{N_{\text{MC}}} \sum_{i=1}^{N_{\text{MC}}} |L - \widehat{L}|. \tag{3.6}$$

Importantly, this metric does not distinguish between miss-detection, false alarm, and repeated target; however, it can be considered a good indicator for analyzing the average performance of the considered algorithm. In fact, fixing the system parameters, miss-detection and false alarm rates can be regarded as approximately constant, so if $\overline{\mathcal{D}}$ decreases, that should be caused by a drop in the targets' repetition rate. Fig. 3.4 shows the mean cardinality error and the mean OSPA localization error computed varying the number of sensing directions, N_{dir}, for different values of ϵ_r, ϵ_v and ρ. As it can clearly be noticed, by fixing ϵ_r and ϵ_v, the overall performance of the system (both in localization and cardinality error) improves for increasing values of ρ. For what concerns the localization error, the results shown in Fig. 3.4b are in agreement with those presented in Fig. 3.3b. As the position of the target is varied between 20 and 85 m, the system performance is worse for $\rho = 0.1$ than $\rho = 0.3$, as expected. In Fig. 3.4a it is possible to notice as for $N_{\text{dir}} \geq 40$ the mean cardinality error becomes smaller choosing $\epsilon_v = 3\Delta v$, both for $\rho = 0.3$

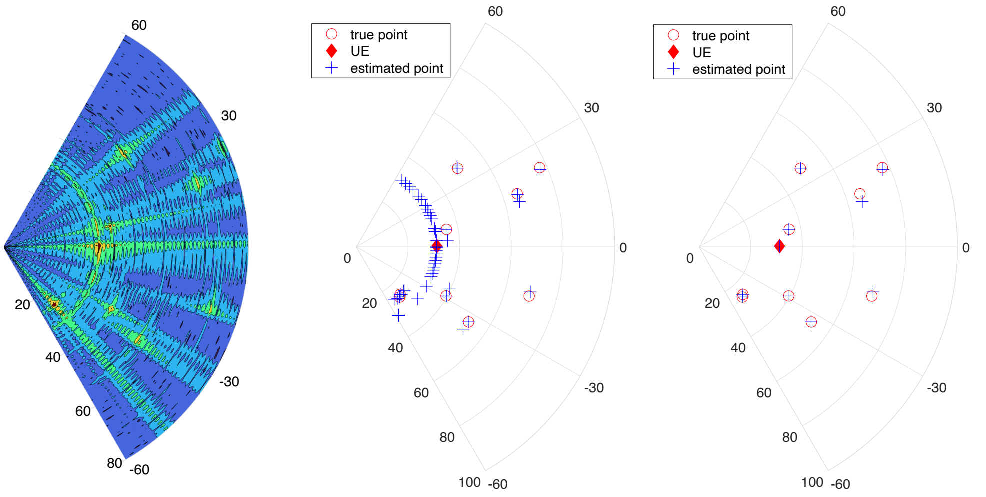

(a) (b) (c)

Figure 3.6: Considered scenario with 9 targets and 1 UE. The range-angle map in (a) has been obtained with $f_\mathrm{c} = 28\,\mathrm{GHz}$, $N_\mathrm{T} = N_\mathrm{R} = 50$ antennas, $N_\mathrm{dir} = 60$ and $\rho = 0.3$. (b) shows the point detected starting from the range-angle map in (a), before repeated targets pruning. In (c) the result obtained after the removal of the repeated targets, performed with $\epsilon_r = \Delta r$ and $\epsilon_v = 3\Delta v$ is shown.

and $\rho = 0.1$, and, in particular, for $\rho = 0.3$ the system on average misses less than one target. As pointed out, a value of $\epsilon_r > \Delta r$ does not change appreciably the system performance; therefore, its value is kept fixed, letting ϵ_v vary. This latter term most affects the repeated targets pruning algorithm detection performance due to zero padding, as already observed.

In Fig. 3.5, the mean OSPA metric is computed varying N_dir for the same values of ϵ_r, ϵ_v and ρ used above. In addition, the 20th and 80th percentile are shown to better understand the range of values the OSPA metric can assume for different positions of the targets. Also in this case, the best performance are obtained for $\rho = 0.3$, $\epsilon_r = \Delta r$ and $\epsilon_v = 3\Delta v$. In particular, for this choice of parameters the mean value of $\bar{d}$ is below $3\,\mathrm{m}$ and the 20th percentile is approximately equal to $1\,\mathrm{m}$ for $N_\mathrm{dir} = 60$. Note, however, that such numerical results also consider the portion of the monitored area where the DoA estimation is severely degraded (see Fig. 3.3); a proper sensing cell sizing may avoid such region and lead to much better performance. As a final system-level analysis, in Fig. 3.6 an example of multiple targets map returned by the JSC sensor is shown. The parameters are $\rho = 0.3$, $\epsilon_r = \Delta r$

and $\epsilon_v = 3\Delta v$. First, in Fig. 3.6a the range-angle map obtained by computing the periodogram (2.23) in each sensing direction, is shown. Then, in Fig. 3.6b we have the targets detected through the hypothesis test (2.24), and the resulting range estimates (2.25)-(2.26) and angle estimates (2.20). As it can be seen, multiple points per target are present. After the repeated targets pruning algorithm introduced in Section 2.2.3 the resulting targets are shown in Fig. 3.6c. As we can observe, in this particular case the algorithm is very effective in removing all redundant points while retaining all the useful points. As expected, most of the repeated points are on the circumference with a radius equal to the distance between the UE and the monostatic sensor; this is to be attributed to a large fraction of power used for the communication beam which illuminates the UE causing a strong received echo.

3.3 Remarks

In this chapter, we provided a system-level analysis for the multibeam JSC system introduced in Chapter 2. We identified the main dominant factors affecting performance and compared two system setups operating at sub-6 GHz, and mmWave frequencies. The findings of the analysis conducted have demonstrated that: *i*) DoA estimation is the primary source of error when used to evaluate the target position; *ii*) even with a relatively small fraction of power devoted to sensing, good localization performance at tens of meters can be achieved in LoS even at mmWave: *iii*) in the sub-6 GHz band targets can be detected at higher distances but with lower accuracy mainly because of the reduced number of antenna elements; *iv*) Tens of targets can be detected and localized with sub-meter level accuracy when the power for sensing is capable of ensuring reliable DoA estimation.

Chapter 4

From Monostatic to Bistatic Configuration

In this chapter, we extend the performance analysis conducted in Chapter 3, which considered a single point-like target scenario and monostatic configuration, to include a bistatic JSC system. As already mentioned in Chapter 1, a bistatic radar setup can be seen as a concrete solution to avoid the SI problem that arises in a monostatic setting and requires full-duplex capabilities, which are still considered a challenge. As in the previous chapter, we first provide the sensing performance of a bistatic JSC MIMO system consisting of a Tx and a Rx that estimates DoA and bistatic range, comparing two setups operating at sub-6 GHz and mmWave frequencies. We then analyze the RMSE of position estimate in the monitored area through heatmaps and show the impact of the blind zone on sensing. Lastly, since a multibeam system is considered as in Chapter 2, the sensing coverage limits of the bistatic system are studied, by varying the fraction of power devoted to sensing.

4.1 System Model

As depicted in Fig. 4.1, in this chapter, a bistatic configuration for the JSC system is considered. In contrast with the monostatic setup studied in the previous chapters, in which the Tx and the Rx are co-located, the bistatic one employs two nodes at different known locations, $\mathbf{p}_{\text{tx}} = (x_{\text{T}}, y_{\text{T}})$, and

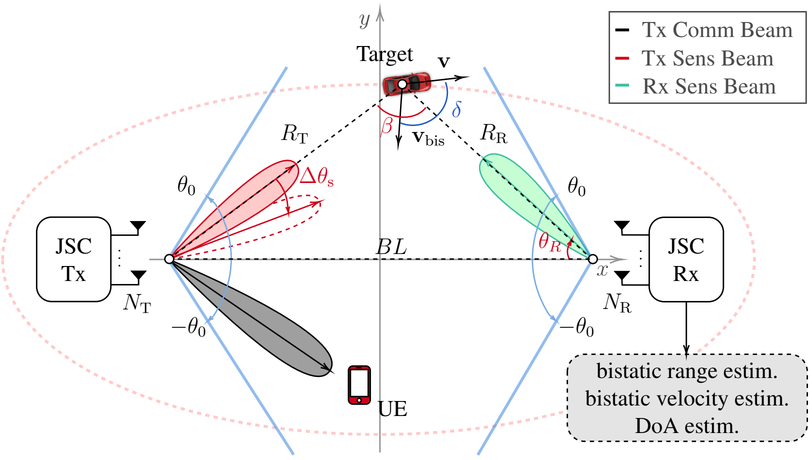

Figure 4.1: Illustration of the considered bistatic system for JSC. The Tx presents multibeam capabilities to perform communication and sensing functionalities using the same time-frequency resources and sharing the transmitted power.

$\mathbf{p}_{\rm rx} = (x_{\rm R}, y_{\rm R})$. In this way, it is possible to avoid the well-known self-interference problem affecting monostatic configurations [12].

Considering a bistatic sensing system based on downlink signals, the Tx can be a BS. Still, the Rx can be either another BS, a UE-like device, or a remote radio head (RRH) in a Cloud-RAN architecture. Alternatively, the system can work with uplink signals as well. In this case, the signal transmitted by a UE is collected by a BS, after being reflected from targets [3, 7].

The proposed JSC system consists of a Tx with $N_{\rm T}$ antenna elements and of an Rx with $N_{\rm R}$ antenna elements. Similarly to the system model considered in Chapter 2, the transmitted signal is used for both communication and sensing, exploiting the multibeam capabilities of the system, with a sensing beam that scans the environment while the communication beam points towards the user. Without loss of generality, both the Tx and the Rx are equipped with ULAs whose elements are equally spaced of half-wavelength, i.e., $d = \lambda_{\rm c}/2$ with $\lambda_{\rm c} = c/f_{\rm c}$, where $f_{\rm c}$ is the carrier frequency and c is the speed of light. The communication system transmits a 5G NR downlink signal with M OFDM symbols and K active subcarriers to a UE in the cell [62]. The baseband OFDM signal, as for the monostatic case in Section 2.1, can be written as (2.1).

4.1.1 Bistatic range and Doppler shift

In a bistatic configuration, the propagation time τ of the signal scattered by the target is related to the distance between the Tx and the target, R_{T}, and that between the target and the Rx, R_{R}, via the bistatic range [13]

$$R_{\mathrm{bis}} = R_{\mathrm{T}} + R_{\mathrm{R}} = \tau \cdot c. \tag{4.1}$$

After estimating R_{bis} via τ, the target can be located on an ellipse with a major axis equal to R_{bis} and foci at Tx and Rx positions, as depicted in Fig. 4.1. The Tx, Rx, and target form a triangle with base BL (the distance between Tx and Rx) called the baseline; the angle β of the opposite vertex is named the bistatic angle.

If the DoA θ_{R} of the reflected echo at the Rx can be estimated, it is possible to determine the distance R_{R} as [13]

$$R_{\mathrm{R}} = \frac{R_{\mathrm{bis}}^2 - BL^2}{2(R_{\mathrm{bis}} + BL \sin(\theta_{\mathrm{R}} - \pi/2))} \tag{4.2}$$

and then the target position, $\mathbf{p}_{\mathrm{tg}} = (x_{\mathrm{R}} - R_{\mathrm{R}} \cos\theta_{\mathrm{R}}, y_{\mathrm{R}} + R_{\mathrm{R}} \sin\theta_{\mathrm{R}})$.

In addition to the target's location, the bistatic velocity of the target can be inferred from the bistatic Doppler shift. The latter is proportional to the rate of change of R_{bis}. When Tx and Rx are stationary, and the target is moving with velocity $\mathbf{v}$, the Doppler shift can be obtained as [13]

$$f_{\mathrm{D}} = \frac{1}{\lambda_{\mathrm{c}}} \frac{d}{dt} \left[R_{\mathrm{T}}(t) + R_{\mathrm{R}}(t)\right] = \frac{2v}{\lambda_{\mathrm{c}}} \cos\delta \cos(\beta/2) \tag{4.3}$$

where δ is the angle between the direction of the velocity and the bistatic bisector, and $v = |\mathbf{v}|$. While β can be easily determined by knowing BL, R_{T}, R_{R}, and θ_{R}, the angle δ is unknown so only the bistatic velocity, $v_{\mathrm{bis}} = |\mathbf{v}_{\mathrm{bis}}| = v \cos\delta$, can be estimated by the system.

4.1.2 Maximum bistatic range and blind zone

To avoid inter-symbol interference (ISI) and guarantee unambiguous range detection, the guard time t_{G} of the OFDM needs to be larger than the prop-

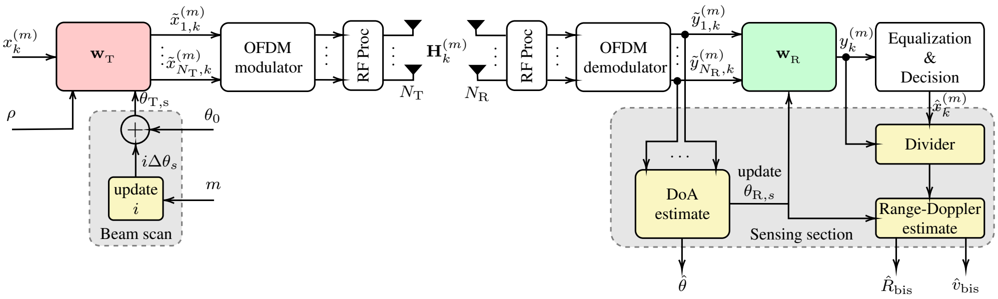

Figure 4.2: Block diagram of the bistatic 5G NR-based JSC system with multibeam capability.

agation delay of the scattered signal. In a bistatic configuration, this leads to a maximum detectable bistatic range

$$R_\mathrm{bis} \leq t_\mathrm{G} c + BL \tag{4.4}$$

which results in a maximum ellipse whose minor axis is

$$A_\mathrm{max} = \sqrt{(t_\mathrm{G} c + BL)^2 - BL^2}. \tag{4.5}$$

A critical issue deserving attention in bistatic setup is the blind zone, i.e., a region enclosing the baseline where target detection becomes problematic [74]. A target sufficiently close to the baseline is hard to detect because of the time resolution, which compromises the separation of the direct Tx-Rx path from the Tx-target-Rx one. Given the resolution of the bistatic range estimate, $\Delta r = c/(K\Delta f)$, we define $BL + \Delta r$ as the minimum bistatic range below which the Rx cannot resolve the reflected path from the direct one. So, we must have

$$R_\mathrm{bis} \geq BL + \Delta r. \tag{4.6}$$

The ellipse with major axis $BL + \Delta r$ is called the minimum ellipse, whose minor axis is $A_\mathrm{min} = \sqrt{(BL + \Delta r)^2 - BL^2}$.

4.1.3 Transmitted and received signal

Now, let us detail the whole system behavior by looking at the block diagram in Fig. 4.2. First, at the Tx, QPSK symbols $x_k^{(m)}$ are mapped at each antenna through a digital precoder $\mathbf{w}_{\mathrm{T}} \in \mathbb{C}^{N_{\mathrm{T}} \times 1}$, to obtain the transmitted vector $\tilde{\mathbf{x}}_k^{(m)} \in \mathbb{C}^{N_{\mathrm{T}} \times 1}$, defined as $\tilde{\mathbf{x}}_k^{(m)} = \mathbf{w}_{\mathrm{T}} x_k^{(m)}$. In particular, the idea is to split the available transmitted power of the OFDM signal between communication and sensing, using the BF vector in (2.2).

As it is shown in Fig. 4.2, in the considered JSC system, the sensing direction $\theta_{\mathrm{T,s}}$ is sequentially changed to illuminate the entire surrounding environment, according to

$$\theta_{\mathrm{T,s}} = \theta_0 + i\,\Delta\theta_{\mathrm{s}} \qquad i = 0, \dots, N_{\mathrm{dir}} - 1 \tag{4.7}$$

where $\Delta\theta_{\mathrm{s}}$ is the angle step and N_{dir} is the number of directions to scan the aperture $[-\theta_0, \theta_0]$. Given M OFDM symbols contained in a 5G NR frame, $M_{\mathrm{s}} < M$ symbols are acquired by the Rx in each sensing direction. Hence, the update of i depends on the symbol index m, and the number of frames and time required to complete a scan become $N_{\mathrm{f}} = \left\lceil \frac{M_{\mathrm{s}} N_{\mathrm{dir}}}{M} \right\rceil$ and $T_{\mathrm{scan}} = T_{\mathrm{f}} N_{\mathrm{f}}$.

For each $\theta_{\mathrm{T,s}}$, the vector $\tilde{\mathbf{y}}_k^{(m)} \in \mathbb{C}^{N_{\mathrm{R}} \times 1}$ of the received symbols at each antenna after OFDM demodulation, is given by

$$\tilde{\mathbf{y}}_k^{(m)} = \mathbf{H}_k^{(m)} \tilde{\mathbf{x}}_k^{(m)} + \tilde{\mathbf{n}}_k \tag{4.8}$$

where $\mathbf{H}_k^{(m)} \in \mathbb{C}^{N_{\mathrm{R}} \times N_{\mathrm{T}}}$ is the channel matrix, and $\tilde{\mathbf{n}}_k \sim \mathcal{CN}(\mathbf{0}, \sigma_{\mathrm{N}}^2 \mathbf{I}_{N_{\mathrm{R}}})$. When L point targets are present in the monitored area, the channel matrix between the transmitting and receiving antennas can be represented as

$$\mathbf{H}_k^{(m)} = \sum_{l=1}^{L} \underbrace{\alpha_l e^{j2\pi m T_{\mathrm{s}} f_{\mathrm{D},l}} e^{-j2\pi k \Delta f \tau_l}}_{\triangleq \beta_l} \mathbf{a}_{\mathrm{R}}(\theta_{\mathrm{r},l}) \mathbf{a}_{\mathrm{T}}^T(\theta_{\mathrm{t},l}) \tag{4.9}$$

where $\boldsymbol{\theta}_{\mathrm{R}} = [\theta_{\mathrm{r},1}, \theta_{\mathrm{r},2}, \dots, \theta_{\mathrm{r},L}]$ are the DoAs, $\boldsymbol{\theta}_{\mathrm{T}} = [\theta_{\mathrm{t},1}, \theta_{\mathrm{t},2}, \dots, \theta_{\mathrm{t},L}]$ are the DoDs of the targets, and $\alpha_l = |\alpha_l|\, e^{j\phi_l}$ is the complex amplitude which includes phase shift and attenuation along the lth propagation path.

On the receiving side shown in Fig. 4.2, starting from (4.8), spatial combining is performed through the receiving BF vector $\mathbf{w}_{\mathrm{R}}$ to obtain the received symbol, $y_k^{(m)} = \mathbf{w}_{\mathrm{R}}^T \tilde{\mathbf{y}}_k^{(m)}$. In particular, target detection and localization are performed in two steps: 1) the vector $\mathbf{w}_{\mathrm{R}}$ is initialized to have all elements equal to one to search for targets in the area through DoA estimation, $\widehat{\theta}_{\mathrm{r},l}$; 2) once DoAs are estimated, $\mathbf{w}_\mathrm{R}$ is updated to point the receiving beam in the direction where the target l is likely to be present, i.e., $\mathbf{w}_\mathrm{R} = \mathbf{a}_\mathrm{R}^c(\theta_{\mathrm{R},s})$, with $\theta_{\mathrm{R},s} = \widehat{\theta}_{\mathrm{r},l}$. Then, in each sensing direction, the Rx needs to perform channel equalization and decision for detecting the transmitted symbols, $\hat{x}_k^{(m)}$. As will be explained in Section 4.2.2, to estimate bistatic range and Doppler shift, it is necessary to know and remove the transmitted symbol $x_k^{(m)}$, through the *divider* block.

4.1.4 Received power and Cassini ovals

In the bistatic radar configuration, the power reflected by a point target l with a RCS equal to $\sigma_{\mathrm{RCS},l}$, illuminated by the Tx sensing beam and collected at the Rx antenna element in free-space propagation conditions, is given by

$$P_{\mathrm{R},l}^{\mathrm{bis}} = \frac{\rho P_\mathrm{T} G_\mathrm{T} G_\mathrm{R} c^2 \sigma_{\mathrm{RCS},l}}{(4\pi)^3 f_\mathrm{c}^2 (R_{\mathrm{T},l} R_{\mathrm{R},l})^2} \tag{4.10}$$

where G_R is the receiving antenna gain of the single antenna element, while $R_{\mathrm{T},l}$ and $R_{\mathrm{R},l}$ are, respectively, the Tx-target and Rx-target distances for the lth target.

As it can be seen in (4.10), the received power scattered by the target is inversely proportional to $(R_\mathrm{T} R_\mathrm{R})^2$. The locus of points such that the product of their distances $R_\mathrm{T} R_\mathrm{R}$ from two foci is a constant is named Cassini oval [13, 74].

Starting from (4.10), the SNR at the single receiving antenna element related to the lth target can be defined as

$$\mathrm{SNR}_l = \frac{P_{\mathrm{R},l}^{\mathrm{bis}}}{N_0 K \Delta f} \tag{4.11}$$

where N_0 is the one-sided noise PSD at each antenna element. By normalizing to one the mean power of the transmitted symbols, i.e., $\mathbb{E}\{|x_k^{(m)}|^2\} = 1$, (4.11) reduces to $\mathrm{SNR}_l = 1/\sigma_\mathrm{N}^2$. Iso-SNR contours are thus Cassini ovals.

4.2 Estimation of Target Parameters and Detection

This section introduces the techniques used for estimating DoA, bistatic range, and bistatic velocity. In particular, for the DoA three different methods have been compared, i.e., MUSIC, root-MUSIC, and estimation of signal parameters via rotational invariance techniques (ESPRIT), while for bistatic range and velocity estimation, a periodogram-based frequency estimation approach has been used, as in Section 2.2.

4.2.1 Estimation of the number of targets and DoAs

DoAs estimation requires, at first, the evaluation of the number of targets or sources. For the initial estimate, the sample covariance matrix of the received symbols vector (4.8) is computed in each Tx sensing direction, as follows

$$\widehat{\mathbf{R}} = \frac{1}{KM_\mathrm{a}} \sum_{m=0}^{M_\mathrm{a}-1} \sum_{k=0}^{K-1} \tilde{\mathbf{y}}_k^{(m)} \tilde{\mathbf{y}}_k^{(m)\dagger} = \mathbf{U} \boldsymbol{\Lambda} \mathbf{U}^\dagger \tag{4.12}$$

where $M_\mathrm{a} \subset M_\mathrm{s}$ is the number of OFDM symbols employed in each sensing direction to estimate the DoAs, the columns of $\mathbf{U} \in \mathbb{C}^{N_\mathrm{R} \times N_\mathrm{R}}$ are the eigenvectors of $\widehat{\mathbf{R}}$ and $\boldsymbol{\Lambda} = \mathrm{diag}(\lambda_1, \dots, \lambda_{N_\mathrm{R}})$ is a diagonal matrix with eigenvalues sorted in descending order.

Starting from $\boldsymbol{\Lambda}$, the number of sources $\widehat{L}$ can be estimated by model order selection based on information-theoretic criteria (see e.g., (2.18)). Then, since the noise is zero mean and independent of the target echoes, the eigenvectors corresponding to the $N_\mathrm{R} - \widehat{L}$ smallest eigenvalues of $\widehat{\mathbf{R}}$ identify the noise subspace, whereas the first $\widehat{L}$ eigenvalues determine the signal subspace. Starting from the noise subspace, the vector of DoAs, $\widehat{\boldsymbol{\theta}}_\mathrm{R}$, is estimated, either through MUSIC or root-MUSIC algorithms, or, from the signal subspace, with the ESPRIT algorithm [71, 75, 76].

4.2.2 Range-Doppler estimation and localization

After a DoA, $\widehat{\theta}_{\mathrm{r},l}$, has been chosen, the bistatic range and velocity of the target l are extrapolated through range-Doppler evaluation as in Section 2.2. Starting from the received symbols $y_k^{(m)}$, a division is performed to remove the unwanted data symbols, i.e., $g_k^{(m)} = y_k^{(m)}/x_k^{(m)}$.[1] Next, as $g_k^{(m)}$ contains two complex sinusoids for each target, embedded in β_l of (4.9), whose frequencies are related to $f_{\mathrm{D},l}$ and τ_l, a periodogram can be computed, as [12, 14]

$$\mathcal{P}(q,p) = \left| \sum_{k=0}^{K_\mathrm{p}-1} \left(\sum_{m=0}^{M_\mathrm{p}-1} g_k^{(m)} e^{-j2\pi \frac{mp}{M_\mathrm{p}}} \right) e^{j2\pi \frac{kq}{K_\mathrm{p}}} \right|^2 \tag{4.13}$$

with $q = 0, \dots, K_\mathrm{p} - 1$ and $p = 0, \dots, M_\mathrm{p} - 1$. In this work, $K_\mathrm{p} > K$ and $M_\mathrm{p} > (M_\mathrm{s} - M_\mathrm{a})$ are calculated as the next power of two of K and $F_\mathrm{p} \cdot (M_\mathrm{s} - M_\mathrm{a})$, respectively, where F_p is the zero-padding factor to improve speed estimation resolution. The periodogram (4.13) represents the range-Doppler map from which, after performing target detection by a hypothesis test as in Section 2.2, bistatic range and velocity of the target l can be extracted. In particular, at first, the location of the peak in the periodogram needs to be found, as $(\widehat{q}, \widehat{p}) = \arg\max_{(q,p)}\{\mathcal{P}(q,p)\}$. Then, the bistatic range can be evaluated as

$$\widehat{R}_{\mathrm{bis},l} = \frac{\hat{q}\, c}{\Delta f K_\mathrm{p}}. \tag{4.14}$$

Once $\widehat{R}_{\mathrm{bis},l}$ and $\widehat{\theta}_{\mathrm{r},l}$ have been estimated, it is possible to estimate the distance between the Rx and the target, $\widehat{R}_{\mathrm{R},l}$, according to (4.2). Then, position and bistatic velocity of the target l are determined as stated in Section 4.1.1. In particular, the module of the bistatic velocity is given by

$$\widehat{v}_{\mathrm{bis}} = \frac{\widehat{p} c}{2 f_\mathrm{c} T_\mathrm{s} M_\mathrm{p} \cos\left(\beta/2\right)}. \tag{4.15}$$

---

[1] Note that, in this analysis, the symbols $x_k^{(m)}$ are considered known at the Rx; this may happen, e.g., because of correct demodulation or because the sequence of symbols emitted during sensing is predefined. Moreover, perfect synchronization between Tx and Rx is assumed.

Table 4.1: JSC system parameters

5G specification →	NR 100	NR 400
f_c [GHz]	3.5	28
Δf [kHz]	30	120
Active subcarriers K	3276	3168
OFDM symbols per frame M	280	1120
Number of antennas N_T	10	50
Number of antennas N_R	10	10 50

4.3 System Level Analysis

Numerical simulations are performed to evaluate the performance of the presented bistatic JSC system. In particular, since the main purpose here is to study the system behavior in terms of RMSE of position, angle and bistatic range estimation, a single target scenario is considered, i.e., $L = 1$, with the sensing beam at Tx aligned with the target, i.e., $\theta_{\mathrm{T,s}} = \theta_{\mathrm{t},1}$. The parameter θ_0 is set to 60° to have a total angular aperture of 120° at both Tx and Rx. Table 4.1 shows the 5G NR parameters employed for the simulations. For each sensing direction at the Tx, K active subcarriers and $M_\mathrm{s} = 112$ OFDM symbols are considered. A QPSK modulation alphabet is considered for each subcarrier.

As already stated in Section 4.1.3, at the Rx, the initially performed operation is DoA estimation with the first $M_\mathrm{a} = 30$ OFDM symbols acquired. Then, the receiving BF vector, $\mathbf{w}_\mathrm{R}$, is updated accordingly and the periodogram is performed with the remaining $M_\mathrm{s} - M_\mathrm{a} = 82$ OFDM symbols, with $F_\mathrm{p} = 10$. For DoA estimation with MUSIC, the pseudo-spectrum function is computed only in the range $[-\theta_0, \theta_0]$, to reduce the processing burden.

Two types of simulations are performed: 1) RMSE of DoA and R_bis estimate as a function of the SNR. In this case, the received symbols are normalized to unit power and the noise variance is defined as $\sigma^2_\mathrm{N} = 1/\mathrm{SNR}$, as mentioned in Section 4.1.4; 2) system coverage analysis performed computing the RMSE of the position estimate, with the SNR as a function of target position itself and of the portion of transmitted power reserved to sensing, according to (4.11). In this case, the following system parameters are considered: the EIRP is set to $P_\mathrm{T}G_\mathrm{T} = 43\,\mathrm{dBm}$; $G_\mathrm{R} = 1$ and the noise PSD is $N_0 = k_\mathrm{B}T_0F$; the target RCS is $\sigma_\mathrm{RCS} = 1\,\mathrm{m}^2$.

4.3.1 RMSE vs SNR

In this set of simulations, the position of the target is varied randomly, from one realization to another, within a diamond-shaped area identified by θ_0, as illustrated in Fig. 4.1. As expected, inside the blind zone, target detection is problematic, and the error is affected primarily by the bistatic geometry configuration. For this reason, targets are not generated inside the minimum ellipse, as this zone is not considered a system operation zone. In each realization, the target velocity is varied randomly, with a uniform distribution from -20 to $20\,\mathrm{m/s}$.

Fig. 4.3 shows the RMSE as a function of the SNR for DoA and bistatic range estimate. In the former, MUSIC, root-MUSIC, and ESPRIT algorithm are compared. Since the target parameters estimate strongly depends on the beamforming direction at the Rx, i.e., $\theta_\mathrm{R,s}$, to separately study the two errors, the curve in Fig. 4.3b is obtained using the true value of the target DoA as $\theta_\mathrm{R,s}$ to update the receiving BF vector. As it can be noticed, RMSE of the DoA estimate increases for higher values of the SNR than those for which the estimate of R_bis degrades. This behavior can be explained considering that R_bis estimation process is subject to a double processing gain, one resulting from the periodogram calculation, equal to $10\log_{10}(K\cdot(M_\mathrm{s}-M_\mathrm{a}))\,\mathrm{dB}$ [9], and the other from the beamforming gain, equal to $10\log_{10}(N_\mathrm{R})\,\mathrm{dB}$. In contrast, the DoA estimation is not subject to any processing gain, and the RMSE of angle estimation starts to increase at much higher SNR values, depending on the number of receiving antennas N_R.

Moreover, root-MUSIC and ESPRIT strictly depend on the number of estimated targets, as well as the noise and signal subspace, respectively. At lower SNR, when the number of targets estimation becomes difficult, the DoA estimate process fails, and targets can be missed. This defines a lower bound, $\mathrm{SNR}_\mathrm{min}$, for angle estimation and position estimation, as a consequence. MUSIC is still able to detect targets for lower SNR as it depends solely on the noise subspace, but angle RMSE increases rapidly.

4.3.2 Coverage analysis

For the sensing coverage area analysis, the considered diamond-shaped region of space is divided into pixels of $1\,\mathrm{m}^2$ area, and the error on the position estimate in each pixel is calculated. Also in this case, the speed of the target is varied randomly with uniform distribution from -20 to $20\,\mathrm{m/s}$. A direct visualization of the behavior of the position RMSE in each point inside the considered area is represented through heatmaps, shown in Fig. 4.4, evaluated for two different values of BL with a fraction of power for sensing given by $\rho = 0.1$. In particular, a 5G NR signal with $\Delta f = 120\,\mathrm{kHz}$, $f_\mathrm{c} = 28\,\mathrm{GHz}$, and a number of antennas $N_\mathrm{T} = N_\mathrm{R} = 50$ are used. For DoA estimation root-MUSIC is applied. In the scenario of Fig. 4.4a, Tx and Rx are located at (-30,0) and (30,0), respectively, with $BL = 60\,\mathrm{m}$. In this case, $A_\mathrm{min} = 9.8\,\mathrm{m}$ and $A_\mathrm{max} = 228\,\mathrm{m}$. Likewise, in Fig. 4.4b a baseline $BL = 80\,\mathrm{m}$ is considered, with Tx and Rx located at (-40,0) and (40,0), having $A_\mathrm{min} = 11.3\,\mathrm{m}$ and $A_\mathrm{max} = 243\,\mathrm{m}$. These results highlight how the fraction of covered area increases as the baseline decreases for fixed sensing power. However, the blind zone area does not decrease proportionally to the overall area when decreasing BL, and thus, for shorter baselines, the fraction of the covered area diminishes. This behavior is better emphasized in Fig. 4.4c, where the percentage of covered areas as a function of the baseline BL, for different values of ρ, is shown.

More precisely, the percentage of coverage area is calculated as the following. Recalling Fig. 4.3a, the coverage area is calculated through the maximum Cassini oval, associated with the minimum SNR, $\mathrm{SNR}_\mathrm{min}$, for which the system can estimate the DoA with good accuracy. For example, for the parameters specified above and root-MUSIC estimation performance, $\mathrm{SNR}_\mathrm{min} = -26.1\,\mathrm{dB}$ at $f_\mathrm{c} = 28\,\mathrm{GHz}$, whereas $\mathrm{SNR}_\mathrm{min} = -22.1\,\mathrm{dB}$ at $f_\mathrm{c} = 3.5\,\mathrm{GHz}$. The blind zone region is not considered in the sensing system covered area since in that zone, target detection becomes problematic with very large position RMSE, as shown in Fig. 4.4a and Fig. 4.4b. Therefore, the coverage area is the area of the diamond-shaped region inside the Cassini oval, corresponding to $\mathrm{SNR}_{\min}$, minus the area of the blind zone; such area is then normalized to the diamond-shape area to provide a measure of coverage effectiveness of the sensing system.

4.4 Remarks

In this chapter, the analysis presented in the previous chapters related to a monostatic JSC system based on 5G NR has been extended by considering a bistatic setup. An analysis of the sensing performance when such a system is used to estimate the position of a target via bistatic range and DoA has been performed. Analyzing the RMSE, we found that good accuracy can be achieved in LoS, both at mmWave and sub-6 GHz frequencies, and that: *i*) DoA estimation is the primary source of degradation of the system localization performance; *ii*) a fraction of coverage area greater or equal to 70% can be reached for a baseline $L \leq 80\,\mathrm{m}$, even at mmWave when ρ is equal to 0.3; *iii*) the blind zone may have a major impact on detection coverage, especially for narrow bandwidth numerologies.

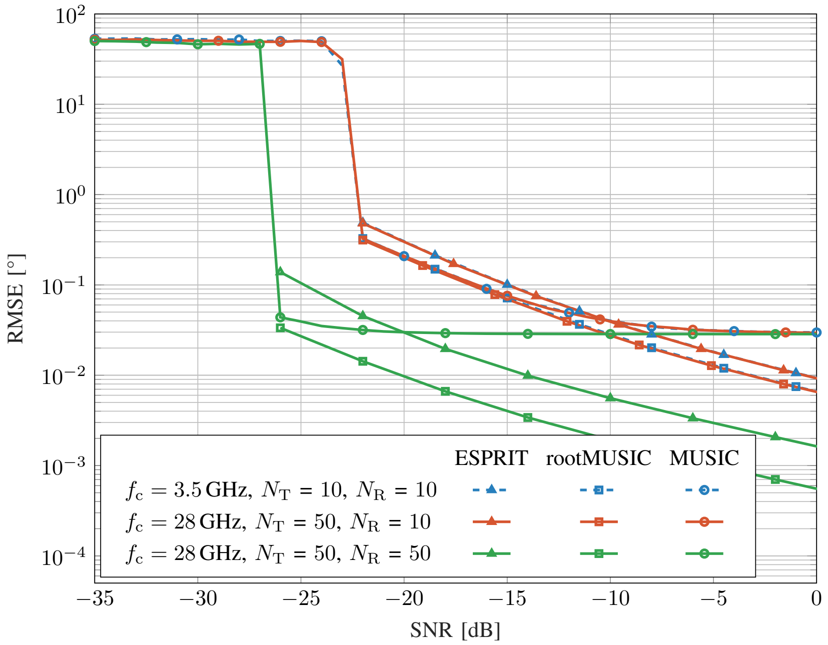

(a) *Angle estimation RMSE*

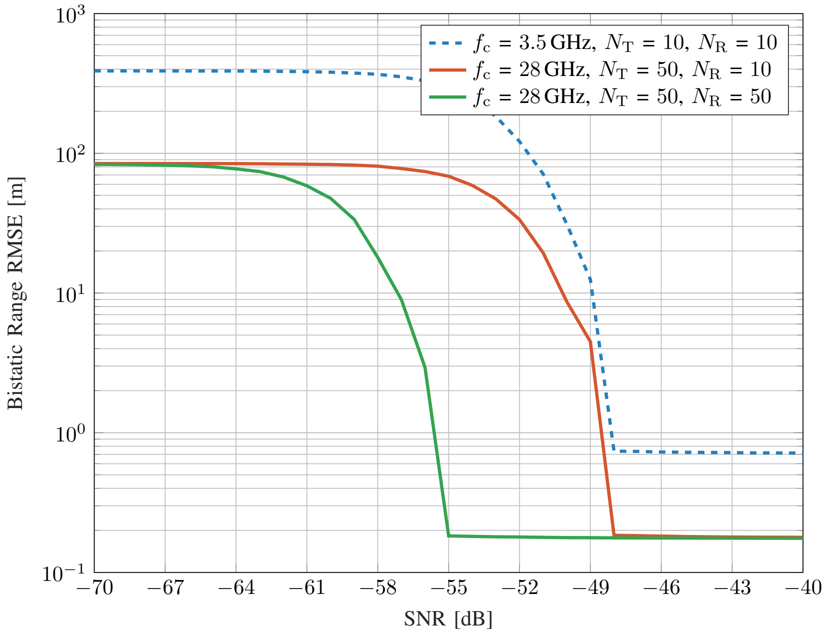

(b) *Bistatic range estimation RMSE*

Figure 4.3: Sensing performance of the JSC system as a function of the SNR for DoA and bistatic range estimates, comparing a different number of antennas and 5G numerologies. In (a) the RMSE of the DoA estimate for different estimation techniques, is shown; (b) shows the RMSE of the bistatic range estimate.

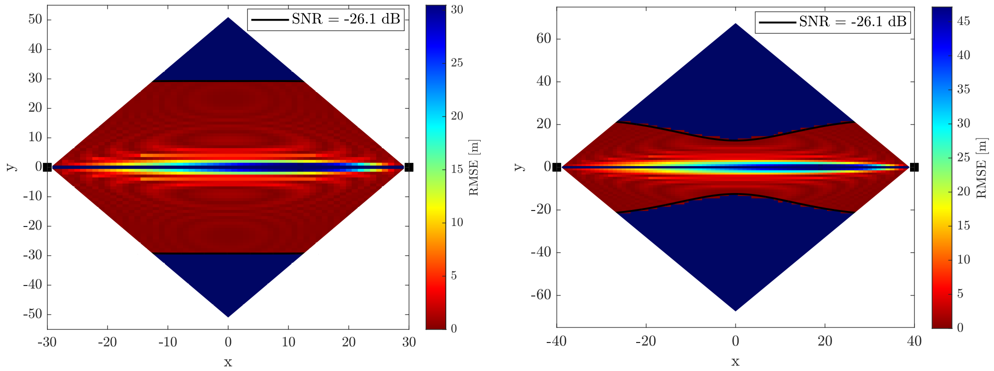

(a) *Baseline* $BL = 60$ (b) *Baseline* $BL = 80$

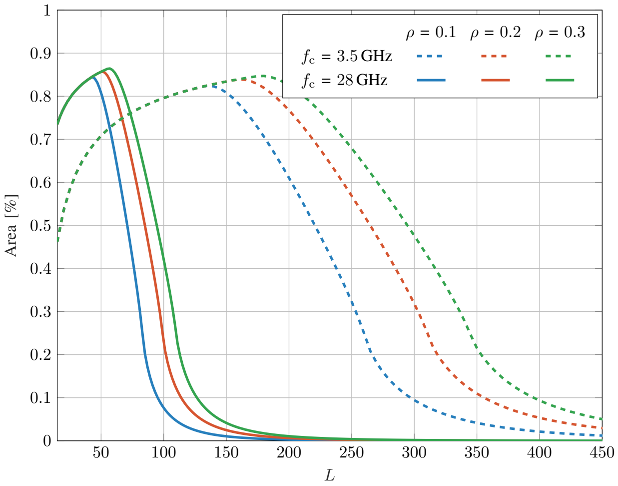

(c) *Coverage area of the sensing system*

Figure 4.4: Sensing coverage of the JSC bistatic system operating at $f_\mathrm{c} = 28\,\mathrm{GHz}$ with $N_\mathrm{T} = N_\mathrm{R} = 50$ and $f_\mathrm{c} = 3.5\,\mathrm{GHz}$ with $N_\mathrm{T} = N_\mathrm{R} = 10$. In particular, (a) and (b) show the heatmaps representing the system coverage in terms of the position RMSE when $f_\mathrm{c} = 28\,\mathrm{GHz}$ and $\rho = 0.1$, with the SNR as a function of the target position itself and of the portion of the transmit power reserved for sensing. The black lines bordering the red areas represent the Cassini Oval at SNR $= -26.1\,\mathrm{dB}$. (c) shows the fraction of area covered for different values of the power reserved for sensing, varying the baseline L.

Chapter 5

Multistatic Joint Sensing and Communication System in the Near/Far-Field

This chapter aims at extending the analysis presented in Chapter 3 and Chapter 4, in which we considered monostatic and bistatic settings, respectively, and point-like targets, by studying the performance of a MIMO OFDM-based JSC multistatic system in the presence of ETs, which here represent UEs (e.g., cars, motorcycles, etc.), and considering both near-field and far-field propagation conditions at mmWave frequencies. In particular, the analysis presented in this chapter differs from the previous ones in several aspects, as listed hereafter.

- ETs, modeled according to a binomial distribution (BND), are considered.
- A multistatic JSC system is considered, which consists of one Tx and two Rxs and is capable of exploiting spatial diversity (as introduced in section 1.2.1), i.e., viewing the target from different perspectives, to obtain an accurate estimate of the ETs in the system's coverage area. Additionally, differently from the previous chapters, the setup considered in this chapter is based on HDA beamforming architectures which have been shown to be energy and cost-efficient. In fact, for

very large antenna arrays the implementation of fully digital architectures becomes extremely challenging due to the enormous data rate of the A/D conversion at each antenna element. In order to alleviate this problem, HDA architectures are commonly considered for massive MIMO communications [77].

- A general channel model is provided, which is valid for both near and far-field propagation conditions since it accounts for amplitude and phase variations at different antenna elements in the near-field and converges to the well-known LoS propagation model (like the one in (2.8)) in the far-field.

- Since a near/far-field channel model is considered, beamfocusing is performed instead of beamforming when the target/user is identified in the near-field of the Tx. This approach significantly improves localization and communication performance compared to traditional beamforming.

- Given that one of the main advantages of multistatic radar setups is to increase system robustness in terms of target detection, numerical examples show that by fusing the information from the two Rxs, it is possible to significantly increase target detection performance.

5.1 System Model

In this chapter, a multistatic JSC configuration is considered. In particular, as shown in Fig. 5.1, the system consists of a Tx and two Rxs units to form two bistatic Tx-Rx pairs and can operate in both near and far-field. The Tx and the Rxs can be connected by a fronthaul link to a central unit that coordinates sensing operations performed by different bistatic pairs, e.g., by performing synchronization between Tx and Rx in each pair and data fusion to improve target detection (as shown in section 5.4). In fact, as already mentioned, by using multiple Rxs it is possible to see the targets from different perspectives, thus providing a diversity gain, especially in the case

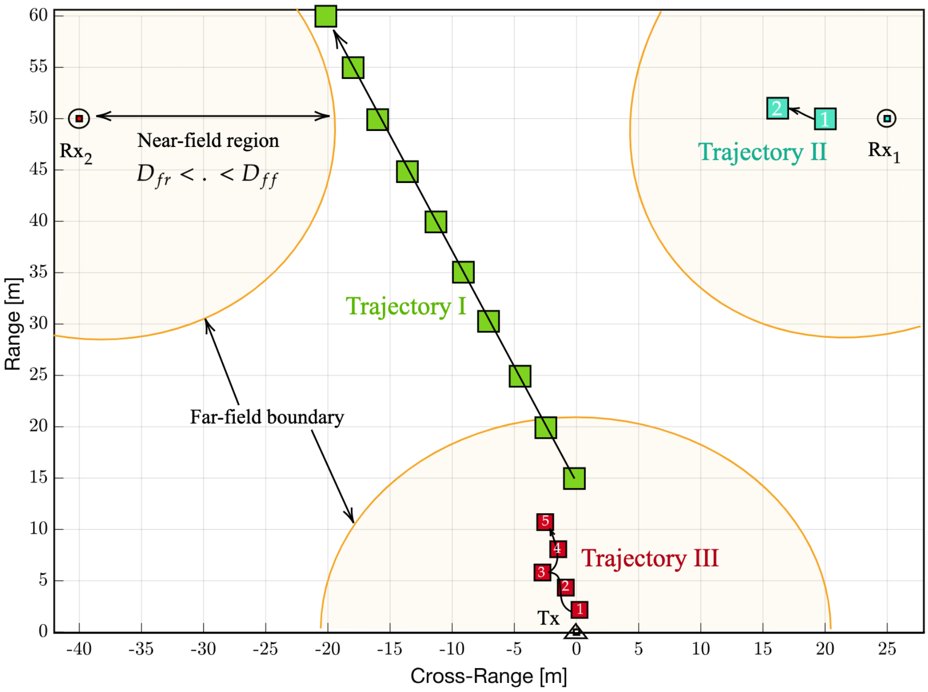

Figure 5.1: Schematic illustration of the considered JSC multistatic system to be used in an urban-type scenario. The trajectories shown in the figure model various locations and movement patterns that may occur with respect to the near and far-fields of the antenna arrays. We assume that the deployment has been planned so that the near-fields of the Tx/Rx pairs do not coincide. Each Tx/Rx pair is a bistatic pair whose geometric relationship is shown in Fig. 4.1. D_{fr} and D_{ff} have been defined in Section 1.3.

of ETs where different observation perspectives of targets result in different measurements [78].

Similar to the system model considered in the previous analysis, at Tx we assume to illuminate one scanning direction at a time using a beamformer $\mathbf{w} \in \mathbb{C}^{N_{\mathrm{T}} \times 1}$, where N_{T} is the number of transmit antennas, and scan the environment from one direction to another using a time division technique. In each direction, we consider that the Tx transmits a frame consisting of M OFDM symbols, for a duration equal to MT_{s}, and with a bandwidth of $B = K\Delta f$, where K is the total number of subcarriers, in order to perform the sensing task, i.e., to illuminate targets. Unlike the beam steering approach considered in the previous chapters, where the idea was to steer the power in the desired directions, here the Tx beamformers are designed to ensure that each of them covers a relatively large circular sector in space (centered in the considered sensing direction) with constant gain while maintaining very low gain elsewhere, with no overlap between different sectors. This is a possible solution to the side lobes problem discussed in Chapter 3. The considered design approach follows that presented in [79], and details are beyond the scope of this dissertation.

As already mentioned, the considered system can operate in both near and far-field. For this reason, at the Tx we consider not only the design of the beamformers, but also the design of the beamfocusing vectors. In fact, as it will be shown later, using a beamforming approach when the target is estimated to be in the near-field of the Tx leads to a degradation of the sensing performance due to the mismatch in the array response (see Section 1.3). The design of the beamfocusing vector considered in this work is explained in detail in [61] and some more details will be given in Section 5.3. The main idea is that instead of illuminating a specific circular sector as in beamforming, each vector is designed to focus the transmitted energy in a specific region centered at the coordinates (ϕ, r) (which does not overlap with others), so that an extended area is illuminated with relatively constant gain.

However, differently from the previous analysis, at the Rxs an HDA architecture is considered [77]. In particular, at each instant time, the Rxs scan the portion of space illuminated by the respective Tx beamformer. Consequently, parameter estimation is carried out specifically within this circular sector. This process continues sequentially until the entire desired monitored region has been covered. Since the here considered HDA architecture does not allow conventional MIMO radar processing, multiple samples of the space are required for angle estimation. To address this, a codebook containing a set of N_{R} discrete Fourier transform (DFT) orthogonal beams as $\mathcal{U}_{\mathrm{DFT}} \coloneqq (\mathbf{u}_1, ..., \mathbf{u}_{N_{\mathrm{R}}}) \in \mathbb{C}^{N_{\mathrm{R}} \times N_{\mathrm{R}}}$ selected from the Fourier basis ($\in \mathbb{C}^{N_{\mathrm{R}} \times N_{\mathrm{R}}}$), where N_{R} is the number of antenna array elements at each Rx. Subsequently, $N_{\mathrm{R}}^{\mathrm{rf}}$ beams out of the N_{R} are selected at Rx units, ensuring coverage of a desired region of interest in the beam space (i.e., covering the illuminated region by the Tx) resulting in the formation of the reduction matrix $\mathbf{U} \in \mathbb{C}^{N_{\mathrm{R}} \times N_{\mathrm{R}}^{\mathrm{rf}}}$.

It is worth noting that the HDA system model considered in this chapter can easily be converted to the fully digital system considered previously. In this case, $N_{\mathrm{R}}^{\mathrm{rf}} = N_{\mathrm{R}}$ radio frequency (RF) chains are used to demodulate and sample all the antennas of the radar Rx, allowing fully digital processing.

5.1.1 Extended target model

It is a common practice to represent an ET as a set of fixed point-scatterers. As an alternative approach, it is possible to produce a measurement model (likelihood) in terms of the spatial density of measurements in the intended sensing area. Specifically, motivated by finite element discretization techniques commonly used for RCS characterization [80], in this analysis, the target is modeled as a set of grid elements $\mathcal{P}$ within a designated rectangular region $\mathbf{A} \subset \mathbb{R}^2$ with an area of $|\mathbf{A}|$, as shown in Fig. 5.2. At each instant the radar measurement is made, the ET representing a UE (e.g., vehicle, motorcycle, etc.) is composed of a random number $P \leq |\mathcal{P}|$ of scatterers. Given that each grid point inside $\mathbf{A}$ can be active with probability q, the number of active points P follows a BND, with probability q and number of trials $|\mathcal{P}|$, i.e., $P \sim \mathrm{B}(q, |\mathcal{P}|)$. Then, the probability of having p active points at each instant is given by the probability mass function[1]:

$$\Pr(P = p) = \binom{|\mathcal{P}|}{p} q^p (1-q)^{|\mathcal{P}|-p}.$$

Then, P points (elements) are drawn i.i.d. from $\mathcal{P}$ such that $P \subseteq \mathcal{P}$.

In the considered channel model, each individual scattering point (represented by an element) is characterized only by its LoS path since mmWave channels are characterized by large isotropic attenuation, so multipath components are typically much weaker than the LoS and disappear below the noise floor after reflection, especially for the scattering channel seen by the radar receiver [81,82]. In the following analysis, we assume that the reflection points observed by each Rx unit are generated by a separate BND process at each instant of time.

---

[1] Interesting to note that, considering a finite but very large number of elements on the grid, i.e. $|\mathcal{P}| \to \infty$, each of which is independent active or non-active, the binomial distribution can also be very well approximated by a Poisson distribution, with intensity $\gamma = q|\mathcal{P}|$.

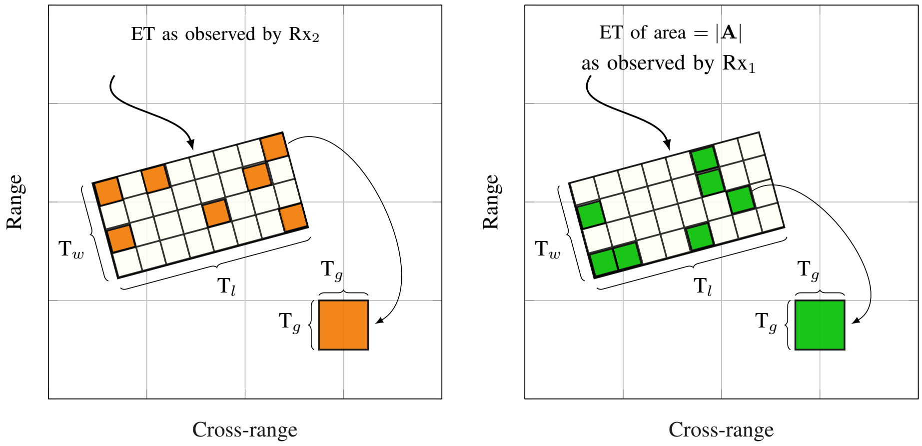

Figure 5.2: Schematic of the ET model, composed of scattering point clusters determined through a BND. Note that each Rx observes a different scattering profile of the ET at each measurement instance.

5.1.2 Near/far-field channel model

As already mentioned, the considered multistatic JSC system based on OFDM can operate in both near and far-field. In particular, the urban scenario shown in Fig. 5.1 allows the simultaneous presence of far-field and neaf-field conditions in the direct and reflected channels. The difference between these two regimes in terms of sensing parameters estimation has already been explained in Section 1.3. The purpose of this section is to provide a general formulation of the channel model that is valid for both conditions [33]. The channel model is derived considering the presence of L ETs in the monitored area, each of which is modeled according to a BND as described in Section 5.1.1.

For simplicity, we start the channel derivation by considering a single scatterer p (taken from a generic ET l) located at $\mathbf{p}_p = r_{i,p}[\cos\phi_{i,p}, \sin\phi_{i,p}]^T$ and a transmit ULA i having N_T elements located at $\mathbf{p}_{i_n} = [0, nd]^T$, with $n = -\frac{N_\mathrm{T}-1}{2}, \dots, \frac{N_\mathrm{T}-1}{2}$, the antenna index, and d the spacing between the elements, here set to half the wavelength. We denote with $r_{i,p}$ and $\phi_{i,p}$ respectively the reference distance and the reference DoD between Tx i and the scatterer p, calculated with respect to the center of the array [2]. Considering LoS

---

[2] Note that, without loss of generality, in Chapter 2 and Chapter 4 the first antenna element of the array has been considered as a reference point.

propagation conditions, the equivalent low-pass complex channel coefficient for the channel between the single antenna element i_n and the scatterer p at the k-th subcarrier $f_k = f_\mathrm{c} + k\Delta f$, with $k = -K/2, \ldots, K/2-1$, and m-th OFDM symbol can be written as

$$h_{i_n,p}[k,m] = \sqrt{\xi_{i_n,p}} e^{-j\left(2\pi\left(\frac{r_{i_n,p}}{c} f_k - mT_\mathrm{s} f_{\mathrm{D,i,p}}\right)+\varphi_0\right)} \tag{5.1}$$

where $f_{\mathrm{D,i,p}}$ is the Doppler shift, $r_{i_n,p} = \|\mathbf{p}_p - \mathbf{p}_{i_n}\|_2$ is the distance between the i_n-th antenna of the Tx i and the scatterer p, c is the speed of light, $\varphi_0 \in \mathcal{U}_{[0,2\pi)}$ is the phase offset between Tx and Rx. Furthermore, $\xi_{i_n,l}$ is the gain factor of the channel between the antenna i_n and the scatterer p, which can be written, considering LoS propagation conditions, as follows

$$\xi_{i_n,p} = \frac{\sigma_{i,p}}{4\pi r_{i_n,p}^2} \tag{5.2}$$

with $\sigma_{i,p}$ the RCS of the scatterer p, illuminated by the Tx i.

By performing simple algebraic manipulations on (5.1), the channel vector $\mathbf{h}_{i,p}[k,m] \in \mathbb{C}^{1\times N_\mathrm{T}}$ associated with subcarrier k and scatterer p at time instant m, can be obtained as

$$\mathbf{h}_{i,p}[k,m] = \alpha_{i,p} e^{j2\pi(mT_\mathrm{s} f_{\mathrm{D,i,p}} - k\Delta f \tau_{i,p})} \mathbf{a}^\dagger(\phi_{i,p}, r_{i,p}) \tag{5.3}$$

where $\alpha_{i,p} = \sqrt{\xi_{i,p}} e^{-j(2\pi f_\mathrm{c} \tau_{i,p} + \varphi_0)}$ is the reference channel coefficient associated to scatterer p and computed with respect to the center of the antenna array; $\tau_{i,p} = r_{i,p}/c$ is the reference propagation delay and $\xi_{i,p}$ the reference channel gain, while $\mathbf{a}(\phi_{i,p}, r_{i,p}) \in \mathbb{C}^{N_\mathrm{T}\times 1}$, is the array response vector, given by

$$\mathbf{a}(\phi_{i,p}, r_{i,p}) = \begin{pmatrix} \frac{r_{i,p}}{r_{0,p}} \exp(-j\frac{2\pi f_c}{c}(r_{0,p} - r_{i,p})) \\ \frac{r_{i,p}}{r_{1,p}} \exp(-j\frac{2\pi f_c}{c}(r_{1,p} - r_{i,p})) \\ \vdots \\ \frac{r_{i,p}}{r_{N_\mathrm{T}-1,p}} \exp(-j\frac{2\pi f_c}{c}(r_{N_\mathrm{T}-1,p} - r_{i,p})) \end{pmatrix}. \tag{5.4}$$

The relationship between the reference distance $r_{i,p}$ and the distance of the i_nth antenna element from the scatterer p can be obtained from a second order Taylor expansion, as follows [33]

$$r_{i_n,p} - r_{i,p} \approx \frac{(nd\cos\phi_{i,p})^2}{2r_{i,p}} - nd\sin\phi_{i,p}. \tag{5.5}$$

By replacing (5.5) in (5.4) and considering $|nd| \ll r_{i,p}\,\forall n$, and $r_{i,p}/r_{i_n,p} \approx 1$ as reasonable assumptions in the far-field, when $d = c/(2f_c)$ we get the same array response vector as in (2.6). Therefore, (5.4) can be rewritten as

$$\mathbf{a}(\phi_{i,p}) = [e^{-j\frac{N_\mathrm{T}-1}{2}\pi\sin\phi_{i,p}}, \dots, e^{j\frac{N_\mathrm{T}-1}{2}\pi\sin\phi_{i,p}}]^T. \tag{5.6}$$

Similarly, the vector $\mathbf{h}_{p,j}[k,m] \in \mathbb{C}^{N_\mathrm{R}\times 1}$ representing the channel between a given scatterer p and a Rx unit j (consisting of N_R antenna elements) related to the k-th subcarrier and time instant m is given by

$$\mathbf{h}_{p,j}[k,m] = \beta_{p,j} e^{j2\pi(mT_\mathrm{s}f_\mathrm{D,p,j} - k\Delta f\tau_{p,j})}\mathbf{b}(\theta_{p,j},\gamma_{p,j}) \tag{5.7}$$

where $\tau_{p,j} = \gamma_{p,j}/c$ is the reference propagation delay, with $\gamma_{p,j}$ the distance between the scatterer p and the center of the antenna array j, $\beta_{p,j} = \sqrt{\zeta_{p,j}}e^{-j2\pi f_\mathrm{c}\tau_{p,j}}$ is the reference channel coefficient, while $\mathbf{b}(\theta_{p,j},\gamma_{p,j}) \in \mathbb{C}^{N_\mathrm{R}\times 1}$ is the array response vector computed as in (5.4), with $\theta_{p,j}$ the reference DoA. Considering LoS propagation conditions and isotropic antenna elements with effective area $A = c^2/(4\pi f_\mathrm{c}^2)$, the gain factor $\zeta_{p,j}$ can be written as

$$\zeta_{p,j} = \frac{c^2}{(4\pi\, f_c\, \gamma_{p,j})^2}. \tag{5.8}$$

Let us now consider ET l. Each of the Tx-Rx bistatic pairs with index (i,j) can collect echoes from a random set $P_{i,j}^{(l)} \subseteq \mathcal{P}$ of these points [3]. Considering (5.3) and (5.7), the generalized near/far-field $N_\mathrm{R} \times N_\mathrm{T}$ bistatic MIMO channel between Tx i and Rx j, considering the presence of the ET l, at k-th

---

[3] In the following, for the sake of brevity, we denote by $P = |P_{i,j}^{(l)}|$ the random number of scatterers related to the target l and seen by the bistatic pair (i,j).

subcarrier and m-th time instant can be written similar to (4.9), as follows

$$\mathbf{H}_{i,j}[k,m] = \sum_{p=1}^{P} \varepsilon_p e^{j2\pi(mT_{\mathrm{s}}f_{\mathrm{D},p} - k\Delta f \tau_p)} \mathbf{b}(\theta_{p,j}, \gamma_{p,j}) \mathbf{a}^{\dagger}(\phi_{i,p}, r_{i,p}) \tag{5.9}$$

where $\varepsilon_p = \alpha_{i,p}\beta_{p,j}$ and $\tau_p = \tau_{i,p} + \tau_{p,j}$ are the bistatic complex channel factor and bistatic propagation delay, respectively, associated with the p-th scatterer of the target, while $f_{\mathrm{D},p} = f_{\mathrm{D},i,p} + f_{\mathrm{D},p,j}$ is the bistatic Doppler shift, defined in (4.3).

5.1.3 Input-output relationship

Similar to (2.1), the OFDM frame transmitted from Tx i to target l is here defined as

$$\mathbf{s}_{i,l}(t) = \mathbf{w}_l \sum_{k=0}^{K-1} \sum_{m=0}^{M-1} x_{i,l}[k,m] g_{k,m}(t) \tag{5.10}$$

where $\mathbf{w}_l \in \mathbb{C}^{N_{\mathrm{T}} \times 1}$ is a (unit-norm) transmit beamforming (in the far-field) or beamfocusing (in the near-field) vector to point toward l, and $x_{i,l}[k,m]$ is a generic complex modulation symbol of the $K \times M$ OFDM resource grid used at the Tx i to estimate range, angle, and velocity parameters of the target l, while $g_{k,m}(t)$ is the pulse.

The noise-free N_{R}-dimensional continuous-time signal transmitted by i-th Tx, scattered by the ET l, and received from the j-th Rx is given by

$$\begin{aligned}
\mathbf{r}_{i,j}(t) =& \sum_{p=1}^{P} \varepsilon_p e^{j2\pi f_{\mathrm{D},p} t} \mathbf{b}(\theta_{p,j}, \gamma_{p,j}) \mathbf{a}^{\dagger}(\phi_{i,p}, r_{i,p}) \mathbf{s}_{i,l}(t - \tau_p) \\
=& \sum_{p=1}^{P} \varepsilon_p e^{j2\pi f_{\mathrm{D},p} t} \mathbf{b}(\theta_{p,j}, \gamma_{p,j}) \mathbf{a}^{\dagger}(\phi_{i,p}, r_{i,p}) \times \\
& \times \mathbf{w}_l \sum_{k=0}^{K-1} \sum_{m=0}^{M-1} x_{i,l}[k,m] g_{k,m}(t - \tau_p).
\end{aligned} \tag{5.11}$$

In the following analysis, we place an assumption that multiple (extended) targets are sufficiently separated in space, i.e., $|\mathbf{a}^{\dagger}(\phi_{i,l}, r_{i,l}) \mathbf{w}_{l'}(\hat{\phi}_{i,l'}, \hat{r}_{i,l'})| \approx 0$

for $l' \neq l$, where $\hat{\phi}_{i,l'}$ is the pointing direction (DoD) for a Tx beamformer $\mathbf{w}_{l'}$ associated with the l'-th (extended) target.

As already mentioned, at the Rx an HDA architecture is considered, thus the received signal $\mathbf{r}_{i,j}(t)$ is processed by a reduction matrix before sampling. In particular, we focus the radar Rx on a single target l for M OFDM symbols and estimate different targets sequentially in time. To achieve this, a reduction matrix $\mathbf{U} \in \mathbb{C}^{N_\mathrm{R} \times N_\mathrm{R}^{(\mathrm{rf})}}$ is chosen to cover a particular area in the current sensing direction/region (determined by the current Tx beamformer). Then, after the OFDM demodulator, considering negligible inter-carrier interference (ICI) and ISI and including noise, a received time-frequency grid of complex elements $y[k,m]$ is obtained at each RF chain. Thus, considering the channel model in (5.9), the $N_\mathrm{R}^\mathrm{rf} \times 1$ vector of the received complex modulation symbols is given by

$$\begin{aligned} \mathbf{y}[k,m] &= \mathbf{U}^\dagger \mathbf{H}_{i,j}[k,m]\mathbf{w}_l x_{i,l}[k,m] \\ &= \sum_{p=1}^{P} \varepsilon_p \mathbf{U}^\dagger \mathbf{b}(\theta_{p,j}, \gamma_{p,j}) \mathbf{a}^\dagger(\phi_{i,p}, r_{i,p}) \mathbf{w}_l \times \\ &\times x_{i,l}[k,m] e^{j2\pi(mT_\mathrm{s} f_{\mathrm{D},p} - k\Delta f \tau_p)} + \tilde{\mathbf{n}}[k,m]. \end{aligned} \tag{5.12}$$

where $\tilde{\mathbf{n}} \sim \mathcal{CN}(\mathbf{0}, \sigma_\mathrm{\tilde{n}}^2 \mathbf{I}_{N_\mathrm{R}^\mathrm{rf}})$ is the complex Gaussian noise.

By stacking the $K \times M$ OFDM symbol grid into a $KM \times 1$ vector $\underline{\mathbf{x}}$, the received signal $\underline{\mathbf{y}} \in \mathbb{C}^{N_\mathrm{R}^\mathrm{rf} KM \times 1}$ can then be written as

$$\underline{\mathbf{y}} = \sum_{p=1}^{P} \varepsilon_p \mathbf{G}(f_{\mathrm{D},p}, r_{i,p}, \gamma_{p,j}, \theta_{p,j}, \phi_{i,p}) \underline{\mathbf{x}} + \underline{\tilde{\mathbf{n}}}. \tag{5.13}$$

where $\mathbf{G}(\cdot)$ is the effective channel matrix of dimension $N_\mathrm{R}^\mathrm{rf} KM \times KM$, that is defined for a single scatterer p as follows

$$\mathbf{G}(f_{\mathrm{D},p}, r_{i,p}, \gamma_{p,j}, \theta_{p,j}, \phi_{i,p}) \triangleq \mathbf{T} \otimes \Big(\mathbf{U}^\dagger \mathbf{b}(\theta_{p,j}, \gamma_{p,j}) \mathbf{a}^\dagger(\phi_{i,p}, r_{i,p}) \mathbf{w}_l \Big) \tag{5.14}$$

---

where $\mathbf{T}(\tau, f_{\mathrm{D}}) \in \mathbb{C}^{MK\times MK}$ is defined as

$$\mathbf{T}(\tau, f_{\mathrm{D}}) = \operatorname{diag}\Big([1, \dots, e^{j2\pi m T_{\mathrm{s}} f_{\mathrm{D}}}, \dots, e^{j2\pi(M-1)T_{\mathrm{s}} f_{\mathrm{D}}}]^T \otimes [1, \dots, e^{-j2\pi k\Delta f\tau}, \dots, e^{-j2\pi(K-1)\Delta f\tau}]^T\Big). \quad (5.15)$$

For the derivation of the ML target parameter estimation in Section 5.2, we consider a single Tx and Rx pair and drop their respective indices, $(.)_{i,j}$, to avoid excessive notation clutter. Needless to say, the same formulation holds for other pairs. Moreover, we assume $N_{\mathrm{T}} = N_{\mathrm{R}} = N_{\mathrm{a}}$ and $N_{\mathrm{R}}^{\mathrm{rf}} = N_{\mathrm{rf}}$.

5.2 Parameter Estimation and Detection

Considering the scenario shown in Fig. 5.1, where a target can be in the near or far-field of the Tx or one of the Rxs, the target parameter estimation can be performed in two different ways. In particular, as explained in Section 5.1.2, when the target is in the near-field of the Rx, the array response in (5.7) is a function of both angle and distance (as in (5.4)), so it is possible to estimate the position of the target directly. Conversely, in the far-field, the array response is only a function of angle, i.e, $\mathbf{b}(\theta, \gamma) \to \mathbf{b}(\theta)$, and an estimate of the range γ can be obtained from the estimate of the propagation delay τ and the DoA θ, according to (4.1) and (4.2). In addition, if the target is in the near-field of the Tx, using a beamforming approach to illuminate the target will result in a loss of gain as shown in Fig. 1.5. In this case, a beamfocusing approach can be used to focus the energy in this area and improve the SNR associated with the target, thus improving the estimation accuracy.

Since we assume that we do not know a priori whether a target is in the far or near-field of Tx or one of the Rx, a two-stage ML parameter estimation framework is introduced. In the first stage, we consider scanning the environment in time-division and illuminating each target through beamforming, and a coarse parameter estimation is performed based on bistatic far-field assumptions at the Rx units. Then, based on the estimates obtained from the first stage, if the target is determined to be in the near-field region of either the Tx or Rx units, a second estimation stage is performed. As mentioned before, depending on the target being located in the near-field of the Tx or Rx, the second stage will differ. More details are given in the following sections.

Important to note that when the near-field cases occur in the initial stage, the model mismatch between the near-field and far-field array response vectors presented in Section 5.1.2 leads to poorly localized estimates. However, these approximate and inaccurate estimates are used to define a region of interest (RoI) for further processing based on the more correct near-field model.

Stage 1: Far-field beamforming and bistatic estimation

In the first stage, we assume no knowledge of the target position. The appropriate far-field beamformer is selected at the Tx, and based on the assumption that the ET is located in the far-field of both the Tx and the Rx units, the array responses at the Tx and the Rx units in (5.14), which are only functions of angular parameters (i.e., $\mathbf{a}(\phi, r) \to \mathbf{a}(\phi)$ and $\mathbf{b}(\theta, \gamma) \to \mathbf{b}(\theta)$) are considered for parameter estimation. As such, the effective channel matrix $\mathbf{G}(f_{\mathrm{D},p}, r_p, \gamma_p, \theta_p, \phi_p)$ in (5.14) takes the form

$$\breve{\mathbf{G}}(f_{\mathrm{D},p}, \tau_p, \theta_p) \overset{\triangle}{=} \mathbf{T} \otimes \left(\mathbf{U}^{\dagger}\mathbf{b}(\theta_p)\mathbf{a}^{\dagger}(\phi_p)\mathbf{w}(\hat{\phi}_p)\right). \tag{5.16}$$

It is worth noting that from the perspective of the bistatic Rx, the channel response from Tx to the target is a constant that can be absorbed in the channel gain coefficient, i.e.,

$$g_p \overset{\triangle}{=} \mathbf{a}^{\dagger}(\phi_p)\mathbf{w}(\hat{\phi}_p)\ ,\ h_p \overset{\triangle}{=} g_p\varepsilon_p$$

and therefore, $\breve{\mathbf{G}}$ is not a function of the DoD, ϕ. Then, the received signal in (5.13) can be recast as

$$\underline{\mathbf{y}} = \sum_{p=1}^{P} h_p\breve{\mathbf{G}}(f_{\mathrm{D},p}, \tau_p, \theta_p)\underline{\mathbf{x}} + \underline{\tilde{\mathbf{n}}}. \tag{5.17}$$

From (5.17), the vector of parameters to be estimated is defined as

$$\boldsymbol{\theta} = \{h_p, f_{\mathrm{D,p}}, \tau_p, \theta_p\}_{p=0}^{P-1}. \tag{5.18}$$

For an ET with P scattering points, the ML estimate of the set $\boldsymbol{\theta}$ involves solving the following equation (5.19) in a search space $\Gamma_{\mathrm{FF}} \triangleq \mathbb{C}^P \times \mathbb{R}^{3P}$

$$\boldsymbol{\theta}_{\mathrm{ML}} = \underset{\{h_p, f_{\mathrm{D,p}}, \tau_p, \theta_p\}_{p=0}^{P-1} \in \Gamma}{\arg\min} \left\| \underline{\mathbf{y}} - \sum_{p=1}^{P} h_p \breve{\mathbf{G}}(f_{\mathrm{D},p}, \tau_p, \theta_p) \underline{\mathbf{x}} \right\|_2^2 . \tag{5.19}$$

The solution of (5.19) requires knowledge of the number of scattering points P, which can be formulated as a model order estimation problem (see e.g., Section 2.2.1). Since the micro-scatterers of ETs are often indistinguishable due to the system resolution, the estimation of the model order is an unattainable task due to the problem being intrinsically ill-posed [83]. In addition, the parameter space of the brute force ML solution in (5.19) requires prohibitively large computations.

For this reason, a possible solution, in this case, is to resort to an approximate method that evaluates a hypothesis test on a set of $(f_{\mathrm{D}}, \tau, \theta)$ tuples belonging to a grid Θ. By maximizing the log-likelihood function with respect to the amplitude h, the log-likelihood ratio (LLR) takes the form [61]

$$\ell(f_{\mathrm{D}}, \tau, \theta) = \frac{\left| \mathbf{b}^{\dagger}(\theta) \boldsymbol{\xi}(f_{\mathrm{D}}, \tau) \right|^2}{\mathbf{b}^{\dagger}(\theta) \bar{\mathbf{U}} \mathbf{b}(\theta)} \tag{5.20}$$

where the following definitions are used

$$\begin{aligned} \bar{\mathbf{U}} &= \|\underline{\mathbf{x}}\|_2^2 \mathbf{U}\mathbf{U}^{\dagger} \\ \boldsymbol{\xi}(f_{\mathrm{D}}, \tau) &= \left[\underline{\mathbf{x}}^{\mathrm{T}} \mathbf{T}(f_{\mathrm{D}}, \tau) \mathbf{Y}^{\dagger} \mathbf{U}^{\dagger} \right]^{\mathrm{T}} \\ \mathbf{Y} &= \Big[\underline{\mathbf{y}}[0,0], \ldots, \underline{\mathbf{y}}[M-1, K-1] \Big]. \end{aligned} \tag{5.21}$$

Then, the LLR test is given by

$$\ell(f_{\mathrm{D}}, \tau, \theta) \underset{\mathcal{H}_0}{\overset{\mathcal{H}_1}{\gtrless}} T_r \ , \quad (f_{\mathrm{D}}, \tau, \theta) \in \Theta \tag{5.22}$$

where, for this analysis, the threshold T_r is chosen at each grid point by using the ordered statistic constant false alarm rate (OS-CFAR) approach described in [84]. By defining a suitably refined search grid on $\Theta_{\mathrm{FF}} \triangleq \mathbb{R}^{3P}$, and evaluating (5.20) for every tuple $(f_{\mathrm{D}}, \tau, \theta) \in \Theta_{\mathrm{FF}}$ and performing the estimation and detection (thresholding) step according to (5.22), the estimates $(\hat{f}_{\mathrm{D}}, \hat{\tau}, \hat{\theta})$ of the scattering points can be obtained. To convert these values to the angle and range of the target in the global coordinates, bistatic conversion principles presented in Section 4.1.1 can be used.

Stage 2: Estimation in the Rx near-field

If the target is determined to be in the near-field of an Rx array, the second stage performs another ML estimation of the target parameters with the correct near-field model, resulting in significantly improved estimation performance. The correct ML estimator for this scenario is derived below.

In this case, the received signal in (5.13) is considered and the vector of parameters to be estimated is defined as

$$\boldsymbol{\theta} = \{\varepsilon_p, f_{\mathrm{D,p}}, r_p, \gamma_p, \theta_p, \phi_p\}_{p=0}^{P-1}. \tag{5.23}$$

Similar to the previous far-field case, maximizing the log-likelihood function over the amplitude ε_p, the LLR test takes on the form [61]

$$\ell(f_{\mathrm{D}}, r, \gamma, \theta, \phi) = \frac{\left|\mathbf{w}^{\dagger}\mathbf{a}\mathbf{b}^{\dagger}\boldsymbol{\xi}(f_{\mathrm{D}}, r, \gamma)\right|^2}{\mathbf{w}^{\dagger}\mathbf{a}\mathbf{b}^{\dagger}\bar{\mathbf{U}}\mathbf{b}\mathbf{a}^{\dagger}\mathbf{w}} \underset{\mathcal{H}_0}{\overset{\mathcal{H}_1}{\gtrless}} T_r \tag{5.24}$$

with $(f_{\mathrm{D}}, r, \gamma, \theta, \phi) \in \Theta_{\mathrm{NF}} \triangleq \mathbb{R}^5$.

This means the ML metric in (5.24) needs to be evaluated on a fine-grained grid defined over Θ to meet high accuracy localization requirements. It is clear that evaluating a 5-D search grid is computationally heavy. Therefore, an appropriately refined Cartesian grid can be defined over the RoI indicated by the coarse estimates from the first step.

Stage 2: Estimation in the Tx near-field

If the presence of targets in the near-field of the Tx is detected, the scheme switches from beamforming to a beamfocusing approach at the Tx, thus increasing the SNR at the intended target location, and so the estimation performance. Considering the possibility that the detected target may be a communication user, the ability to properly illuminate it can also lead to a significant increase in communication performance (i.e., spectral efficiency). To obtain the beamfocusing weights, a beamfocusing codebook at Tx is utilized where the codewords are designed to maintain an (almost) constant gain within an extended spatial region. Note that in this case, the Rxs can use the far-field model due to the deployment topology, as shown in Fig. 5.1).

5.3 Design of the Beamfocusing Weights

As explained in the previous section, if the target is determined to be in the near-field of the Tx, a beamfocusing approach should be considered to improve the SNR. Recently, several works have dealt with near-field beamfocusing schemes, especially in the reconfigurable reflecting surfaces domain, due to the large array sizes used therein [85, 86]. While a few works have investigated the use of beamfocusing weights obtained by conjugating the near-field array response (same as the beam steering approach in beamforming), others have resorted to optimization-based methods to obtain suitable weights [32, 36]. The most significant drawback of those methods is that a very accurate estimate of the intended user coordinates (equivalently *range* and *angle*) is required. Even when ignoring the cost of obtaining such estimates, these techniques pose another significant challenge since the goal is to focus beams on the UE's antenna. In the very likely scenario of physically ETs (e.g., motorbikes, bicycles, cars, etc.) the UE antenna can be located anywhere on the object and the estimated reflection points do not necessarily correspond to the reflections from the antenna.

Approaches related to near-field codebook-based techniques have also been employed but they present some drawbacks. For example, the approach proposed in [86] presents spectral leakages in unwanted locations which beats the purpose of user-interference reduction via beamfocusing. From the sensing perspective, this leads to reflection from unintended objects that may be located in the undesired illuminated areas.

5.3.1 Problem formulation

Considering the issues mentioned above, a possible solution can be to consider a codebook-based scheme inspired by flat-top beamforming techniques that provide an (almost) constant gain over an extended circular sector. For this reason, the beamfocusing approach considered in this analysis aims to synthesize beamfocusing weights for array operation in near-field such that an extended area is illuminated with a relatively constant gain.

Let us start by defining a set $G = G_\theta G_r$ of discrete tuple points $(\tilde{\phi}_i, \tilde{r}_j),\ i \in [G_\theta],\ j \in [G_r]$. Let A be a matrix that contains array response vectors computed for each tuple pair $(\tilde{\phi}_i, \tilde{r}_j)$, as per (5.4), such that $\mathbf{A} = [\mathbf{a}(\tilde{\phi}_1, \tilde{r}_1), \ldots, \mathbf{a}(\tilde{\phi}_{G_\theta}, \tilde{r}_{G_r})] \in \mathbb{C}^{N_\mathrm{a} \times G}$.
The optimization problem under consideration can be expressed as a magnitude least-squares problem shown in equation (5.25). This problem falls under the category of problems discussed in [87, 88], and can be formulated as follows

$$\begin{aligned} \min_{\mathbf{w}} \quad & \|\, |\mathbf{A}^\dagger \mathbf{w}| - \bar{\mathbf{b}} \|_2^2 \\ \text{s.t.} \quad & \mathbf{w}^\dagger \mathbf{A}\mathbf{A}^\dagger \mathbf{w} = 1 \end{aligned} \tag{5.25}$$

where $\mathbf{w} \in \mathbb{C}^{N_\mathrm{a} \times 1}$ is the beamfocusing vector to be designed and $\bar{\mathbf{b}} \in \mathbb{R}_+^G$ is the desired radiation pattern. This is fixed to have a constant level in a pre-determined angle-range zone (i.e., spot) in the near-field of the array, and such that the values corresponding to the rejection directions (sidelobes) are below a certain threshold with respect to the maximum (center beam). The constraint in (5.25) imposes unit transmit power.

The above problem in (5.25) is not convex, and therefore by performing a semidefinite relaxation, acceptable solutions can be obtained. Due to the typically large number of columns in $\mathbf{A} \in \mathbb{C}^{N_\mathrm{a} \times G}$, the above program is memory and computationally expensive, so it is possible to resort to an iterative method. Further details on the solution to this problem are beyond the scope of this dissertation. For a full understanding, the reader is referred to [61].

Table 5.1: Simulation parameters

System Parameters		Target Parameters
$P_{\mathrm{T}} = 26$ [dBm]	$M = 6$	$\mathrm{T}_l = 1.5$ [m]
$B = 128$ [MHz]	$K = 100$	$\mathrm{T}_w = 1$ [m]
$\mathrm{F} = 3$ [dB]	$f_{\mathrm{c}} = 28.0$ [GHz]	$\mathrm{T}_g = 0.1$ [m]
$N_0 = 2 \cdot 10^{-21}$ [W/Hz]	$N_{\mathrm{a}} = 64$	$q \approx 0.01$
$P_{\mathrm{fa}} = 10^{-3}$	$N_{\mathrm{rf}} = 8$	$\sigma_{\mathrm{rcs}} = 1$ [m^2]

5.4 Simulation Results

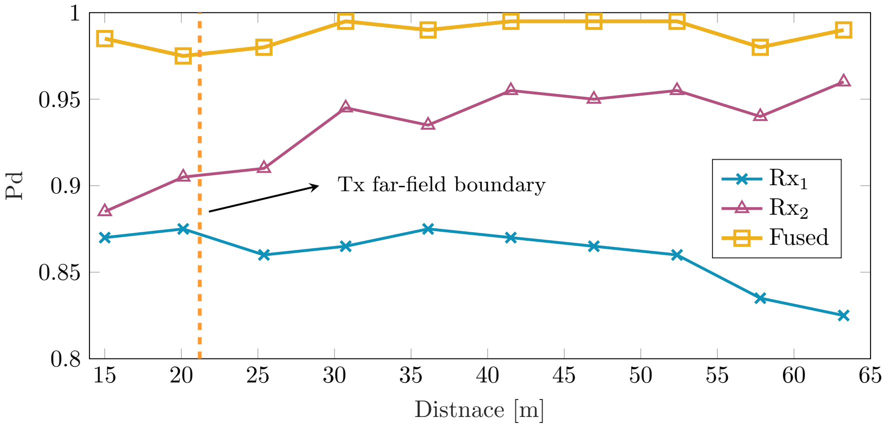

Figure 5.3: Probability of detection for an ET along trajectory I in Fig. 5.1. The x-axis indicates the radial distance from the Tx.

In this section, some numerical results for the considered multistatic setting are given. The results are based on the scenario and topology in Fig. 5.1, where we consider different trajectories, enumerated from I to III, to simulate the different conditions that may be encountered in a real-world deployment. Unless otherwise stated, at each location along the trajectories, we consider an instance of the ET generated according to the BND in Section 5.1.1 and with the dimensions provided in Tab. 5.1.

Multistatic spatial diversity gain (Trajectory I)

This analysis aims to demonstrate the effectiveness of multistatic configura-

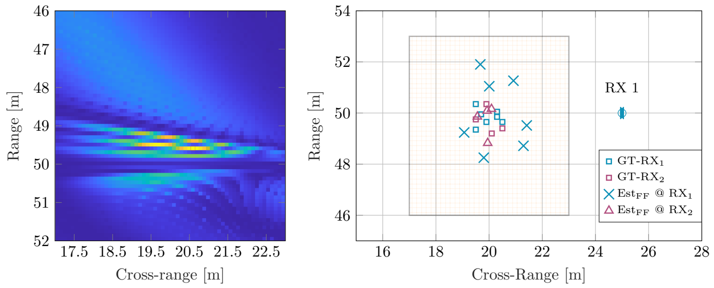

(a) Trajectory II-position 1

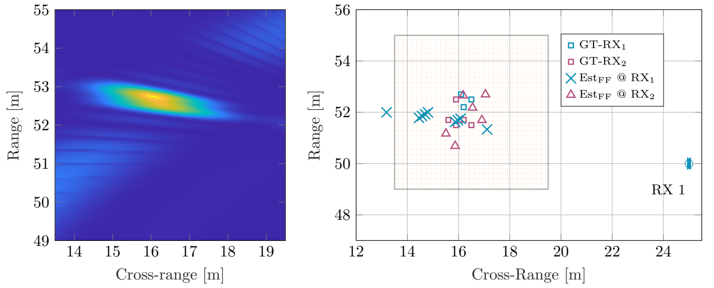

(b) Trajectory II-position 2

Figure 5.4: The figure shows an example of estimating the position of the target's scatterers when the ET is in the near-field of RX$_1$. (Trajectory II of Fig. 5.1).

tions in improving target detection. More specifically, it is well known that under different aspect angles, under which targets are observed by the Rx units in multistatic configurations, targets can exhibit very different reflection characteristics [89]. To this end, having multiple Rxs increases detection robustness. Given that an important distinction of radar systems utilizing multiple radars is to incorporate some level of data fusion between the measurement of individual sensors, the following experiments are performed to prove this. Fig. 5.3 depicts the average detection probability of the considered ET at each Rx, simulated 200 times for each Rx at the given points along Trajectory I in Fig. 5.1, where the detection is performed locally at each Rx using the OS-CFAR thresholding technique. A detection is declared if the main peak passes the threshold and the estimated position resulting from the peak value satisfies $\sqrt{(\hat{x}_p - x_p)^2 + (\hat{y}_p - y_p)^2} < 1$ [m].

Since, as already mentioned, at each realization the target scatterers are generated according to the BND introduced in Section 5.1.1, in some instances a Rx may observe very few or even zero scattering points from the

ET with non-zero probability. The *fused* curve shows the average detection probability if, at each step, either one of the Rxs has detected the target (i.e., OR operation). This fusion can be performed at a central node.

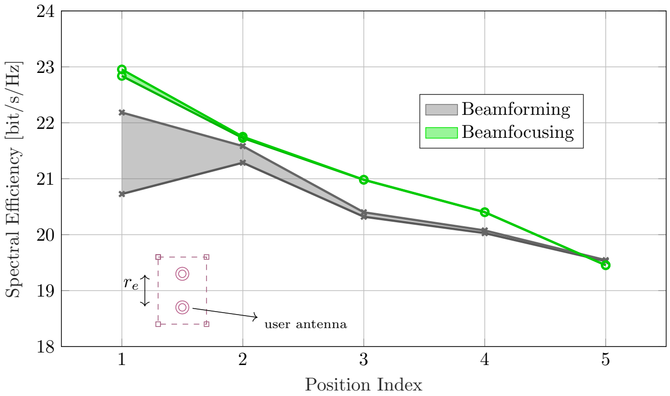

Figure 5.5: Beamfocusing vs beamforming spectral efficiency with an ET along trajectory III in Fig. 5.1. The target locations are indexed $1-5$. The filled area shows the gain within a mismatched antenna distance $r_e = 1$ [m] on the extended object.

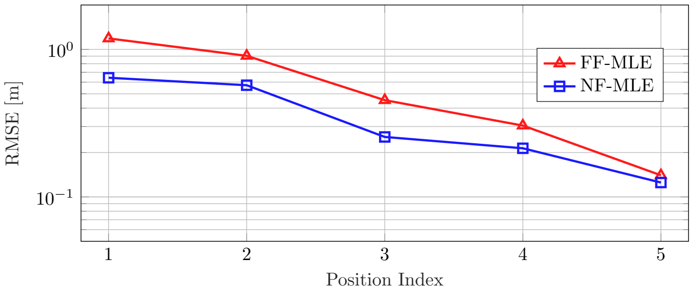

Figure 5.6: Comparison of RMSE of the target position using a near-field beamfocusing vector and a far-field beamforming vector.

Estimation of targets in the Rx near-field (Trajectory II)

Trajectory II in Fig. 5.1 considers an ET that is moving in the near-field of Rx_1. Performing a first estimation through the far-field mismatched model (evaluating (5.20)) a coarse estimation of the ET scatterer is obtained as shown in Fig. 5.4. Then by defining an RoI based on these estimates, (5.24) is evaluated on a fine-grained grid defined over the RoI, comprsing a 6×6 [m^2] square with 0.05 [m] pixels. Fig. 5.4a corresponds to the closer target location on the trajectory, where it can be observed that it is possible to individually resolve many of the point scatterers with high accuracy (much superior to the bandwidth imposed range resolution). Fig. 5.4b depicts the same procedure, however, since the target is now further from Rx_1, the individual scattering points can not be resolved. Nonetheless, the estimated location is highly accurate. Note that the estimates obtained by Rx_2 for both positions correspond to the far-field model and since the target lies in its far-field, the estimates are accurate within the system limits (i.e., range and angular resolution).

Spectral efficiency and estimation performance enhancement with beamfocusing (Trajectory III)

By considering a LoS channel with free-space path loss $\text{PL} = (4\pi r/\lambda)^2$, the matching gain G_M and achievable spectral efficiency (SE) are respectively given by

$$G_\text{M} = |\mathbf{a}^\dagger(r_0, \phi_0)\mathbf{w}_\text{X}(\hat{r}, \hat{\phi})| \tag{5.26a}$$

$$\text{SE} = \log_2\left(1 + \frac{P_\text{tx}G_\text{M}^2}{N_0 W}\left(\frac{\lambda}{4\pi r_0}\right)^2\right) \tag{5.26b}$$

with (r_0, ϕ_0) being the true location of the target. $\mathbf{w}_\text{X} \in \{\mathbf{w}_\text{N}, \mathbf{w}_\text{F}\}$ is the Tx beamforming (beamfocusing) vector where $\mathbf{w}_\text{F}(\hat{\phi})$ is a codeword chosen from a discrete *Fourier* codebook $\in \mathbb{C}^{N_\text{a} \times N_\text{a}}$, as the codeword with the closest angular distance of the mainlobe peak with respect to the estimated DoD $\hat{\phi}$. Conversely, $\mathbf{w}_\text{N}(\hat{r}, \hat{\phi})$ is a codeword from the *custom-designed* codebook of beamfocusing vectors, as explained in Section 5.3.

Fig. 5.5 shows the achievable SE for the ET along Trajectory III. The plot is obtained by calculating the SE at a hypothetical user antenna that is mounted on the ET. Since the custom beamfocusing vectors are designed to cover an extended area with a constant gain, if the antenna position deviates from the expected location, the Fourier codeword performs significantly worse than beamfocusing words. To demonstrate more explicitly the parameter estimation performance with beamfocusing and beamforming, we consider a single point scatterer at each of the locations along trajectory III (in Fig. 5.1) and perform parameter estimation (at Rx) using beamforming and beamfocusing transmission. The results in Fig. 5.6 show an improved parameter estimation performance which can be attributed to the increase in SNR at the target location due to the use of beamfocusing.

5.5 Remarks

In this chapter, a JSC OFDM system in a multistatic configuration has been considered. Unlike the systems considered in the previous chapters, the framework proposed here is based on a HDA architecture and can perform beamforming or beamfocusing and ML parameter estimation based on both near-field and far-field assumptions. Moreover, ETs has been considered. Through numerical simulations, it has been shown that if after a coarse estimation with far-field assumptions the target turns out to be in the near field of the Rx arrays, a high-dimensional ML parameter estimation based on the exact signal model (i.e., the exact array response model) can be subsequently performed in a defined RoI to improve the estimation accuracy. In addition, if the target is determined to be in the near-field of the Tx, beam focusing can be performed to illuminate the target, and the Rxs can re-estimate the target parameters with improved accuracy due to an increased SNR.

Chapter 6

Monostatic Joint Sensing and Communication with OTFS

Unlike the previous chapters, this chapter aims to shift the analysis from OFDM modulation to OTFS. In particular, the system model and techniques for estimating the target parameters are presented by considering a monostatic JSC OTFS-based system. The discussion is based on [38, 39] and [11]. After introducing the system model in Section 6.1, the ML estimator and the Cramér-Rao lower bound (CRLB) are given in Section 6.2.

6.1 System Model

6.1.1 Physical model

The following analysis considers a monostatic JSC OTFS-based. In particular, we consider a scenario like the one shown in Fig. 6.1, where a BS equipped with a monostatic JSC transceiver, with full-duplex capabilities, is jointly used to communicate with UEs and simultaneously sense the environment by collecting signals backscattered from targets, by sharing resources. As for the systems presented in the previous chapters, by collecting these signals, the monostatic JSC system can estimate the distance and radial velocity of nearby targets.

Similar to OFDM, OTFS is a multicarrier modulation scheme that oper-

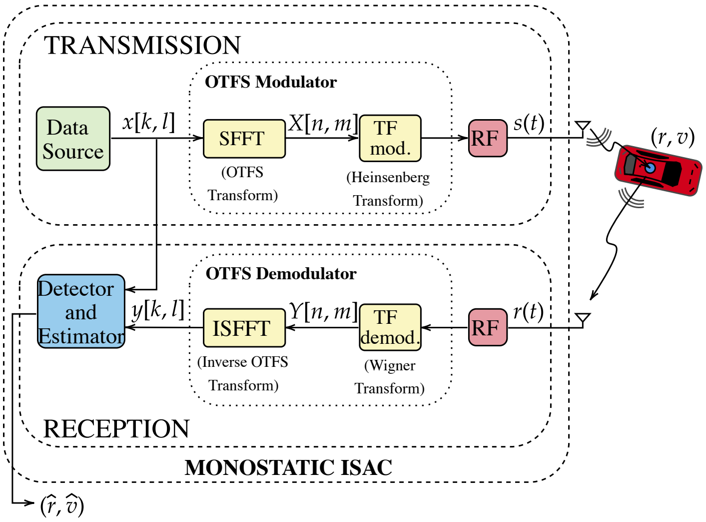

Figure 6.1: Signal-processing chain of the considered JSC OTFS-based system.

ates at a given carrier frequency f_c, with a bandwidth $B = M\Delta f$, where M is the number of subcarriers and $\Delta f = 1/T$ is the subcarrier spacing, with T the symbol time. Like OFDM, the relation between Δf and T is chosen to avoid ICI. However, unlike OFDM, in OTFS systems, it is possible to avoid the use of a cyclic prefix (needed to prevent ISI) by properly choosing the modulating and demodulating pulses, as will be explained in the next subsection [38].

Now, considering a generic scenario with P point-like targets each moving with a relative radial velocity v_{p} at a distance r_{p} from the monostatic transceiver, and considering LoS propagation conditions between the transceiver and the targets, the time-varying channel impulse response of the radar system can be written as

$$h(t,\tau) = \sum_{p=0}^{P-1} h_p \delta(\tau - \tau_p) e^{j2\pi f_{\mathrm{D},p} t} \tag{6.1}$$

where h_p is the complex channel gain, $f_{\mathrm{D},p} = \frac{2v_p f_c}{c}$ the Doppler shift and $\tau_p = \frac{2r_p}{c}$ the round-trip delay of the signal backscattered by the target p, with c the speed of light.

The time-continuous signal $s(t)$ to be transmitted on the channel, can be written as

$$s(t) = \sum_{n=0}^{N-1} \sum_{m=0}^{M-1} X[n,m] g_{\mathrm{tx}}(t - nT) e^{j2\pi m \Delta f (t-nT)} \tag{6.2}$$

where g_{tx} is the pulse shape, while $X[n,m] \in \mathbb{C}$ represents a generic modulation symbol, taken from a complex modulation alphabet, and defined in the time-frequency domain symbol grid at the output of the pre-processing block of OTFS modulator, as shown in Fig. 6.1. Symbols are arranged in the $N \times M$ grid $\mathbf{\Lambda}$, where N is the number of time slots. The so-called pre-processing operation simply consists of a symplectic finite Fourier transform (SFFT) that maps the symbols $x[k,l]$, generated by the transmitter in the delay-Doppler domain and belonging to the grid $\mathbf{\Lambda}^{\perp}$ of $M \times N$ dimension, to the time-frequency domain symbols $X[n,m]$, as

$$X[n,m] = \sum_{k=0}^{M-1} \sum_{l=0}^{N-1} x[k,l] e^{-j2\pi(\frac{mk}{M} - \frac{nl}{N})} \tag{6.3}$$

with $n, l = 0, ..., N-1$ and $m, k = 0, ..., M-1$.

Starting from (6.1) and (6.2), and neglecting the noise introduced by the communication channel for a while, the continuous-time received signal $r(t)$ is given by

$$r(t) = \int h(t,\tau) s(t-\tau) d\tau = \sum_{p=0}^{P-1} h_p s(t - \tau_p) e^{j2\pi f_{\mathrm{D},p} t}. \tag{6.4}$$

The received signal $r(t)$ is first given as an input to a matched filter, which performs cross-correlation between $r(t)$ and a demodulating pulse g_{rx}, and then discretizes the output signal in both the time and frequency domains. The g_{rx} pulse is chosen in relationship with g_{tx}, such that their inner product is bi-orthogonal with respect to translations by integer multiples of time T and frequency Δf [38]. This allows to avoid the use of the CP to prevent ISI.

As a result, first, the cross-ambiguity function $A_{g_{\mathrm{rx}},r}$, defined in the time-frequency domain, is obtained, as

$$\begin{aligned} Y(t,f) &= A_{g_{\mathrm{rx}},r}(\tau, f_{\mathrm{D}})|_{\tau=t, f_{\mathrm{D}}=f} \\ &= \int r(t') g^*_{\mathrm{rx}}(t'-t) e^{-j2\pi f(t-t')} dt'. \end{aligned} \tag{6.5}$$

Then, after a few mathematical manipulations, by sampling (6.5) at times $t = nT$ and frequencies $f = m\Delta f$), a $N \times M$ symbol grid in the time-frequency domain is obtained at the output of the matched filter, whose generic (n, m) element is given by

$$\begin{aligned} Y[n,m] &= Y(t,f)|_{t=nT, f=m\Delta f} \\ &= \sum_{n'=0}^{N-1} \sum_{m'=0}^{M-1} X[n',m'] H_{n,m}[n',m'] \end{aligned} \tag{6.6}$$

where, letting $h'_p \triangleq h_p e^{j2\pi f_{\mathrm{D},p}\tau_p}$, $H_{n,m}[n',m']$ is defined as

$$\begin{aligned} & H_{n,m}[n',m'] \\ & \triangleq \sum_{p=0}^{P-1} h'_p e^{j2\pi n' T f_{\mathrm{D},p}} e^{-j2\pi m \Delta f \tau_p} \\ & \times A_{g_{\mathrm{rx}},g_{\mathrm{tx}}} \left((n-n')\, T - \tau_p, (m-m')\, \Delta f - f_{\mathrm{D},p} \right). \end{aligned} \tag{6.7}$$

Lastly, the demodulated symbols, back in the delay-Doppler domain, are obtained after the post-processing block by performing the inverse symplectic finite Fourier transform (ISFFT) on the symbols in (6.6), as

$$\begin{aligned} y[k,l] &= \frac{1}{NM} \sum_{n=0}^{N-1} \sum_{m=0}^{M-1} Y[n,m] e^{j2\pi(\frac{mk}{M} - \frac{nl}{N})} \\ &= \sum_{k'=0}^{M-1} \sum_{l'=0}^{N-1} x[k',l'] g_{l,l'}[k,k'] \end{aligned} \tag{6.8}$$

where $g_{l,l'}[k,k']$ represents the ISI coefficient relative to the delay-Doppler pair $[k', l']$ seen by sample $[k, l]$, whose expression is given by

$$g_{l,l'}[k,k'] = \sum_{p=0}^{P-1} h'_p \boldsymbol{\Psi}^p_{l,l'}[k,k']. \tag{6.9}$$

where the matrix $\boldsymbol{\Psi}^p \in \mathbb{C}^{NM \times NM}$, is the channel matrix in the delay-Doppler domain with respect to the p-th backscattered signal, also referred to as cross-talk matrix [11]. Its expression is given in Section 6.1.2.

6.1.2 Cross-talk matrix

The cross-talk matrix in (6.9) is the channel matrix in the delay-Doppler domain and can be considered as a block matrix consisting of $N \times N$ submatrices, denoted by indexes $[l, l']$, each of dimension $M \times M$. Differently, the elements of each submatrix are denoted with indexes $[k, k']$. The single element of $\boldsymbol{\Psi}^p$ can be written as follows

$$\begin{aligned}\boldsymbol{\Psi}^p_{l,l'}[k,k'] = \frac{1}{NM} \sum_{n,n',m,m'} & e^{j2\pi(n'Tf_{\mathrm{D},p} - m\Delta f \tau_p - \frac{nl-n'l'}{N} + \frac{mk-m'k'}{M})} \times \\ & \times A_{g_{\mathrm{rx}},g_{\mathrm{tx}}}((n-n')T - \tau_p, (m-m')\Delta f + f_{\mathrm{D},p}).\end{aligned} \tag{6.10}$$

Given the complexity of the expression of the cross-talk matrix, to simplify its calculation, the integral appearing in the representation of the cross-ambiguity function can be approximated with a discrete summation, as

$$\begin{aligned}A_{g_{\mathrm{rx}},g_{\mathrm{tx}}}(\tau, f_{\mathrm{D}}) &= \int_0^T g_{\mathrm{tx}}(t) g^*_{\mathrm{rx}}(t-\tau) e^{-j2\pi f_{\mathrm{D}} t} dt \\ &\approx \frac{T}{M} \sum_{i=0}^{M-1} g_{\mathrm{tx}}(i\frac{T}{M}) g^*_{\mathrm{rx}}(i\frac{T}{M} - \tau) e^{-j2\pi f_{\mathrm{D}} i \frac{T}{M}}.\end{aligned} \tag{6.11}$$

Furthermore, for analytical convenience, it can be assumed that each subcarrier within the band B of the OTFS system is spaced precisely by Δf, which is verified for a large number of subcarriers M, which is a typical case. Additionally, we assume that the bandwidth expansion caused by Doppler is minimal in relation to B in order to keep the received signal bandwidth roughly equal to B, i.e., $f^{(\mathrm{ICI})}_{\mathrm{D,max}} < \Delta f$. We further hypothesize that $g_{\mathrm{tx}}(t)$

and $g_{\mathrm{rx}}(t)$ are two rectangular pulses of duration T, thus limiting, as already stated, the maximum delay $\tau_{\max}^{(\mathrm{ISI})} < T$ measurable by the JSC system. Due to these assumptions, the summation in equation (6.11), which approximates the cross-ambiguity function, can be further simplified in the following way

$$A_{g_{\mathrm{rx}},g_{\mathrm{tx}}}(\tau, f_{\mathrm{D}}) \approx \frac{1}{M} \sum_{i=0}^{M-1-k_\tau} e^{-j2\pi f_{\mathrm{D}} i \frac{T}{M}} \tag{6.12}$$

where $k_\tau \triangleq \lceil \tau/(T/M) \rceil$.

Therefore, under these considerations, the cross-ambiguity function is nonzero only at the index points $n' = n$ and $n' = n-1$, which allows to approximate the cross-talk matrix $\mathbf{\Psi}^p$ as follows [11]

$$\begin{aligned} \mathbf{\Psi}^p_{l,l'}[k,k'] \approx \frac{1}{NM} \frac{1 - e^{j2\pi(l'-l+f_{\mathrm{D},p}NT)}}{1 - e^{j2\pi \frac{(l'-l+f_{\mathrm{D},p}NT)}{N}}} \frac{1 - e^{j2\pi(k'-k+\tau_p M\Delta f)}}{1 - e^{j2\pi \frac{(k'-k+\tau_p M\Delta f)}{M}}} \times \\ \times\, e^{j2\pi f_{\mathrm{D},p} \frac{k'}{M\Delta f}} \begin{cases} 1 & if\ k' = 0, ..., (M-1-k_{\tau_p}) \quad k'_{\mathrm{ICI}} \\ e^{-j2\pi(\frac{l'}{N} + f_{\mathrm{D},p}T)} & if\ k' = (M-k_{\tau_p}), ..., (M-1) \quad k'_{\mathrm{ISI}}. \end{cases} \end{aligned} \tag{6.13}$$

6.1.3 OTFS-JSC input-output relation

A more compact input-output relation directly in the delay-Doppler domain can be derived by starting from (6.8), (6.9) and (6.13), and performing a vectorization operation on the transmitted symbol grid of elements $x[k,l]$ and on the received symbol grid of elements $y[k,l]$. This results in two $NM \times 1$ vectors, which are $\mathbf{x}$ and $\mathbf{y}$, respectively. Thus, the input-output relation can be rewritten as follows

$$\mathbf{y} = \left(\sum_{p=0}^{P-1} h'_p \mathbf{\Psi}^p \right) \mathbf{x} + \mathbf{w} \tag{6.14}$$

where $\mathbf{w} \in \mathbb{C}^{NM\times 1}$ represents the AWGN vector with mean $\mathbf{0}_{NM}$ and covariance $\mathbf{\Sigma} = \sigma_w^2 \mathbf{I}_{NM}$. Throughout this analysis, without loss of generality, a simplified single point-like target scenario is considered, i.e. $P = 1$, so the index p is dropped from now on. Furthermore, the elements of $\mathbf{x}$ are normalized to unit power, such that $\mathbb{E}\{|x[k,l]|^2\} = 1$, and the channel path-loss is ignored, i.e., $h = 1$. Therefore, the SNR related to the sensing part is defined as $\text{SNR}_{\text{rad}} = 1/\sigma_w^2$.

In this setting, (6.14) can be rewritten as

$$\mathbf{y} = h'\boldsymbol{\Psi}\mathbf{x} + \mathbf{w} \tag{6.15}$$

where, by assuming $h = 1$, the coefficient h', previously defined in Section 6.1.1 can be rewritten as $h' = e^{j2\pi f_{\text{D}}\tau}$.

6.2 Sensing Parameters Estimation with OTFS and CRLB Calculation

6.2.1 Target detection and maximum likelihood estimator

Considering the received signal in (6.15), and defining $\mathbf{s} = h'\boldsymbol{\Psi}(\tau, f_{\text{D}})\mathbf{x}$ the $NM \times 1$ vector of mean values of $\mathbf{y}$, the ML estimator for the set of unknown parameters $\boldsymbol{\theta} = (|h'|, \angle h', \tau, f_{\text{D}})$, for the considered single-target scenario, is given by

$$\hat{\boldsymbol{\theta}} = \arg \max_{\boldsymbol{\theta} \in \mathbb{R}^4} l(\mathbf{y}|\boldsymbol{\theta}, \mathbf{x}) \tag{6.16}$$

where $l(\mathbf{y}|\boldsymbol{\theta}, \mathbf{x}) = -\ln\Big(\pi^{NM}\det(\boldsymbol{\Sigma})\Big) - \frac{1}{\sigma_w^2}\|\mathbf{y} - \mathbf{s}\|^2$ is the log-likelihood function to be maximized.

Assuming τ and f_{D} as known, the estimator $\hat{h'}$ of the channel gain $h' = |h'|e^{j\angle h'}$ is given by

$$\hat{h'} = \frac{\mathbf{x}^\dagger \boldsymbol{\Psi}(\tau, f_{\text{D}})^\dagger \mathbf{y}}{\mathbf{x}^\dagger \boldsymbol{\Psi}(\tau, f_{\text{D}})^\dagger \boldsymbol{\Psi}(\tau, f_{\text{D}})\mathbf{x}}. \tag{6.17}$$

Next, by substituting (6.17) into the log-likelihood function and by neglecting the term that does not depend on parameters in $\boldsymbol{\theta}$, we obtain

$$l(\mathbf{y}|\boldsymbol{\theta}, \mathbf{x}) = -\left(|\mathbf{y}|^2 - \frac{|\mathbf{x}^\dagger \boldsymbol{\Psi}(\tau, f_{\text{D}})^\dagger \mathbf{y}|^2}{\mathbf{x}^\dagger \boldsymbol{\Psi}(\tau, f_{\text{D}})^\dagger \boldsymbol{\Psi}(\tau, f_{\text{D}})\mathbf{x}}\right) \tag{6.18}$$

Therefore, by introducing the function

$$\ell(\tau, f_{\mathrm{D}}) = \frac{|\mathbf{x}^{\dagger}\mathbf{\Psi}(\tau, f_{\mathrm{D}})^{\dagger}\mathbf{y}|^2}{\mathbf{x}^{\dagger}\mathbf{\Psi}(\tau, f_{\mathrm{D}})^{\dagger}\mathbf{\Psi}(\tau, f_{\mathrm{D}})\mathbf{x}} \tag{6.19}$$

the estimate $(\hat{\tau}, \hat{f}_{\mathrm{D}})$ of τ, f_{D}, which is directly related to the estimation of the sensing parameters (r, v), previously shown in Section 6.1, can be obtained as

$$(\hat{\tau}, \hat{f}_{\mathrm{D}}) = \arg \max_{(\tau, f_{\mathrm{D}}) \in \Gamma} \ell(\tau, f_{\mathrm{D}}) \tag{6.20}$$

where Γ is a discretized search space defined as set of delay-Doppler value pairs taken from given delay intervals $[\tau_{\min}, \tau_{\max}]$ and Doppler frequency intervals $[f_{\mathrm{D,min}}, f_{\mathrm{D,max}}]$, with steps of $\Delta\tau = 1/(M'\Delta f)$ and $\Delta f_{\mathrm{D}} = 1/(N'T)$, respectively, with $M' \geq M$ and $N' \geq N$, as follows[1]

$$\begin{aligned}\Gamma = \{(\tau, f_{\mathrm{D}}) \,|\, \tau &= \tau_{\min} : \Delta\tau : \tau_{\max}, \\ f_{\mathrm{D}} &= f_{\mathrm{D,min}} : \Delta f_{\mathrm{D}} : f_{\mathrm{D,max}}\}\end{aligned} \tag{6.21}$$

To perform the estimation of parameters related only to actual targets, a binary hypothesis test with threshold η is performed on (6.19) to distinguish noise from the useful signal, as follows

$$\ell(\tau, f_{\mathrm{D}}) \underset{\mathcal{H}_1}{\overset{\mathcal{H}_0}{\lessgtr}} \eta \tag{6.22}$$

where η is the detection threshold, $\mathcal{H}_0$ and $\mathcal{H}_1$ are the hypotheses of the considered binary test, corresponding to the absence of a target (i.e., only noise) and the presence of a target, respectively.

The target parameters estimation (range and velocity) is performed according to (6.20) each time the binary test in (6.22) selects $\mathcal{H}_1$, i.e., a target is present. Specifically, when $\ell(\hat{\tau}, \hat{f}_{\mathrm{D}})$ is greater than η, the pair $(\hat{\tau}, \hat{f}_{\mathrm{D}})$ corresponds to the estimated parameters for the detected target.

The detection threshold η can be chosen to fix the false-alarm rate (FAR) in the considered search space Γ of size $|\Gamma|$. It is easy to prove that if there

---

[1] Starting from $\Delta\tau$ and Δf_{D} the range and velocity resolutions of the system can be computed as $\Delta r = c\Delta\tau/2$ and $\Delta v = c\Delta f_{\mathrm{D}}/(2f_{\mathrm{c}})$, respectively.

is only noise at the receiver, i.e., $\mathbf{y} = \mathbf{w}$, the random amplitude assumed by $\ell(\tau, f_{\mathrm{D}})$ for each $(\tau, f_{\mathrm{D}}) \in \Gamma$ is exponentially distributed with mean value equal to σ_w^2. Thus, it follows that the threshold can be computed as

$$\eta = -\sigma_w^2 \ln P_{\mathrm{FA,point}} \tag{6.23}$$

where $P_{\mathrm{FA,point}}$ is the probability of having a false alarm, i.e., the probability that $\ell(\tau, f_{\mathrm{D}}) > \eta$ under $\mathcal{H}_0$, related to each point $(\tau, f_{\mathrm{D}}) \in \Gamma$. The relation between $P_{\mathrm{FA,point}}$ and the total FAR to be guaranteed in the whole search space Γ is given by

$$P_{\mathrm{FA,point}} = \mathrm{FAR}/|\Gamma|. \tag{6.24}$$

Looking at (6.20) it is worth noting that the channel matrix Ψ defined in (6.13) must be recomputed several times to obtain the estimate of the sensing parameters τ and f_{D}. Also, a large number of numerical operations is required to compute this matrix. For this reason, approaches to reduce the computational complexity of the estimator are very highly desirable. Having said that, in Chapter 7, an analysis of the computational complexity of the sensing system is performed and a low-complexity detector for OTFS-based sensing is proposed.

6.2.2 Cramér–Rao lower bound

In the following, the derivation of the CRLB on the estimation of the sensing parameters τ and f_{D}, considering the received signal in (6.15), is presented. As known, the CRLB on the estimation of each parameter τ, f_{D}, $|h'|$ and $\angle h'$ contained in the vector $\boldsymbol{\theta}$ is given by

$$\mathrm{var}[\hat{\theta}_i] \geq J_{ii}^{-1} \tag{6.25}$$

where $\hat{\theta}_i$ is the estimate of $\theta_i \in \boldsymbol{\theta}$, representing the i-th generic parameter contained in $\boldsymbol{\theta}$ and J_{ii}^{-1} represents the generic i-th element on the main diagonal of the inverse *Fisher* matrix.

Thus, the problem of determining the CRLB of the four parameters in $\boldsymbol{\theta}$ is reduced to computing the *Fisher* matrix, which in this specific case is

4×4, and its inversion.

The elements of the *Fisher* matrix can be defined as follows

$$J_{ij} = \mathbb{E}[H_{\theta_i} H_{\theta_j}] = -\mathbb{E}[H_{\theta_i,\theta_j}] \tag{6.26}$$

where the generic $H_{\theta_i} = \frac{d}{d\theta_i} l(\mathbf{y}|\theta, \mathbf{x})$, with $l(\mathbf{y}|\theta, \mathbf{x})$ the log-likelihood function already introduced in the Section 6.2.1.

The elements of the *Fisher* matrix for such a likelihood function are given by [90]

$$J_{ij} = \frac{2}{\sigma_w^2} \sum_{n=0}^{NM-1} \left[\frac{\partial \mu_n}{\partial \theta_i} \frac{\partial \mu_n}{\partial \theta_j} + \frac{\partial v_n}{\partial \theta_i} \frac{d v_n}{\partial \theta_j} \right] \tag{6.27}$$

where $\mu_n = \mathfrak{Re}\{s_n\}$ and $v_n = \mathfrak{Im}\{s_n\}$, by assuming s_n the n-th element of the mean value vector $\mathbf{s}$, defined in Section 6.2.1. Now, by considering the following relation

$$\mathfrak{Re}\left\{ \left(\frac{\partial s_n}{\partial \theta_i} \right)^* \left(\frac{\partial s_n}{\partial \theta_j} \right) \right\} = \frac{\partial \mu_n}{\partial \theta_i} \frac{\partial \mu_n}{\partial \theta_j} + \frac{\partial v_n}{\partial \theta_i} \frac{\partial v_n}{\partial \theta_j} \tag{6.28}$$

(6.27) can be rewritten as

$$J_{ij} = \frac{2}{\sigma_w^2} \mathfrak{Re}\left\{ \sum_{n=0}^{NM-1} \left(\frac{\partial s_n}{\partial \theta_i} \right)^* \left(\frac{\partial s_n}{\partial \theta_j} \right) \right\} \tag{6.29}$$

where s_n can be written as an element of a $M \times N$ matrix of indexes k, l, defined as

$$s[k,l] = |h'| e^{j\angle h'} \sum_{k'=0}^{M-1} \sum_{l'=0}^{N-1} \mathbf{\Psi}_{l,l'}[k,k'] x[k',l'] \tag{6.30}$$

with $k, k' = 0, ..., M-1$ and $l, l' = 0, ..., N-1$.

Hence, in order to calculate the Fisher matrix, the partial derivatives of $s[k,l]$ with respect to the four parameters in $\boldsymbol{\theta}$, must be evaluated. For the sake of clarity, the partial derivatives are listed below

$$\frac{\partial s[k,l]}{\partial \tau} = h' \sum_{k'=0}^{M-1} \sum_{l'=0}^{N-1} \frac{\partial \mathbf{\Psi}_{l,l'}[k,k']}{\partial \tau} x[k',l'] \tag{6.31}$$

$$\frac{\partial s[k,l]}{\partial f_{\mathrm{D}}} = h' \sum_{k'=0}^{M-1} \sum_{l'=0}^{N-1} \frac{\partial \boldsymbol{\Psi}_{l,l'}[k,k']}{\partial f_{\mathrm{D}}} x[k',l'] \tag{6.32}$$

$$\frac{\partial s[k,l]}{\partial |h'|} = e^{j\angle h'} \sum_{k'=0}^{M-1} \sum_{l'=0}^{N-1} \boldsymbol{\Psi}_{l,l'}[k,k'] x[k',l'] \tag{6.33}$$

$$\frac{\partial s[k,l]}{\partial \angle h'} = jh' \sum_{k'=0}^{M-1} \sum_{l'=0}^{N-1} \boldsymbol{\Psi}_{l,l'}[k,k'] x[k',l']. \tag{6.34}$$

As can be seen by looking at (6.31), (6.32), the problem of CRLB computation lastly turns into the derivation and calculation of the partial derivatives of the cross-talk matrix with respect to the parameters τ and f_{D}, whose expressions are given in (6.35) and (6.36), according to [11].

$$\begin{aligned} &\frac{\partial \boldsymbol{\Psi}_{l,l'}[k,k']}{\partial \tau} = \\ &= \frac{j2\pi\Delta f}{NM} e^{j2\pi f_{\mathrm{D}}\left(\frac{k'}{M\Delta f}\right)} \sum_{n,m} m e^{j2\pi(l'-l+f_{\mathrm{D}}NT)\frac{n}{N}} e^{-j2\pi(k'-k+\tau M\Delta f)\frac{m}{M}} \\ &\quad\times \begin{cases} 1 & if\ k' = 0, ..., (M-1-k_\tau) = k'_{\mathrm{ICI}} \\ e^{-j2\pi\left(\frac{l'}{N}+f_{\mathrm{D}}T\right)} & if\ k' = (M-k_\tau), ..., (M-1) = k'_{\mathrm{ISI}}. \end{cases} \end{aligned} \tag{6.35}$$

$$\begin{aligned} \frac{\partial \boldsymbol{\Psi}_{l,l'}[k,k']}{\partial f_{\mathrm{D}}} &= \frac{j2\pi}{NM} e^{j2\pi f_{\mathrm{D}}\left(\frac{k'}{M\Delta f}\right)} \sum_{m} e^{-j2\pi(k'-k+\tau M\Delta f)\frac{m}{M}} \\ &\times \begin{cases} g_1(l,l',k') & if\ k' = 0, ..., (M-1-k_\tau) = k'_{\mathrm{ICI}} \\ g_2(l,l',k') & if\ k' = (M-k_\tau), ..., (M-1) = k'_{\mathrm{ISI}}. \end{cases} \end{aligned} \tag{6.36}$$

with

$$\begin{aligned}
g_1(l,l',k') &= \sum_n e^{j2\pi(l'-l+f_\mathrm{D}NT)\frac{n}{N}}\big(\frac{k'}{M\Delta f}\big) + \sum_n nTe^{j2\pi(l'-l+f_\mathrm{D}NT)\frac{n}{N}} \\
g_2(l,l',k') &= e^{-j2\pi(\frac{l'}{N}+f_\mathrm{D}T)}\Big[\sum_n e^{j2\pi(l'-l+f_\mathrm{D}NT)\frac{n}{N}}\big(\frac{k'}{M\Delta f}-T\big)+ \\
&\qquad\qquad + \sum_n nTe^{j2\pi(l'-l+f_\mathrm{D}NT)\frac{n}{N}}\Big].
\end{aligned}$$

Chapter 7

A Low-Complexity Detector for OTFS-based Sensing

In order to address the problem of the high complexity of OTFS-based JSC systems introduced in Chapter 6, this chapter proposes a solution for a low-complexity detector for JSC OTFS-based systems. In particular, we first propose an efficient calculation method of the channel matrix proposed in [11], containing the information on the detection parameters, through its decomposition into four elementary, low-dimensional matrices linked with the absolute value of the *Dirichlet kernel*. Then, a priori localization of the elements of the elementary matrices containing most of the information helpful in estimating the sensing parameters is performed. Starting from that, an approximation criterion for the elementary matrices, which consists of neglecting in the computation those elements not significant for parameter estimation, leveraging properties of the *Dirichlet kernel* is given. The proposed solution is validated through numerical simulations in order to show that it allows significantly reducing the computational complexity of the ML estimator without seriously affecting its performance, measured in terms of RMSE of range and velocity estimation and probability of detection.

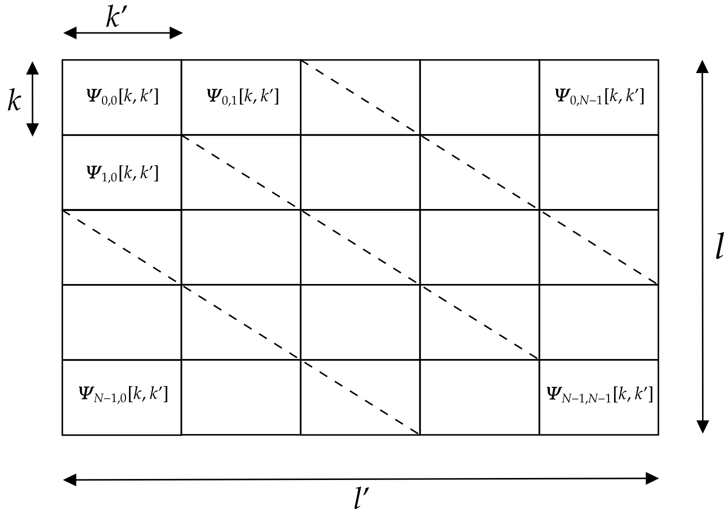

Figure 7.1: Cross-talk matrix schematic representation.

7.1 Cross-Talk Matrix Considerations

The cross-talk matrix $\boldsymbol{\Psi} \in \mathbb{C}^{NM \times NM}$ is the channel matrix in the delay-Doppler domain, containing the information about the sensing parameters. It can be defined as a block matrix since it is composed of $N \times N$ sub-matrices (denoted by indexes $[l, l']$), each of dimension $M \times M$, whose elements are indexed by the pair of indexes $[k, k']$, as conceptually shown in Fig. 7.1.

As it can be seen from (6.13), a large number of numerical operations is required to compute $\boldsymbol{\Psi}$. Moreover, according to (6.20), this matrix must be re-computed several times to obtain the estimate of the sensing parameters τ and f_D. For this reason, approaches to reduce the computational complexity of the estimator are very much desirable.

As a starting point for pursuing this objective, the following four matrices are defined

$$\boldsymbol{\mathsf{Y}}_1 \triangleq \frac{1}{NM}\frac{1-e^{j2\pi(\mathrm{l}'-\mathrm{l}+f_\mathrm{D}NT)}}{1-e^{j2\pi\frac{(\mathrm{l}'-\mathrm{l}+f_\mathrm{D}NT)}{N}}} \tag{7.1}$$

$$\boldsymbol{\mathsf{Y}}_2 \triangleq \frac{1}{NM}\frac{e^{-j2\pi(\frac{\mathrm{l}'}{N}+f_\mathrm{D}T)}-e^{j2\pi(\mathrm{l}'(1-\frac{1}{N})-\mathrm{l}+f_\mathrm{D}T(N-1))}}{1-e^{j2\pi\frac{(\mathrm{l}'-\mathrm{l}+f_\mathrm{D}NT)}{N}}} \tag{7.2}$$

$$\mathbf{X}_1 \triangleq \frac{e^{j2\pi f_{\mathrm{D}}\frac{\mathbf{k}'_1}{M\Delta f}} - e^{j2\pi(\mathbf{k}'_1(1+\frac{f_{\mathrm{D}}}{M\Delta f})-\mathbf{k}+\tau M\Delta f)}}{1-e^{j2\pi\frac{\mathbf{k}'_1-\mathbf{k}+\tau M\Delta f}{M}}} \tag{7.3}$$

$$\mathbf{X}_2 \triangleq \frac{e^{j2\pi f_{\mathrm{D}}\frac{\mathbf{k}'_2}{M\Delta f}} - e^{j2\pi(\mathbf{k}'_2(1+\frac{f_{\mathrm{D}}}{M\Delta f})-\mathbf{k}+\tau M\Delta f)}}{1-e^{j2\pi\frac{\mathbf{k}'_2-\mathbf{k}+\tau M\Delta f}{M}}} \tag{7.4}$$

where $\mathbf{Y}_1$, $\mathbf{Y}_2$ are $N \times N$ matrices, while $\mathbf{X}_1$, $\mathbf{X}_2$ have dimension $M \times (M - k_\tau)$ and $M \times k_\tau$, respectively. The two vectors $\mathbf{l} = [0, \ldots, N-1]^{\mathrm{T}}$ and $\mathbf{l}' = [0, \ldots, N-1]$ represent the row and column indexes, respectively, of $\mathbf{Y}_1$ and $\mathbf{Y}_2$. Moreover, $\mathbf{k} = [0, \ldots, M-1]^{\mathrm{T}}$ is the row indexes vector of $\mathbf{X}_i$, with $i = 1, 2$, while $\mathbf{k}'_1 = [0, \ldots, M-1-k_\tau]$ and $\mathbf{k}'_2 = [0, \ldots, k_\tau - 1]$ are the column indexes vector of $\mathbf{X}_1$ and $\mathbf{X}_2$, respectively.
From these matrices, it is now possible to calculate the cross-talk matrix through the Kronecker products between $\mathbf{Y}_i$ and $\mathbf{X}_i$ matrices with the same indexes and then sum together the resulting matrices thus obtained, as follows

$$\begin{aligned}
\boldsymbol{\Psi}_1 &= \mathbf{Y}_1 \otimes [\mathbf{X}_1, \mathbf{0}_{M\times k_\tau}] \\
\boldsymbol{\Psi}_2 &= \mathbf{Y}_2 \otimes [\mathbf{0}_{M\times (M-k_\tau)}, \mathbf{X}_2] \\
\boldsymbol{\Psi} &= \boldsymbol{\Psi}_1 + \boldsymbol{\Psi}_2.
\end{aligned} \tag{7.5}$$

To find a method for reducing the computational complexity, first, some considerations about the absolute value of $\mathbf{Y}_1$, $\mathbf{Y}_2$, $\mathbf{X}_1$, $\mathbf{X}_2$ must be made. Starting from (7.1), (7.2), (7.3) and (7.4), it is easy to prove that the absolute value is the same for each of these matrices, and it coincides with the absolute value function of the *Dirichlet kernel* [1]. This function, periodic of 2π in the $[-\pi, \pi]$ interval, can be conveniently normalized to have periodicity in $[-1/2, 1/2]$, as

$$D_R(x) = \sum_{r=-R}^{R} e^{j2\pi r x} = \frac{\sin((2R+1)\pi x)}{\sin(\pi x)} \tag{7.6}$$

With some algebraic manipulations, it can be proved that the absolute value

---

[1] Note that, in this analysis, we refer to the absolute value of a matrix as an element-wise modulus operation.

of $\mathbf{Y}_1$ and $\mathbf{Y}_2$ can be expressed as the absolute value of $D_R(x)$ apart from a normalization factor $1/(NM)$, when $R = (N-1)/2$, and by defining $x = x_{l,l'} \triangleq x'_{l,l'}/N$, with $x'_{l,l'} = l' - l + (f_\mathrm{D}NT)$, $\forall l \in \mathbf{l}$, $\forall l' \in \mathbf{l}'$. Similarly, the same expression of the absolute value can be obtained for $\mathbf{X}_1$ and $\mathbf{X}_2$ by assuming $R = (M-1)/2$ and defining $x = x_{k,k'_i} \triangleq x'_{k,k'_i}/M$, with $x'_{k,k'_i} = k'_i - k + (\tau M\Delta f)$, $\forall k \in \mathbf{k}$, $\forall k'_i \in \mathbf{k}'_\mathbf{i}$, for $i = 1, 2$. More precisely, the aforementioned relationships are

$$\begin{aligned}\left|D_{\frac{N-1}{2}}(x_{l,l'})\right| &= \left|\frac{1-e^{-j2\pi N x_{l,l'}}}{1-e^{-j2\pi x_{l,l'}}}\right| \\ &= \left|\frac{1-e^{j2\pi x'_{l,l'}}}{1-e^{j2\pi\frac{x'_{l,l'}}{N}}}\right| = |\mathbf{Y}_i[l,l']|\end{aligned} \tag{7.7}$$

$$\begin{aligned}\left|D_{\frac{M-1}{2}}(x_{k,k'_i})\right| &= \left|\frac{1-e^{-j2\pi M x_{k,k'_i}}}{1-e^{-j2\pi x_{k,k'_i}}}\right| \\ &= \left|\frac{1-e^{j2\pi x'_{k,k'_i}}}{1-e^{j2\pi\frac{x'_{k,k'_i}}{M}}}\right| = |\mathbf{X}_i[k,k'_i]|\end{aligned} \tag{7.8}$$

for $i = 1, 2$.

As it can be seen in Fig. 7.2 and 7.3, the absolute value functions in (7.7) and (7.8) are periodic of N and M in the intervals $[-N/2, N/2]$ or $[-M/2, M/2]$, respectively.
In light of all the previous considerations, the elements of $|\mathbf{Y}_1|$, $|\mathbf{Y}_2|$, $|\mathbf{X}_1|$, and $|\mathbf{X}_2|$ are nothing more than samples of the absolute value of the *Dirichlet kernel*. In particular, each of these samples falls on predictable points since, by definition, the variable x' can only take value in a specific finite discrete set depending on the related matrix indexes.

The absolute value of the *Dirichlet kernel* can be seen as a periodic function consisting of a main lobe and secondary lobes of lower peak value and decreasing as one moves away from the so-called main lobe. In particular, considering the first period that can be defined in the interval $[-N/2, N/2]$ or $[-M/2, M/2]$, depending on the matrix considered, the main lobe turns

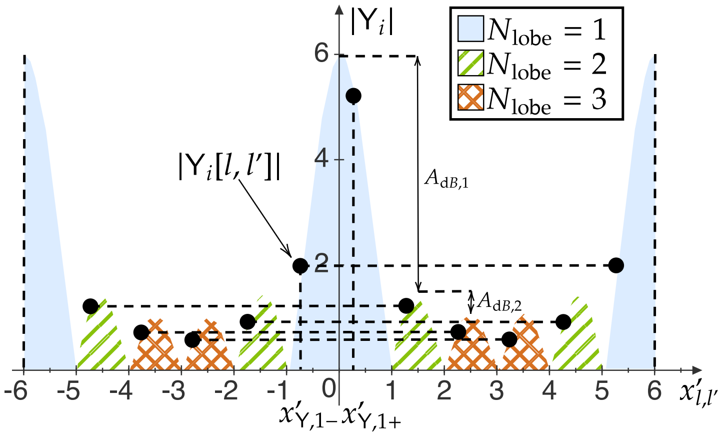

Figure 7.2: Graphical representation of the elements of matrices $|\mathbf{Y}_i[l,l']|$, with $i = 1, 2$, seen as samples of the associated function $|\mathbf{Y}_i|$, considering $x'_{\mathbf{Y},1+} \triangleq \mathrm{frac}(f_{\mathrm{D}}NT)$ and $x'_{\mathbf{Y},1-} \triangleq \mathrm{frac}(f_{\mathrm{D}}NT) - 1$. The case with $N = 6$ and $x'_{\mathbf{Y},1+} < 0.5$ is depicted.

out to be centered in the half of the period, i.e. in zero. In contrast, the secondary lobes present peaks for $x'_{l,l'}$ or x'_{k,k'_i} non-integer multiple values of $1/2$, except for $1/2$ and, as mentioned above, these peaks gradually decrease until $x'_{l,l'} = \pm N/2$ or $x'_{k,k'_i} = \pm M/2$. Since the function is periodic, the values grow again after that point until $\pm N$ or $\pm M$, respectively.
Moreover, due to the geometric property of the considered absolute value function and the fact that the indexes are integers, two samples fall into the main lobe centered at zero, namely in $x'_{l,l'} = x'_{\mathbf{Y},1+} \triangleq \mathrm{frac}(f_{\mathrm{D}}NT)$ and in $x'_{l,l'} = x'_{\mathbf{Y},1-} \triangleq \mathrm{frac}(f_{\mathrm{D}}NT) - 1$, for the $|\mathbf{Y}_i|$ matrices, or in $x'_{k,k'_i} = x'_{\mathbf{X},1+} \triangleq \mathrm{frac}(\tau M\Delta f)$ and in $x'_{k,k'_i} = x'_{\mathbf{X},1-} \triangleq \mathrm{frac}(\tau M\Delta f) - 1$, for the $|\mathbf{X}_i|$ matrices, with $i = 1, 2$. Contrariwise, in each secondary lobe only a single sample falls at multiple integers of $x'_{\mathbf{Y},1+}$ or $x'_{\mathbf{X},1+}$ in the positive x' axis and of $x'_{\mathbf{Y},1-}$ or $x'_{\mathbf{X},1-}$ in the negative one, respectively. Thus, it is worth noting that the elements of the four matrices can be seen as periodic samples of the function taken asymmetrically with respect to the y-axis.

Two special cases can be identified: one for $x'_{\mathbf{Y},1+} = 0$ or $x'_{\mathbf{X},1+} = 0$ and the other one for $x'_{\mathbf{Y},1+} = 0.5$ or $x'_{\mathbf{X},1+} = 0.5$. The former determines a discontinuity in the *Dirichlet kernel* absolute value function at the considered x' value, so that only one sample, obtained by applying *de l'Hôpital*'s theo-

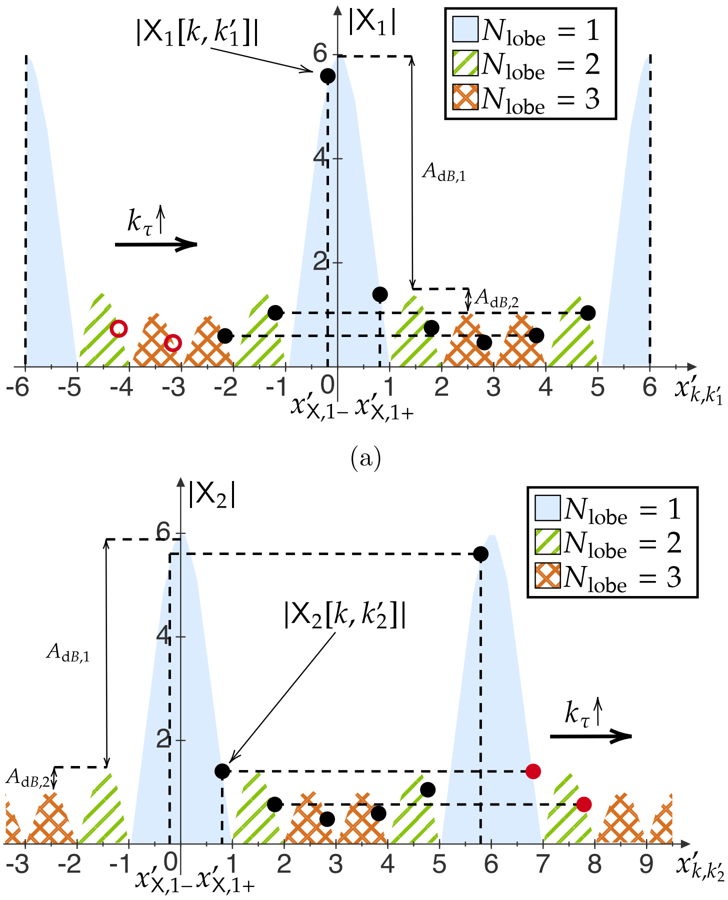

(a)

(b)

Figure 7.3: Graphical representation of the elements of the matrices $|\mathbf{X}_1[k,k_1']|$ (a) and $|\mathbf{X}_2[k,k_2']|$ (b), seen as samples of the associated functions $|\mathbf{X}_1|$ and $|\mathbf{X}_2|$, respectively, considering $x'_{\mathbf{X},1+} \triangleq \text{frac}(\tau M \Delta f)$ and $x'_{\mathbf{X},1-} \triangleq \text{frac}(\tau M \Delta f) - 1$. The case with $M = 6$ and $x'_{\mathbf{X},1+} > 0.5$ is depicted. In red are represented the samples removed from $|\mathbf{X}_1|$ (red unfilled circle) and added in $|\mathbf{X}_2|$ (red filled circle) when switching from the case with $k_\tau = 1$ to the one with $k_\tau = 3$.

rem, falls on the main lobe, precisely on its peak, while no samples fall on the secondary ones since they are located in the notches (or zeros) of the function. Differently, the latter produces a symmetrical situation in which the two samples on the main lobe assume the same value, while those on the secondary lobes are located at the corresponding peaks of the function.

7.2 Cross-Talk Matrix Approximation

In this section, the analysis performed for the approximation of the cross-talk matrix in (6.13) is presented.

By analyzing this matrix, it is possible to observe that it is nothing more than a quasi-band matrix since it has only a few elements clustered in bands that have a value in modulus that is not negligible. Moreover, as it will be shown in Section 7.5, the elements with higher modulus seem to contain most of the information about sensing parameters. Having said that, one way to reduce the computational complexity might be to set the matrix elements with modulus values below a chosen threshold to zero and then treat this matrix as a sparse matrix. However, given the high dimensionality of the cross-talk matrix and the resulting large number of entries, this approximation strategy would be inefficient from an implementation point of view, since it would require first computing the entire matrix and then setting some of its elements to zero.

One possible solution to address this problem is not to directly approximate the cross-talk matrix but to approximate the four matrices $|\mathbf{Y}_1|$, $|\mathbf{Y}_2|$, $|\mathbf{X}_1|$ and $|\mathbf{X}_2|$ introduced in Section 7.1, which have a reduced dimensionality. In particular, it is possible to select a threshold on each of these matrices, setting it according to the element that falls on one of the lobes of the corresponding *Dirichlet kernel* absolute value function, within one of its periods, as shown in Fig. 7.2 and 7.3. These lobes are identified by means of the variable N_{lobe}, with $N_{\text{lobe}} \in [1, \lceil N/2 \rceil]$ for $\mathbf{Y}_i$ functions, and $N_{\text{lobe}} \in [1, \lceil M/2 \rceil]$ for $\mathbf{X}_i$ functions, with $i = 1, 2$.

In particular, $N_{\text{lobe}} = 1$ denotes the main lobe, while values of N_{lobe} greater than one are used to identify the secondary lobes that are progressively further away from the main lobe, either in the positive or negative x' axis, within a generic period of the considered function. The above approach is motivated by the fact that between the samples on the main lobe and those on one of the secondary lobes, there is a large difference in amplitude, increasing as we move away from the main lobe. For this reason, it can be observed that the more the threshold is set to the sample that falls in a secondary lobe far away from the main lobe within the function period, the lower the threshold value becomes, and thus the smaller the number of elements of the matrix that are neglected in the approximation, and vice-versa.

Going into more detail, it can be observed that the absolute value matrices $|\mathbf{Y}_i|$ and $|\mathbf{X}_i|$, with $i = 1, 2$, have a well-defined band structure consisting of circularly shifted diagonals. Each of these diagonals is composed of equal elements, whose values are specific samples of the corresponding absolute value function, as stated in Section 7.1. The values associated with different diagonals become progressively smaller as one moves away from the main diagonal, which corresponds to the main lobe of the related absolute value function. Furthermore, each diagonal is circularly shifted by a certain factor that depends on the sensing parameters, as will be explained later. Thus, it turns out to be possible to approximate such matrices by band matrices with fewer non-zero diagonals.

One way to perform this approximation technique is to use appropriate matrices that act as masks, having ones where the matrix value must be calculated and zeros otherwise. In particular, these mask matrices are obtained from an identity matrix, by adding to it and then properly circularly shifting a number of super- and sub-diagonals equal to $\lfloor N_{\text{diag}}/2 \rfloor$, where N_{diag} is the number of non-zero diagonals in the mask matrices, given by

$$N_{\text{diag}} = 2N_{\text{lobe}} - 1, \text{ with } N_{\text{lobe}} \in \mathbb{Z}^{+}. \tag{7.9}$$

The equality in (7.9) is justified if we consider setting the threshold in correspondence of the element of the four matrices $|\mathbf{Y}_1|$, $|\mathbf{Y}_2|$, $|\mathbf{X}_1|$ and $|\mathbf{X}_2|$, associated with the chosen value of N_{lobe}. Actually, due to the asymmetry of the problem, for a given value of N_{lobe}, there are always two associated elements with different values, as can be seen in Fig. 7.2 and 7.3. However, the equality in (7.9) is still verified if one of the two that is greater in modulus is considered.

As already mentioned, the mask matrices actually turn out to be shifted in a manner dependent on the value of delay τ and Doppler shift f_{D}. In particular, the masks related to $|\mathbf{Y}_1|$ and $|\mathbf{Y}_2|$ turn out to be circularly shifted to the left by $l_{f_{\text{D}}} \triangleq \lceil f_{\text{D}} N T \rceil$ positions, while those associated with $|\mathbf{X}_1|$ and $|\mathbf{X}_2|$ are obtained starting from $M \times M$ mask matrices, by circularly shifting them leftward and downward, respectively, of $k_\tau - 1$ positions.

Nevertheless, a particular case must be considered. In fact, as previously stated in Section 7.1, for values of τ and f_D such that $\mathrm{frac}(\tau M \Delta f) = 0$ and $\mathrm{frac}(f_\mathrm{D} N T) = 0$, respectively, the elements of the absolute value matrices are samples that fall, one on the peak of the main lobe and the rest on the notches of the associated function. All the elements that fall on the notches can be neglected while the one on the peak of the main lobe can be evaluated through *de l'Hôpital*'s theorem due to a discontinuous condition, as stated in Section 7.1. In such a scenario, the matrices can be approximated as diagonal matrices, each with the corresponding sample at the peak of the main lobe as its value. Again, the resulting mask matrices are shifted by an amount related to delay and Doppler, but this time not circularly and horizontally, but downward by a number of positions equal to k_τ and l_{f_D}, respectively, depending on whether we consider the $|\mathbf{X}_i|$ or $|\mathbf{Y}_i|$ matrices.

7.3 Low-Complexity ML Implementation

To determine the pair $(\hat{\tau}, \hat{f}_\mathrm{D})$ that maximizes (6.20), which represents the parameters estimate, it is essential to compute the expression in (6.20) for multiple (τ, f_D) pair. This evaluation is performed within specified search ranges for both delay and Doppler, using a predetermined step size, as explained in Section 6.2.1. However, this operation can be computationally expensive, especially when dealing with large delay-Doppler evaluation ranges. To address this, a low-complexity algorithm for implementing the ML estimator, presented in Section 6.2.1, is provided. This method is based on the approximated ML sensing parameter estimation scheme described in [11].

The goal is to dynamically change the search interval for the values of τ and f_D by starting with a wide discretization step and gradually narrowing it to the values of the sensing parameters estimated in the previous step. This is achieved while maintaining a fixed number of τ and f_D values evaluated within the new search interval. Consequently, the algorithm maintains low complexity while repeatedly and dynamically achieving a high resolution in the search.

Specifically, in this approach, the ML estimator no longer explores all possible combinations of delay and Doppler points within a given wide range of values. Instead, it proceeds iteratively by tightening the search range around the point (τ,f_D) estimated in the previous iteration, i.e. ($\hat{\tau}$,$\hat{f}_\mathrm{D}$), until it converges to a value that remains approximately constant, with minor fluctuations, for a user-defined number of cycles. This flexible approach enables an effective balance between algorithmic complexity and resolution, offering improved efficiency in parameter estimation.

The considered low-complexity algorithm is structured as follows, where n^it denotes the index associated with the current iteration of the algorithm, T_r represents the threshold value used to determine when the change in the estimate of either sensing parameter between two consecutive iterations becomes negligible, and $N^\mathrm{it,max}$ is the maximum number of consecutive iterations in which the change in the estimated values remains below the specified threshold:

Initialization: $n^\mathrm{it} = 0$:

- fixing $\hat{h}'^{n^\mathrm{it}=0} = 0$
- we take K equispaced points (where K can take different values in the case of delay or Doppler) with step $1/(M\Delta f)$ and $1/(NT)$ in the search intervals related to delay and Doppler, respectively, as chosen by the user, i.e. $\left[\tau_\mathrm{min}^{n^\mathrm{it}=0},\tau_\mathrm{max}^{n^\mathrm{it}=0}\right]$ and $\left[f_\mathrm{D,min}^{n^\mathrm{it}=0},f_\mathrm{D,max}^{n^\mathrm{it}=0}\right]$. In this way, the following vectors of K elements are to be formed, respectively
    1. $\boldsymbol{\tau}^{n^\mathrm{it}=0} = \left\{\tau_1^0, ..., \tau_K^0\right\}$
       with $\tau_1^0 = \tau_\mathrm{min}^0$ and $\tau_K^0 = \tau_\mathrm{max}^0$
    2. $\boldsymbol{f}_\mathrm{D}^{n^\mathrm{it}=0} = \left\{f_\mathrm{D,1}^0, ..., f_{\mathrm{D},K}^0\right\}$
       with $f_\mathrm{D,1}^0 = f_\mathrm{D,min}^0$ and $f_{\mathrm{D},K}^0 = f_\mathrm{D,max}^0$

For $n^\mathrm{it} = 1, ..., N^\mathrm{it,max}$ **or**
$\left(\left|\hat{\tau}^{n^\mathrm{it}} - \hat{\tau}^{n^\mathrm{it}-1}\right|\right.$ **and** $\left.\left|\hat{f}_\mathrm{D}^{n^\mathrm{it}} - \hat{f}_\mathrm{D}^{n^\mathrm{it}-1}\right|\right) < T_\mathrm{r}$**, do**:

- *Delay and Doppler estimation update*:

$$\left(\hat{\tau}^{n^\mathrm{it}}, \hat{f}_\mathrm{D}^{n^\mathrm{it}}\right) = \underset{(\tau,f_\mathrm{D})\in\left(\boldsymbol{\tau}^{n^\mathrm{it}},\boldsymbol{f}_\mathrm{D}^{n^\mathrm{it}}\right)}{\arg\max} \frac{\left|\mathbf{x}^\dagger\boldsymbol{\Psi}^\dagger(\tau, f_\mathrm{D})\mathbf{y}\right|^2}{\mathbf{x}^\dagger\boldsymbol{\Psi}^\dagger(\tau, f_\mathrm{D})\boldsymbol{\Psi}(\tau, f_\mathrm{D})\mathbf{x}}$$

- *Channel complex gain estimate update*:

$$\hat{h}'^{n^{\mathrm{it}}} = \frac{\mathbf{x}^{\dagger}\boldsymbol{\Psi}^{\dagger}\big(\hat{\tau}^{n^{\mathrm{it}}}, \hat{f}_{\mathrm{D}}^{n^{\mathrm{it}}}\big)\mathbf{y}}{\mathbf{x}^{\dagger}\boldsymbol{\Psi}^{\dagger}\big(\hat{\tau}^{n^{\mathrm{it}}}, \hat{f}_{\mathrm{D}}^{n^{\mathrm{it}}}\big)\boldsymbol{\Psi}\big(\hat{\tau}^{n^{\mathrm{it}}}, \hat{f}_{\mathrm{D}}^{n^{\mathrm{it}}}\big)\mathbf{x}}$$

- *Updating and narrowing of the search intervals*:
  Assuming that $\hat{i}$ and $\hat{j}$ represent the indexes associated with the elements of the vectors $\boldsymbol{\tau}^{n^{\mathrm{it}}}$ and $\boldsymbol{f}_{\mathrm{D}}^{n^{\mathrm{it}}}$, respectively, corresponding to the estimated values at step n^{it} for delay $\hat{\tau}$ and Doppler $\hat{f}_{\mathrm{D}}$, then it arises

  - $\tau_{\mathrm{min}}^{n^{\mathrm{it}}+1} = \tau_{\hat{i}-1}^{n^{\mathrm{it}}}$ and $\tau_{\mathrm{max}}^{n^{\mathrm{it}}+1} = \tau_{\hat{i}+1}^{n^{\mathrm{it}}}$
  - $f_{\mathrm{D,min}}^{n^{\mathrm{it}}+1} = f_{\mathrm{D}\hat{j}-1}^{n^{\mathrm{it}}}$ and $f_{\mathrm{D,max}}^{n^{\mathrm{it}}+1} = f_{\mathrm{D}\hat{j}+1}^{n^{\mathrm{it}}}$

  If $\hat{i}$ or $\hat{j}$ are equal to 1 or K, then we have

  - case $\hat{i} = 1$ or $\hat{j} = 1$, then:
    $\tau_{\mathrm{min}}^{n^{\mathrm{it}}+1} = \tau_{\hat{i}}^{n^{\mathrm{it}}}$ and $\tau_{\mathrm{max}}^{n^{\mathrm{it}}+1} = \tau_{\hat{i}+2}^{n^{\mathrm{it}}}$
    $f_{\mathrm{D,min}}^{n^{\mathrm{it}}+1} = f_{D,\hat{j}}^{n^{\mathrm{it}}}$ and $f_{\mathrm{D,max}}^{n^{\mathrm{it}}+1} = f_{D,\hat{j}+2}^{n^{\mathrm{it}}}$
  - case $\hat{i} = K$ or $\hat{j} = K$, then:
    $\tau_{\mathrm{min}}^{n^{\mathrm{it}}+1} = \tau_{\hat{i}-2}^{n^{\mathrm{it}}}$ and $\tau_{\mathrm{max}}^{n^{\mathrm{it}}+1} = \tau_{\hat{i}}^{n^{\mathrm{it}}}$
    $f_{\mathrm{D,min}}^{n^{\mathrm{it}}+1} = f_{D,\hat{j}-2}^{n^{\mathrm{it}}}$ and $f_{\mathrm{D,max}}^{n^{\mathrm{it}}+1} = f_{D,\hat{j}}^{n^{\mathrm{it}}}$

  Finally, in the subsequent iteration of the algorithm, denoted as $\big(n^{\mathrm{it}} + 1\big)$, a new set of K equispaced values is selected within the updated delay and Doppler search intervals $\big[\tau_{\mathrm{min}}^{n^{\mathrm{it}}+1}, \tau_{\mathrm{max}}^{n^{\mathrm{it}}+1}\big]$ and $\big[f_{\mathrm{D,min}}^{n^{\mathrm{it}}+1}, f_{\mathrm{D,max}}^{n^{\mathrm{it}}+1}\big]$. This set of values comprises the following elements

  - $\boldsymbol{\tau}^{n^{\mathrm{it}}+1} = \big\{\tau_1^{n^{\mathrm{it}}+1}, \ldots, \tau_K^{n^{\mathrm{it}}+1}\big\}$,
    with $\tau_1^{n^{\mathrm{it}}+1} = \tau_{\mathrm{min}}^{n^{\mathrm{it}}+1}$ and $\tau_K^{n^{\mathrm{it}}+1} = \tau_{\mathrm{max}}^{n^{\mathrm{it}}+1}$
  - $\boldsymbol{f}_{\mathrm{D}}^{n^{\mathrm{it}}+1} = \big\{f_{\mathrm{D}1}^{n^{\mathrm{it}}+1}, \ldots, f_{\mathrm{D}K}^{n^{\mathrm{it}}+1}\big\}$,
    with $f_{\mathrm{D}1}^{n^{\mathrm{it}}+1} = f_{\mathrm{D,min}}^{n^{\mathrm{it}}+1}$ and $f_{\mathrm{D}K}^{n^{\mathrm{it}}+1} = f_{\mathrm{D,max}}^{n^{\mathrm{it}}+1}$.

An example of the behavior of the considered low-complexity implementation of the ML estimator is shown through the range-velocity heatmaps in Fig. 7.4. In particular, three iterations of the algorithm are shown. The first one is related to the initialization where a course estimation is performed by considering huge ranges of distance and velocity. Then, as explained earlier, the estimation is improved with each iteration by narrowing the search range around the previously estimated value with increasing resolution.

7.4 Computational Complexity Definition

The definition of computational complexity used in this dissertation is presented in this section.

First, the concept of elementary operation is introduced. Then, the computational complexity is estimated based on the estimation of the number of elementary operations required.

For the considered problem, i.e. the estimation of range and velocity of targets by using the ML algorithm in (6.20), the most expensive operation in terms of computational resources is by far the calculation of the cross-talk matrix $\boldsymbol{\Psi}$.

Therefore, a good estimate of the computational complexity of the system can be obtained as the number of elementary operations needed to compute this matrix. In particular, the complexity estimate is given first for the case without any approximation, hereinafter referred to as the full case, and then for the approximated case. This allows having a metric for comparing the two scenarios, as will be shown in Section 7.5.

In this analysis, the real sum is considered as an elementary operation. Moreover, according to [91], the real multiplication can be seen as corresponding to q times a real sum in terms of computational effort, where q is the equivalence factor between real sum and multiplication. Therefore, since a complex multiplication corresponds to 4 real multiplications and 2 real sums, it follows that it can be considered as a number $2(2q+1)$ of real sums. Differently, the complex sum corresponds to only 2 real sums.

Without loss of generality, we assume that both the sum between two zero elements, i.e. $0+0$, and the product between zero and a generic element $z \in \mathbb{C}$ different from zero, i.e. $0 \times z$, generate a negligible computational cost and are therefore almost negligible for the complexity estimation. For this reason, they are only taken into account by a parameter ϵ whose value depends mainly on the hardware (HW) under consideration and is defined

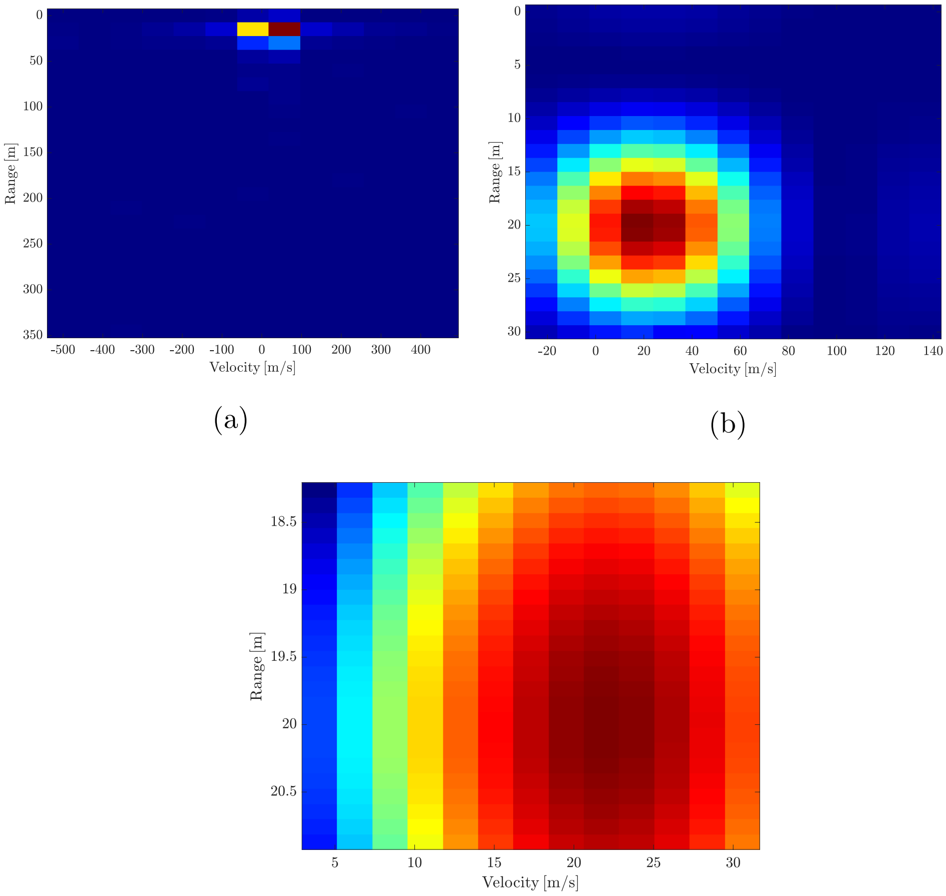

(a)

(b)

(c)

Figure 7.4: Range-velocity heatmaps obtained by varying search intervals and steps for three iterations of the algorithm. (a) first iteration: distance and velocity resolution equal to 15 m and 79.6 m/s, respectively. (b) second iteration: distance and velocity resolution equal to 1.3 m and 13.3 m/s, respectively. (c) third iteration: distance and velocity resolution equal to 0.12 m and 2.2 m/s, respectively.

as follows

$$\begin{cases} 0+0 \\ 0 \times z \end{cases} = \epsilon(\text{HW})\,\text{operations} \approx 0\,\text{operations}. \tag{7.10}$$

The calculation of the cross-talk matrix $\boldsymbol{\Psi}$ in the full case involves a total computational cost $C_{\boldsymbol{\Psi}}$, defined as the number of real sums needed to calculate the cross-talk matrix, given by

$$C_{\boldsymbol{\Psi}} = C_{\boldsymbol{\Psi}_1} + C_{\boldsymbol{\Psi}_2} + C_{\boldsymbol{\Psi}_1+\boldsymbol{\Psi}_2} \tag{7.11}$$

where $C_{\boldsymbol{\Psi}_1} = 2N^2M(M-k_\tau)(2q+1)$ and $C_{\boldsymbol{\Psi}_2} = 2N^2Mk_\tau(2q+1)$ are the computational costs to compute $\boldsymbol{\Psi}_1$ and $\boldsymbol{\Psi}_2$, respectively, while $C_{\boldsymbol{\Psi}_1+\boldsymbol{\Psi}_2} = 2(NM)^2$ is the computational cost to calculate the element-wise sum matrix between $\boldsymbol{\Psi}_1$ and $\boldsymbol{\Psi}_2$. Therefore, the computational cost $C_{\boldsymbol{\Psi}}$ is given by

$$C_{\boldsymbol{\Psi}} = 4(NM)^2(q+1). \tag{7.12}$$

Differently, the computational cost $C_{\boldsymbol{\Psi}_{\text{ap}}}$ for the calculation of the approximate cross-talk $\boldsymbol{\Psi}_{\text{ap}}$ is much lower and it depends on the variable N_{diag}, and thus on N_{lobe}, introduced in (7.9). In particular, the overall computational cost in the approximated case can be expressed as

$$\begin{aligned} C_{\boldsymbol{\Psi}_{\text{ap}}}(N_{\text{lobe}}, \text{HW}) &= C_{\boldsymbol{\Psi}_{1,\text{ap}}}(N_{\text{lobe}}) + C_{\boldsymbol{\Psi}_{2,\text{ap}}}(N_{\text{lobe}}) \\ &+ C_{\boldsymbol{\Psi}_{1,\text{ap}}+\boldsymbol{\Psi}_{2,\text{ap}}}(N_{\text{lobe}}) \\ &+ C_\epsilon(\text{HW}) \end{aligned} \tag{7.13}$$

where $C_{\boldsymbol{\Psi}_{1,\text{ap}}} = 2N(2N_{\text{lobe}}-1)^2(M-k_\tau)(2q+1)$, $C_{\boldsymbol{\Psi}_{2,\text{ap}}} = 2Nk_\tau(2N_{\text{lobe}}-1)^2(2q+1)$ and $C_{\boldsymbol{\Psi}_{1,\text{ap}}+\boldsymbol{\Psi}_{2,\text{ap}}} = 2NM(2N_{\text{lobe}}-1)^2$ are the computational costs in the approximate case, while C_ϵ represents the negligible computational cost associated with the aforementioned zero operations. Starting from (7.13) and replacing the expressions for the computational cost given above, the total computational cost in the approximate case can be obtained as

$$\begin{aligned} C_{\boldsymbol{\Psi}_{\text{ap}}}(N_{\text{lobe}}, \text{HW}) &= 4NM(2N_{\text{lobe}}-1)^2(q+1) \\ &+ C_\epsilon(\text{HW}). \end{aligned} \tag{7.14}$$

Finally, in order to analyze the gain obtained in terms of reduction of the number of operations between the approximate case and the full case, a gain factor $G_{\text{comp}}(N_{\text{lobe}}, \text{HW})$ is introduced. In particular, this can be seen as a decimation factor on operations due to the proposed approximation criterion and is defined as

$$\begin{aligned} G_{\text{comp}}(N_{\text{lobe}}, \text{HW}) &= \frac{C_{\boldsymbol{\Psi}}}{C_{\boldsymbol{\Psi}_{\text{ap}}}(N_{\text{lobe}}, \text{HW})} \\ &= \frac{NM}{(2N_{\text{lobe}} - 1)^2 + C_{\epsilon}(\text{HW})}. \end{aligned} \tag{7.15}$$

7.5 Validation of the Proposed Approximation Technique

Numerical simulations are performed to evaluate the effectiveness of the method proposed in Section 7.2 for the approximation of the cross-talk matrix $\boldsymbol{\Psi}$. The analysis is carried out considering system parameters according to the automotive standard IEEE 802.11p, as summarized in Table 7.1. In addition, a 16-QAM constellation with symbols normalized to unitary mean power, and a scenario as the one described in Section 6.1 are considered.

Two different analysis are conducted: 1) a study of the system computational complexity by means of the metrics introduced in Section 7.4; 2) an analysis of the impact of the approximation technique introduced in Section 7.2 on the sensing performance. The latter is done by means of RMSE and detection probability curves, comparing the estimation and detection performance of the system for different levels of approximation (i.e., different values of the variable N_{lobe}) and also without any approximation.

7.5.1 Computation complexity analysis

The computational complexity analysis of the ML algorithm in (6.20), which is utilized for estimating the sensing parameters τ (or r) and f_D (or v), is conducted by employing the metrics presented in Section 7.4.

This analysis consists of comparing the full case with the approximate case and considering a single computation of the cross-talk matrix. Specifically,

Table 7.1: Simulation Parameters

IEEE 802.11p [92]		Target / Radar Parameters	
f_c [GHz]	5.89	Target dist. r [m]	20
B [MHz]	10	Target vel. v [m/s]	22.22
Active subcarriers M	64	r^0_{min} [m]	0
OTFS symbols per frame N	50	r^0_{max} [m]	350
$\Delta f = B/M$ [kHz]	156.25	v^0_{min} [m/s]	-500
$T = 1/\Delta f$ [μs]	6.4	v^0_{max} [m/s]	500

the focus is on highlighting the decrease in the number of operations needed to calculate the cross-talk matrix as the level of approximation increases.

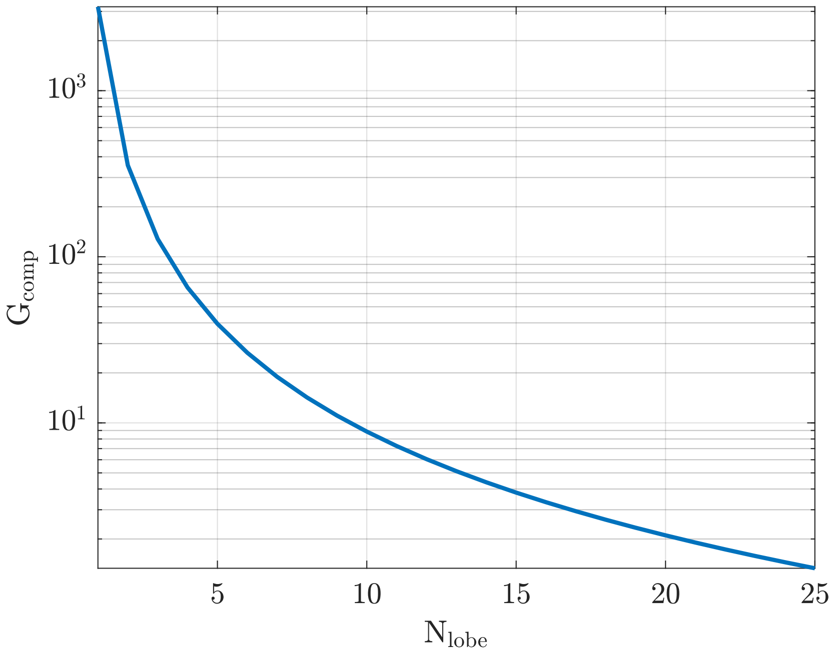

Figure 7.5: Gain factor G_{comp} as a function of the variable N_{lobe}.

For this purpose, in Fig. 7.5 the decrease of the gain factor G_{comp} as the variable N_{lobe} increases is shown. As expected, it can be seen that increasing the value of N_{lobe}, corresponding to a larger number of elements included in the matrix approximation, leads to decreasing benefits in terms of reducing

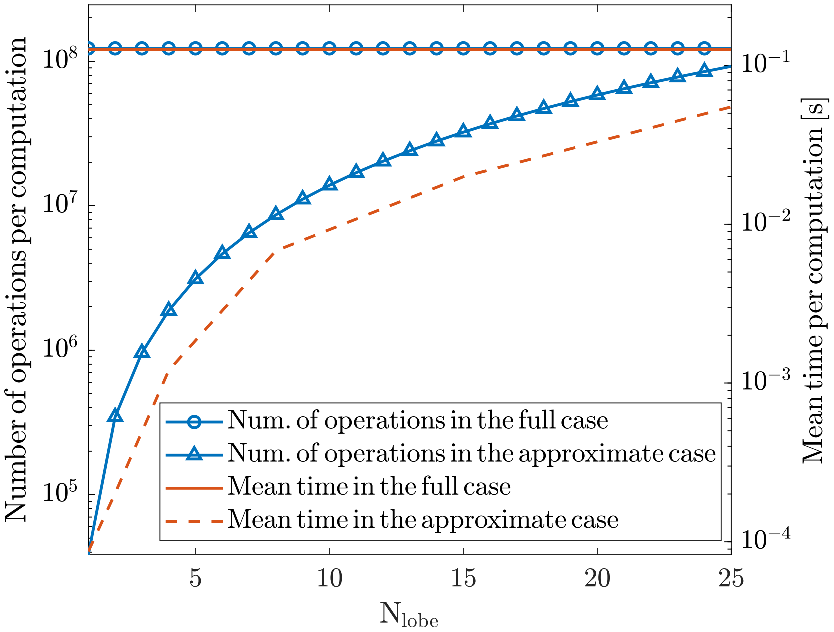

Figure 7.6: $C_{\boldsymbol{\Psi}}$ and $C_{\boldsymbol{\Psi}_{\text{ap}}}$ (left y-axis) and the associate average time curves (right y-axis) vs N_{lobe}, by assuming $N = 50$, $M = 64$, and $q = 2$.

the total number of elementary operations compared to the scenario without any approximation. Notably, for N_{lobe} values greater than approximately $\min(\lceil N/2 \rceil, \lceil M/2 \rceil)$, that is 25 in the considered case, the resulting gain approaches a value of 1, indicating that there is no discernible benefit in adopting the approximation, as expected from what has been explained in Section 7.2.

Fig. 7.6 shows on the left y-axis the curves of the computational costs $C_{\boldsymbol{\Psi}}$ and $C_{\boldsymbol{\Psi}_{\text{ap}}}$ as functions of the variable N_{lobe}. These curves are compared, on the right y-axis, with the corresponding curves of the cross-talk matrix computation mean times, obtained by simulating the system in MATLAB.

It can be noticed that the full case exhibits a convergence of the cost and average time curves at different scales, while in the approximate case, a noticeable offset between these curves is observed. This discrepancy is a result of omitting the term C_{ϵ}, as defined in equation (7.13), from the computation of the number of operations required for constructing the cross-talk matrix. Furthermore, it can be observed the gain on computational complexity as N_{lobe} varies. In particular, it can be seen that for extremely low values of N_{lobe}, where the system works rather well (e.g., for $N_{\text{lobe}} > 1$, as it will be shown in Section 7.5.2), the computational complexity gain is notably high. For example, a difference of 3 orders of magnitude in the number of operations and 2 orders of magnitude in the average times between the full case and the approximate case is present when $N_{\text{lobe}} = 2$.

7.5.2 Estimation root-mean-square error analysis

An analysis of the performance of sensing parameters estimation is carried out in order to highlight the impact of the proposed cross-talk matrix approximation on it. This analysis is done by means of RMSE curves related to the estimation of range and velocity, as a function of SNR, obtained for several values of the variable N_{lobe}, as shown in Fig. 7.7. As can be observed, these curves are also compared with the performance of the full case scenario and with the square root of the CRLBs derived in Section 6.2.2.

As mentioned in Section 6.1.3, the radar SNR is defined as

$$\text{SNR}_{\text{rad}} = \frac{\mathbb{E}\{|x[k,l]|^2\}}{P_{\text{n}}} = \frac{1}{\sigma_w^2} \tag{7.16}$$

The RMSE is defined as in (3.4), with $N_{\text{MC}} = 1000$.
Upon analyzing Fig. 7.7a and 7.7b, which show the RMSE in the estimation of range and velocity respectively, it can be observed that the JSC OTFS-based system in the full case exhibits good estimation performance up to SNR $= -17$ dB, with the RMSE being in close proximity to the theoretical bound, for both range and velocity.

For what concerns the performance related to the proposed approximation technique, it can be noticed that for high SNR, as the value of the variable N_{lobe} increases, and thus the number of considered elements of the cross-talk matrix, the RMSE curves tend to coincide with those related to the full case. Moreover, even for relatively low values of the variable N_{lobe}, such as $N_{\text{lobe}} = 2$, the RMSE curves in the approximate case almost match those of the non-approximate case, showing only a marginal degradation with a difference of about 1 cm in range and less than 1 m/s in velocity in the high-SNR regime. Additionally, it is worth noting that for $N_{\text{lobe}} \geq 5$, the performance becomes nearly identical to that of the full case. Based on the obtained results, it can be concluded that the information concerning the sensing parameters within the cross-talk matrix is predominantly concentrated in a few elements, specifically those with larger magnitudes. As a result, the proposed approximation criterion in this study is both justified and effective in reducing the complexity of an JSC OTFS-based system without significantly compromising the accuracy of sensing parameter estimation when compared to the full case.

Consequently, the choice of an appropriate value for N_{lobe} should be determined by the specific application's requirements, taking into consideration the desired level of estimation accuracy and system complexity. This involves finding a suitable trade-off between lower complexity, which improves with lower N_{lobe}, and higher estimation accuracy, which improves with higher N_{lobe}.

In addition to the RMSE analysis above, the impact of the proposed approximation method on the system performance in terms of detection probability is studied and the obtained results are shown in Fig. 7.8. These curves are obtained by using the hypothesis test in (6.22) and setting η in order to guarantee FAR $= 10^{-2}$ on the considered search space Γ. In particular, with reference to the ML estimator implementation introduced in Section 7.3, the detection is performed on the first search space Γ^0, whose $[\tau^0_{\text{min}}, \tau^0_{\text{max}}]$, and $[f^0_{\text{D,min}}, f^0_{\text{D,max}}]$ intervals are related to the corresponding range and velocity values in Table 7.1. It is important to note that when $N_{\text{lobe}} \geq 2$, the considered approximation technique has no discernible effect on the system performance in terms of detection probability with respect to the full case. This analysis further confirms the effectiveness of the proposed method. The case with $N_{\text{lobe}} = 1$ was neglected because the RMSE analysis showed that the estimator does not work properly in this case.

7.6 Remarks

In this chapter, a novel approach has been introduced to significantly reduce the computational complexity (related to sensing operations) of the OTFS-based JSC system, by focusing on the computation of the channel matrix.

The proposed method is based on the definition of four low-dimensional matrices used to compute the channel matrix through straightforward algebraic manipulations. An analysis found on the *Dirichlet kernel* absolute value function has been performed to identify a-priori the most informative elements in each of these derived matrices.

Based on this, an analytical criterion, independent of the system parameters, has been proposed to approximate those matrices. Through numerical simulations it has been shown that using this criterion, a high degree of approximation can be achieved, resulting in efficient and low-complexity computation of the channel matrix. In particular, the computational effort is reduced by up to 3 orders of magnitude considering a single computation of the matrix, without significantly compromising the sensing performance. This advance holds great promise for improving the practical implementation of the OTFS-based JSC system, making it more accessible to resource-constrained devices and real-time sensing and tracking applications.

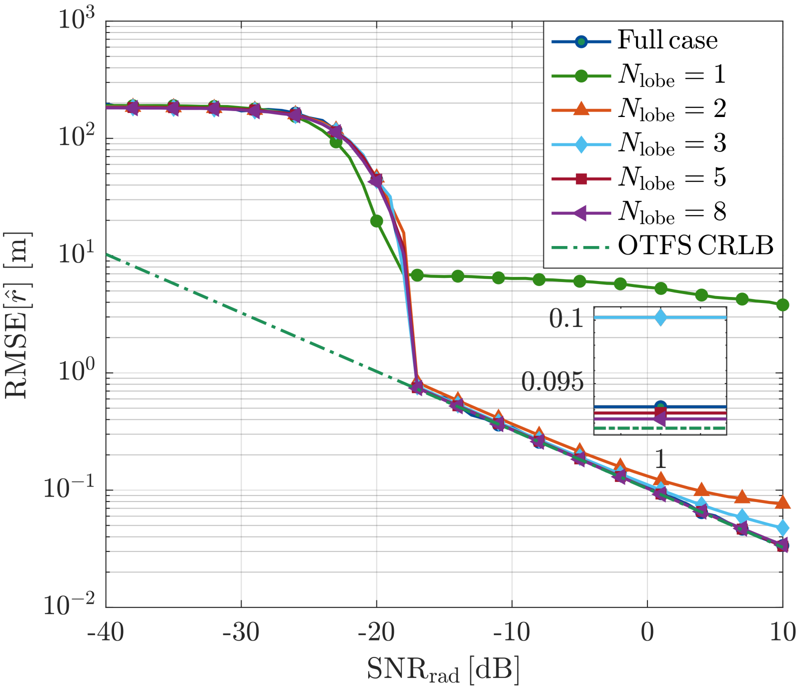

(a) Range estimation RMSE

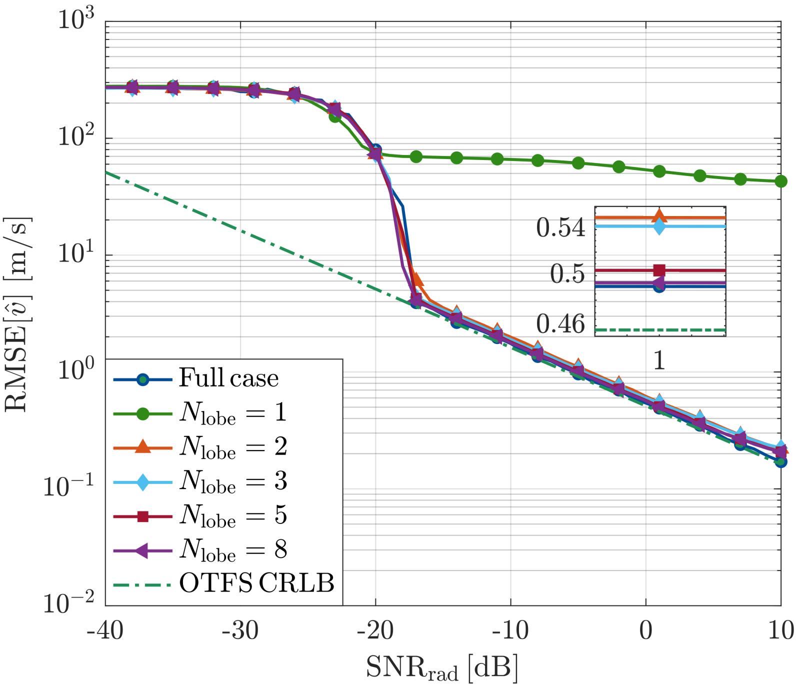

(b) Velocity estimation RMSE

Figure 7.7: RMSE related to range estimation $\hat{r}$ (a) and velocity estimation $\hat{v}$ (b) for $N_\text{lobe} = 1, 2, 3, 5, 8$ and for the full case, as a function of the SNR.

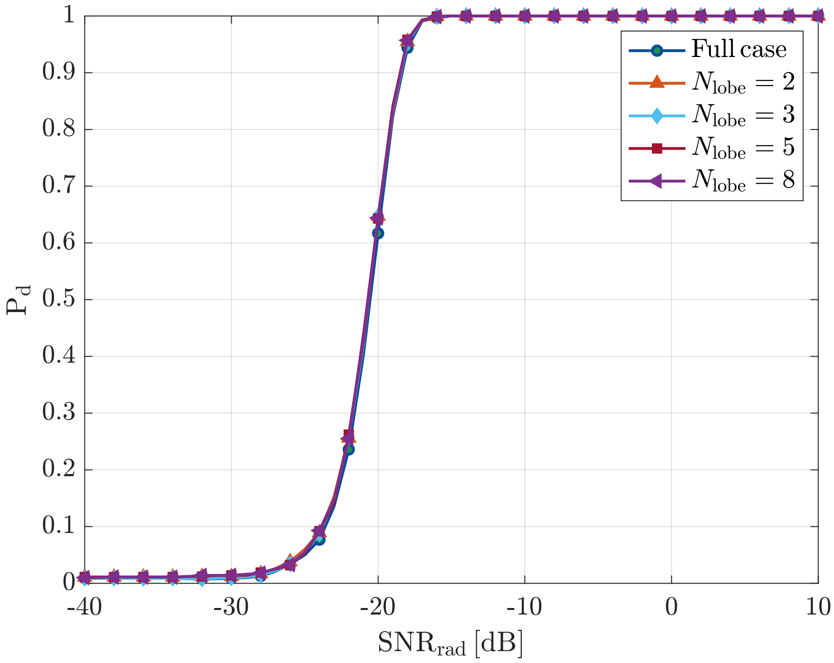

Figure 7.8: Probability of detection as a function of the SNR, computed for $N_{\mathrm{lobe}} = 2, 3, 5, 8$ and for the full case. The curves are obtained by fixing FAR $= 10^{-2}$ on the search space Γ^0

.

Conclusion

Joint sensing and communication (JSC) is a groundbreaking system-level approach to future mobile networks based on the idea of integrating radar and communication functionality into a single architecture by the sharing of physical layer and hardware resources. Given the pervasiveness of mobile systems, this can open the door to ubiquitous and pervasive sensing while improving the energy and spectral efficiency of future wireless networks.

The scope of this dissertation was to explore a variety of signal processing techniques used to estimate the position (via range and DoA estimation) and velocity of passive objects in JSC systems and to perform a comprehensive analysis of their accuracy. The analysis focused on two main areas, providing insights and innovative solutions for OFDM and OTFS based JSC systems.

In the first part of the thesis, OFDM-based JSC systems were investigated, with a focus on the key factors influencing sensing performance in different radar configurations. Monostatic, bistatic, and multistatic scenarios were considered, with particular emphasis on the potential of MIMO technology. This has been shown to enable the use of the same time-frequency resources for both communication and sensing through spatial multiplexing and the detection of multiple passive objects by scanning the environment.

For both the monostatic and bistatic system analysis, a fully digital multibeam system has been considered where the Tx uses a fraction of the total transmitted power to perform the scan. A strength of the monostatic configuration is that the Tx and Rx can be easily synchronized in space and time because they are co-located in the same BS. This provides a huge advantage, e.g., in terms of process gain associated with beamforming. However, it has been shown that this configuration suffers from the problem of SI and requires full-duplex capabilities. In the presence of good synchronization between Tx and Rx, bistatic JSC systems can be considered a good alternative to monostatic systems. The sensing accuracy and coverage of a bistatic JSC system have been investigated by varying the fraction of power reserved for sensing and the distance between Tx and Rx. Moreover, it has been shown that the use of DoA estimation methods at the Rx to align the Tx and Rx beams to ensure that they effectively illuminate the target is the primary factor responsible for reducing the system localization accuracy.

Finally, a MIMO multistatic setup characterized by a single Tx and two Rxs with HDA architectures has been considered, to exploit spatial diversity to improve target detection capabilities. Recognizing the extended nature of real-world objects such as vehicles, we incorporated ET models into our analysis. In addition, we introduced a general near/far-field channel model. The numerical results obtained have underscored the effectiveness of multistatic configurations for improved detection and highlighted the benefits of considering near-field propagation conditions when deploying large antenna arrays at mmWave frequencies, especially when objects are in close proximity to the Tx or Rx.

The second part of the thesis dealt with JSC systems based on OTFS modulation, a promising technology for future mobile networks. However, the inherent complexity of this modulation requires innovative solutions to mitigate the computational burden. To address this challenge, a novel low-complexity estimation and detection approach based on Dirichlet kernel analysis has been presented, focusing our analysis on a monostatic JSC system. Numerical simulations have shown that the proposed approximation technique not only preserves the detection and estimation performance, but also drastically reduces the computational overhead.

As JSC continues to grow in importance for the next generation of mobile systems, this research aimed to further advance and demonstrate its potential to usher in an era of mobile networks with unprecedented sensing capabilities. It is hoped that future research on JSC systems will gain valuable insights from the analysis and ideas presented in this thesis, particularly at the system model and signal processing levels.

List of Figures

Bibliography

[1] Z. Feng, Z. Fang, Z. Wei, X. Chen, Z. Quan, and D. Ji, "Joint radar and communication: A survey," *China Commun.*, vol. 17, no. 1, pp. 1–27, 2020.

[2] C. De Lima, D. Belot, R. Berkvens, A. Bourdoux, D. Dardari, M. Guillaud, M. Isomursu, E.-S. Lohan, Y. Miao, A. N. Barreto, M. R. K. Aziz, J. Saloranta, T. Sanguanpuak, H. Sarieddeen, G. Seco-Granados, J. Suutala, T. Svensson, M. Valkama, B. Van Liempd, and H. Wymeersch, "Convergent communication, sensing and localization in 6G systems: An overview of technologies, opportunities and challenges," *IEEE Access*, vol. 9, pp. 26902–26925, 2021.

[3] J. A. Zhang, M. L. Rahman, K. Wu, X. Huang, Y. J. Guo, S. Chen, and J. Yuan, "Enabling joint communication and radar sensing in mobile networks—a survey," *IEEE Commun. Surveys Tuts.*, vol. 24, no. 1, pp. 306–345, 2022.

[4] Z. Wei, H. Qu, Y. Wang, X. Yuan, H. Wu, Y. Du, K. Han, N. Zhang, and Z. Feng, "Integrated sensing and communication signals toward 5g-a and 6g: A survey," *IEEE Internet Things J.*, vol. 10, no. 13, pp. 11068–11092, 2023.

[5] M. L. Rahman, J. A. Zhang, X. Huang, Y. Guo, and R. Jr, "Framework for a perceptive mobile network using joint communication and radar sensing," *IEEE Trans. Aerosp. Electron. Syst.*, Sep. 2019.

[6] J. A. Zhang, F. Liu, C. Masouros, R. W. Heath, Z. Feng, L. Zheng, and A. Petropulu, "An overview of signal processing techniques for joint

communication and radar sensing," *IEEE J. Sel. Topics Signal Process.*, vol. 15, pp. 1295–1315, Nov. 2021.

[7] F. Liu, Y. Cui, C. Masouros, J. Xu, T. X. Han, Y. C. Eldar, and S. Buzzi, "Integrated sensing and communications: Toward dual-functional wireless networks for 6G and beyond," *IEEE J. Sel. Areas Commun.*, vol. 40, no. 6, pp. 1728–1767, 2022.

[8] S. Dwivedi, M. Zoli, A. N. Barreto, P. Sen, and G. Fettweis, "Secure joint communications and sensing using chirp modulation," in *Proc. 2020 2nd 6G Wireless Summit (6G SUMMIT)*, (Levi, Finland), pp. 1–5, Mar. 2020.

[9] M. Braun, *OFDM radar algorithms in mobile communication networks.* PhD thesis, Karlsruhe Institute of Technology, 2014.

[10] R. Hadani, S. Rakib, S. Kons, M. Tsatsanis, A. Monk, C. Ibars, J. Delfeld, Y. Hebron, A. J. Goldsmith, A. F. Molisch, and A. R. Calderbank, "Orthogonal time frequency space modulation," *CoRR*, vol. abs/1808.00519, 2018.

[11] L. Gaudio, M. Kobayashi, G. Caire, and G. Colavolpe, "On the effectiveness of OTFS for joint radar parameter estimation and communication," *IEEE Trans. Commun.*, vol. 19, no. 9, pp. 5951–5965, 2020.

[12] C. B. Barneto, T. Riihonen, M. Turunen, L. Anttila, M. Fleischer, K. Stadius, J. Ryynänen, and M. Valkama, "Full-duplex OFDM radar with LTE and 5G NR waveforms: challenges, solutions, and measurements," *IEEE Trans. Microw. Theory Techn.*, vol. 67, pp. 4042–4054, Oct. 2019.

[13] N. J. Willis, *Bistatic radar.* SciTech Publishing, 2 ed., 2005.

[14] M. Braun, C. Sturm, and F. K. Jondral, "Maximum likelihood speed and distance estimation for OFDM radar," in *Proc. IEEE Radar Conf.*, (Arlington, VA, USA), pp. 256–261, May 2010.

[15] C. Sturm and W. Wiesbeck, “Waveform design and signal processing aspects for fusion of wireless communications and radar sensing,” *Proc. IEEE*, vol. 99, pp. 1236–1259, July 2011.

[16] 3GPP TS 38.211, *5G; NR; Physical channels and modulation*, 7 2020. version 16.2.0 Release 16.

[17] K. V. Mishra, M. Bhavani Shankar, V. Koivunen, B. Ottersten, and S. A. Vorobyov, “Toward millimeter-wave joint radar communications: A signal processing perspective,” *IEEE Signal Process. Mag.*, vol. 36, no. 5, pp. 100–114, 2019.

[18] J. A. Zhang, X. Huang, Y. J. Guo, J. Yuan, and R. W. Heath, “Multibeam for joint communication and radar sensing using steerable analog antenna arrays,” *IEEE Trans. Veh. Technol.*, vol. 68, pp. 671–685, Jan. 2019.

[19] J. A. Zhang, A. Cantoni, X. Huang, Y. J. Guo, and R. W. Heath, “Joint communications and sensing using two steerable analog antenna arrays,” in *2017 IEEE 85th Vehicular Technology Conference (VTC Spring)*, (Sydney, NSW, Australia), pp. 1–5, June 2017.

[20] Y. Luo, J. A. Zhang, X. Huang, W. Ni, and J. Pan, “Optimization and quantization of multibeam beamforming vector for joint communication and radio sensing,” *IEEE Trans. Commun.*, vol. 67, no. 9, pp. 6468–6482, 2019.

[21] M. Alloulah and H. Huang, “Future millimeter-wave indoor systems: A blueprint for joint communication and sensing,” *Computer*, vol. 52, no. 7, pp. 16–24, 2019.

[22] F. Liu and C. Masouros, “Hybrid beamforming with sub-arrayed mimo radar: Enabling joint sensing and communication at mmwave band,” in *ICASSP 2019 - 2019 IEEE Int. Conf. Acoust. Speech Signal Process. (ICASSP)*, (Brighton, UK), pp. 7770–7774, May 2019.

[23] P. Kumari, S. A. Vorobyov, and R. W. Heath, “Adaptive virtual waveform design for millimeter-wave joint communication–radar,” *IEEE Trans. Signal Process.*, vol. 68, pp. 715–730, 2020.

[24] Y. L. Sit, C. Sturm, J. Baier, and T. Zwick, “Direction of arrival estimation using the MUSIC algorithm for a MIMO OFDM radar,” in *2012 IEEE radar conference*, pp. 0226–0229, IEEE, 2012.

[25] C. B. Barneto, S. D. Liyanaarachchi, T. Riihonen, L. Anttila, and M. Valkama, “Multibeam design for joint communication and sensing in 5G New Radio networks,” in *Proc. IEEE Int. Conf. on Comm. (ICC)*, (online), pp. 1–6, June 2020.

[26] S. Noh, M. D. Zoltowski, and D. J. Love, “Multi-resolution codebook and adaptive beamforming sequence design for millimeter wave beam alignment,” *IEEE Trans. Wireless Commun.*, vol. 16, pp. 5689–5701, Sept. 2017.

[27] R. K. Patra and C. K. Nayak, “A comparison between different adaptive beamforming techniques,” in *Proc. 2019 International Conference on Range Technology*, (Balasore, India), Feb. 2019.

[28] J. A. Zhang, X. Huang, Y. J. Guo, J. Yuan, and R. W. Heath, “Multibeam for joint communication and radar sensing using steerable analog antenna arrays,” *IEEE Trans. Veh. Technol.*, vol. 68, pp. 671–685, Jan. 2019.

[29] S. D. Liyanaarachchi, C. Baquero B., T. Riihonen, M. Heino, and M. Valkama, “Joint multi-user communication and MIMO radar through full-duplex hybrid beamforming,” in *Proc. IEEE Int. Symp. on Joint Comm. & Sensing (JCS)*, (online), pp. 1–5, Feb. 2021.

[30] O. Kanhere, S. Goyal, M. Beluri, and T. S. Rappaport, “Target localization using bistatic and multistatic radar with 5G NR waveform,” in *Proc. IEEE Veh. Tech. Conf. (VTC2021)*, (online), pp. 1–7, Apr. 2021.

[31] E. Fishler, A. Haimovich, R. Blum, R. Cimini, D. Chizhik, and R. Valenzuela, “Performance of mimo radar systems: Advantages of angular diversity,” in *Conference Record of the Thirty-Eighth Asilomar Conference on Signals, Systems and Computers, 2004.*, vol. 1, (Pacific Grove, CA, USA), pp. 305–309, IEEE, Nov. 2004.

[32] H. Zhang, N. Shlezinger, F. Guidi, D. Dardari, and Y. C. Eldar, “6G wireless communications: From far-field beam steering to near-field beam focusing,” *IEEE Commun. Mag.*, vol. 61, no. 4, pp. 72–77, 2023.

[33] Y. Liu, Z. Wang, J. Xu, C. Ouyang, X. Mu, and R. Schober, “Near-field communications: A tutorial review,” *IEEE Open Journal of the Communications Society*, vol. 4, pp. 1999 – 2049, Aug. 2023.

[34] D. Dardari, N. Decarli, A. Guerra, and F. Guidi, “Los/nlos near-field localization with a large reconfigurable intelligent surface,” *IEEE Transactions on Wireless Communications*, vol. 21, pp. 4282–4294, June 2022.

[35] O. Rinchi, A. Elzanaty, and M.-S. Alouini, “Compressive near-field localization for multipath ris-aided environments,” *IEEE Communications Letters*, vol. 26, pp. 1268–1272, June 2022.

[36] Z. Wang, X. Mu, and Y. Liu, “Near-field integrated sensing and communications,” *IEEE Commun. Lett.*, vol. 27, pp. 2048–2052, Aug. 2023.

[37] Z. Wei, H. Qu, Y. Wang, X. Yuan, H. Wu, Y. Du, K. Han, N. Zhang, and Z. Feng, “Integrated sensing and communication signals towards 5G-A and 6G: A survey,” *IEEE Internet Things J.*, pp. 1–1, 2023.

[38] R. Hadani, S. Rakib, S. Kons, M. Tsatsanis, A. Monk, C. Ibars, J. Delfeld, Y. Hebron, A. J. Goldsmith, A. F. Molisch, and A. R. Calderbank, “Orthogonal time frequency space modulation,” *CoRR*, vol. abs/1808.00519, 2018.

[39] R. Hadani, S. Rakib, M. Tsatsanis, A. Monk, A. J. Goldsmith, A. F. Molisch, and R. Calderbank, “Orthogonal time frequency space modulation,” in *2017 IEEE Wireless Communications and Networking Conference (WCNC)*, pp. 1–6, 2017.

[40] Z. Wei, W. Yuan, S. Li, J. Yuan, G. Bharatula, R. Hadani, and L. Hanzo, "Orthogonal time-frequency space modulation: A promising next-generation waveform," *IEEE Wireless Commun.*, vol. 28, no. 4, pp. 136–144, 2021.

[41] S. K. Mohammed, "Derivation of OTFS modulation from first principles," *IEEE Trans. Veh. Technol.*, vol. 70, no. 8, pp. 7619–7636, 2021.

[42] B. Wang, N. Li, Z. Jiang, J. Zhu, X. She, and P. Chen, "On performance evaluation of OTFS and OFDM modulations for sensing," in *2022 14th International Conference on Wireless Communications and Signal Processing (WCSP)*, pp. 427–431, 2022.

[43] P. Raviteja, Y. Hong, E. Viterbo, and E. Biglieri, "Effective diversity of OTFS modulation," *IEEE Wireless Commun. Lett.*, vol. 9, no. 2, pp. 249–253, 2020.

[44] Y. Wu and Z. Zhang, "Co-existence analysis of OTFS and OFDM waveforms for multi-mobility scenarios," in *2022 IEEE 95th Vehicular Technology Conference: (VTC2022-Spring)*, pp. 1–5, 2022.

[45] H. Zhang, X. Huang, and J. A. Zhang, "Comparison of OTFS diversity performance over slow and fast fading channels," in *2019 IEEE/CIC International Conference on Communications in China (ICCC)*, pp. 828–833, 2019.

[46] S. K. Mohammed, R. Hadani, A. Chockalingam, and R. Calderbank, "OTFS—A mathematical foundation for communication and radar sensing in the delay-doppler domain," *IEEE BITS the Information Theory Magazine*, vol. 2, no. 2, pp. 36–55, 2022.

[47] W. Yuan, Z. Wei, S. Li, R. Schober, and G. Caire, "Orthogonal time frequency space modulation-part iii: ISAC and potential applications," *IEEE Commun. Lett.*, vol. 27, no. 1, pp. 14–18, 2023.

[48] L. Gaudio, M. Kobayashi, B. Bissinger, and G. Caire, "Performance analysis of joint radar and communication using OFDM and OTFS,"

in *2019 IEEE International Conference on Communications Workshops (ICC Workshops)*, (Shanghai, China), pp. 1–6, May 2019.

[49] P. Raviteja, K. T. Phan, Y. Hong, and E. Viterbo, "Orthogonal time frequency space (OTFS) modulation based radar system," in *2019 IEEE Radar Conference (RadarConf)*, pp. 1–6, 2019.

[50] M. F. Keskin, H. Wymeersch, and A. Alvarado, "Radar sensing with OTFS: Embracing ISI and ICI to surpass the ambiguity barrier," in *2021 IEEE International Conference on Communications Workshops (ICC Workshops)*, pp. 1–6, 2021.

[51] T. Thaj and E. Viterbo, "Low complexity iterative rake decision feedback equalizer for zero-padded OTFS systems," *IEEE Trans. Veh. Technol.*, vol. 69, no. 12, pp. 15606–15622, 2020.

[52] T. Thaj, E. Viterbo, and Y. Hong, "Orthogonal time sequency multiplexing modulation: Analysis and low-complexity receiver design," *IEEE Trans. Wireless Commun.*, vol. 20, no. 12, pp. 7842–7855, 2021.

[53] T. Thaj, E. Viterbo, and Y. Hong, "General I/O relations and low-complexity universal MRC detection for all OTFS variants," *IEEE Access*, vol. 10, pp. 96026–96037, 2022.

[54] S. E. Zegrar, S. Rafique, and H. Arslan, "OTFS-FMCW waveform design for low complexity joint sensing and communication," in *2022 IEEE 33rd Annual International Symposium on Personal, Indoor and Mobile Radio Communications (PIMRC)*, pp. 988–993, 2022.

[55] C. Liu, S. Liu, Z. Mao, Y. Huang, and H. Wang, "Low-complexity parameter learning for OTFS modulation based automotive radar," in *ICASSP 2021 - 2021 IEEE International Conference on Acoustics, Speech and Signal Processing (ICASSP)*, pp. 8208–8212, 2021.

[56] F. Lampel, A. Avarado, and F. M. Willems, "On OTFS using the discrete Zak transform," in *2022 IEEE International Conference on Communications Workshops (ICC Workshops)*, pp. 729–734, 2022.

[57] L. Pucci, E. Paolini, and A. Giorgetti, “System-level analysis of joint sensing and communication based on 5G New Radio,” *IEEE J. Sel. Areas Commun.*, vol. 40, pp. 2043–2055, July 2022.

[58] L. Pucci, E. Matricardi, E. Paolini, W. Xu, and A. Giorgetti, “Performance analysis of joint sensing and communication based on 5G New Radio,” in *IEEE Work. on Adv. in Netw. Loc. and Nav. (ANLN), Globecom 2021*, (Madrid, Spain), Dec. 2021.

[59] L. Pucci, E. Matricardi, E. Paolini, W. Xu, and A. Giorgetti, “Performance analysis of a bistatic joint sensing and communication system,” in *Proc. IEEE Int. Conf. Commun. Works.*, (Seoul, Korea), pp. 73–78, July 2022.

[60] T. Bacchielli, L. Pucci, E. Paolini, and A. Giorgetti, “Performance analysis of a low complexity integrated sensing and communication system,” in *Proc. IEEE Veh. Tech. Conf. Fall Workshops*, (Hong-Kong), Oct. 2023.

[61] S. K. Dehkordi, L. Pucci, P. Jung, A. Giorgetti, E. Paolini, and G. Caire, “Multi-static parameter estimation in the near/far field beam space for integrated sensing and communication applications,” 2023.

[62] H. Asplund, D. Astely, P. von Butovitsch, T. Chapman, M. Frenne, F. Ghasemzadeh, M. Hagström, B. Hogan, G. Jöngren, J. Karlsson, *et al.*, *Advanced Antenna Systems for 5G Network Deployments: Bridging the Gap Between Theory and Practice.* Academic Press, 2020.

[63] Y. Luo, J. A. Zhang, X. Huang, W. Ni, and J. Pan, “Multibeam optimization for joint communication and radio sensing using analog antenna arrays,” *IEEE Trans. Veh. Technol.*, vol. 69, no. 10, pp. 11000–11013, 2020.

[64] M. A. Richards, *Fundamentals of radar signal processing.* McGraw-Hill, 2005.

[65] 3GPP TR 38.830, *Study on NR coverage enhancements*, 12 2020. version 1.0.0 Release 17.

[66] S. Moloudi, M. Mozaffari, S. N. K. Veedu, K. Kittichokechai, Y.-P. E. Wang, J. Bergman, and A. Höglund, "Coverage evaluation for 5g reduced capability new radio (NR-redcap)," *IEEE Access*, vol. 9, pp. 45055–45067, 2021.

[67] Y. Zeng, Y. Ma, and S. Sun, "Joint radar-communication: Low complexity algorithm and self-interference cancellation," in *2018 IEEE Global Communications Conference (GLOBECOM)*, pp. 1–7, 2018.

[68] S. J. Orfanidis, *Electromagnetic Waves and Antennas.* New Jersey, USA: Sophocles J. Orfanidis, 1 ed., 2016.

[69] M. Wax and T. Kailath, "Detection of signals by information theoretic criteria," *IEEE Trans. Acoust., Speech, Signal Process.*, vol. 33, pp. 387–392, Apr. 1985.

[70] A. Mariani, A. Giorgetti, and M. Chiani, "Model order selection based on information theoretic criteria: Design of the penalty," *IEEE Trans. Signal Process.*, vol. 63, pp. 2779–2789, June 2015.

[71] R. O. Schmidt, "Multiple emitter location and signal parameter estimation," *IEEE Trans. Antennas Propag.*, vol. 34, pp. 276–280, Mar. 1986.

[72] D. Schuhmacher, B.-T. Vo, and B.-N. Vo, "A consistent metric for performance evaluation of multi-object filters," *IEEE Trans. Signal Process.*, vol. 56, pp. 3447–3457, Aug. 2008.

[73] Z. Li, A. Giorgetti, and K. Sithamparanathan, "Multiple radio transmitter localization via uav-based mapping," *IEEE Trans. Veh. Technol.*, pp. 1–12, 2021.

[74] M. Chiani, A. Giorgetti, and E. Paolini, "Sensor radar for object tracking," *Proc. IEEE*, vol. 106, pp. 1022–1041, Jun 2018.

[75] R. Roy and T. Kailath, "ESPRIT-estimation of signal parameters via rotational invariance techniques," *IEEE Trans. Acoust., Speech, Signal Process.*, vol. 37, pp. 984–995, July 1989.

[76] P. Stoica and R. L. Moses, *Spectral analysis of signals.* Pearson Prentice Hall Upper Saddle River, NJ, 2005.

[77] F. Sohrabi and W. Yu, "Hybrid analog and digital beamforming for mmwave ofdm large-scale antenna arrays," *IEEE Journal on Selected Areas in Communications*, vol. 35, pp. 1432–1443, July 2017.

[78] H. Griffiths, "From a different perspective: principles, practice and potential of bistatic radar," in *2003 Proceedings of the International Conference on Radar (IEEE Cat. No.03EX695)*, (Adelaide, SA, Australia), pp. 1–7, Sep. 2003.

[79] S. K. Dehkordi, L. Gaudio, M. Kobayashi, G. Caire, and G. Colavolpe, "Beam-space MIMO radar for joint communication and sensing with OTFS modulation," *IEEE Trans. Wireless Commun.*, vol. 22, pp. 6737–6749, Oct. 2023.

[80] W. Boyse and A. Seidl, "A hybrid finite element method for 3-D scattering using nodal and edge elements," *IEEE Transactions on Antennas and Propagation*, vol. 42, pp. 1436–1442, Oct. 1994.

[81] P. Kumari, J. Choi, N. González-Prelcic, and R. W. Heath, "IEEE 802.11ad-based radar: An approach to joint vehicular communication-radar system," *IEEE Trans. Veh. Technol.*, vol. 67, pp. 3012–3027, April 2018.

[82] D. H. N. Nguyen and R. W. Heath, "Delay and Doppler processing for multi-target detection with IEEE 802.11 OFDM signaling," in *2017 IEEE International Conference on Acoustics, Speech and Signal Processing (ICASSP)*, (New Orleans, LA, USA), pp. 3414–3418, Mar. 2017.

[83] D. C. Rife and R. R. Boorstyn, "Multiple tone parameter estimation from discrete-time observations," *Bell Syst. Tech. J.*, vol. 55, pp. 1389–1410, Nov. 1976.

[84] M. Kronauge and H. Rohling, "Fast two-dimensional CFAR procedure," *IEEE Trans. Aerosp. Electron. Syst.*, vol. 49, no. 3, pp. 1817–1823, 2013.

[85] E. Björnson and L. Sanguinetti, "Power scaling laws and near-field behaviors of massive MIMO and intelligent reflecting surfaces," *IEEE Open Journal of the Communications Society*, vol. 1, pp. 1306–1324, Sep. 2020.

[86] F. Wang, X. Wang, X. Li, X. Hou, L. Chen, S. Suyama, and T. Asai, "Ring-type codebook design for reconfigurable intelligent surface near-field beamforming," in *Proc. 2022 IEEE 33rd Annual International Symposium on Personal, Indoor and Mobile Radio Communications (PIMRC)*, (Kyoto, Japan), pp. 391–396, Sep. 2022.

[87] M. Goemans and D. Williamson, "Improved approximation algorithms for maximum cut and satisfiability problems using semidefinite programming," *Journal of Association for Computing Machinery*, vol. 42, p. 1115–1145, Nov. 1995.

[88] P. W. Kassakian, *Convex Approximation and Optimization with Applications in Magnitude Filter Design and Radiation Pattern Synthesis.* PhD dissertation, University of California, Berkeley, 2006.

[89] V. S. Chernyak, *Fundamentals of multisite radar systems: multistatic radars and multistatic radar systems.* CRC press, 1998.

[90] D. Rife and R. Boorstyn, "Single tone parameter estimation from discrete-time observations," *IEEE Trans. Inf. Theory*, vol. 20, no. 5, pp. 591–598, 1974.

[91] A. Fam, "Efficient complex matrix multiplication," *IEEE Trans. Comput.*, vol. 37, pp. 877–879, July 1988.

[92] D. H. N. Nguyen and R. W. Heath, "Delay and doppler processing for multi-target detection with IEEE 802.11 OFDM signaling," in *2017 IEEE International Conference on Acoustics, Speech and Signal Processing (ICASSP)*, pp. 3414–3418, 2017.

Acknowledgements

There are several people I would like to thank at the end of this long journey within my PhD.

First of all, I would like to thank my family. My parents, Antonella and Arsenio, for always being by my side and supporting me in every important decision of my life. My younger brother Leonardo and my sister Laura.

I would like to thank all my close friends for their understanding and support during the difficult times I have experienced in the last three years. In particular, I would like to thank my dear friends Andrea and Elia, with whom I have shared every moment of joy and discouragement. They have always been there to listen to me and give me valuable advice.

I would like to thank my advisor Prof. Enrico Paolini and my co-advisor Prof. Andrea Giorgetti for always supporting me during these years. Their invaluable suggestions and teachings have been fundamental to reach the end of this journey.

I want to express my sincere appreciation to Prof. Giuseppe Caire for his invaluable guidance and support during my time as a visiting student at the Technical University of Berlin. His extensive expertise has been an indispensable resource, and I feel fortunate to have had the opportunity to learn from him.

I am also very grateful to my co-authors Tommaso, Elisabetta, and Saeid for their invaluable collaboration, which allows me to significantly enhance the quality and impact of the research presented in this thesis.

Lastly, a very special thank you is reserved for the most special person to me, who has made a unique contribution to my success. Her unwavering support and belief in me gave me the strength to complete this dissertation and regain my confidence in myself. This dissertation is dedicated to her.